2005

Experimental investigation of stick-slip behavior in granular materials

Lynne E. Roussel
Louisiana State University and Agricultural and Mechanical College

EXPERIMENTAL INVESTIGATION OF STICK-SLIP BEHAVIOR IN GRANULAR MATERIALS

A Thesis

Submitted to the Graduate Faculty of the
Louisiana State University and
Agricultural and Mechanical College
in partial fulfillment of the
requirements for the degree of
Master of Science in Civil Engineering

in

The Department of Civil and Environmental Engineering

By
Lynne E. Roussel
B.S. in Civil Engineering, Louisiana State University, 2003
August, 2005

ACKNOWLEDGEMENTS

I would like to acknowledge my advisor Dr. Khalid A. Alshibli for the encouragement, support, and guidance through this investigation. Also, many thanks to the members of my advisory committee, Dr. John Sansalone and Dr. Clinton Willson for their time and advice.

Special thanks to NASA's Graduate Student Researchers Program Fellowship for providing the financial support that made this investigation possible. I would also like to thank the people at Marshall Space Flight Center in Huntsville, Alabama for allowing us to use their facilities and their time, especially Mr. Buddy Guynes, Dr. Ron Beshears, Mr. David Meyers, and Mr. David Bennett.

I would like to thank all of the students in the lab for their help during my two years of graduate school. To my student worker Megan, thank you for helping me edit my thesis and all of the other little things you have done for me during the testing stages of my research. You were a life saver. Thank you to my lunch buddy Bashar, who was always there to answer my questions on computer tomography and for keeping me from throwing the computer out the window when it was not cooperating. To Bryan and Andrew, thanks for helping me out in the lab when I needed more muscles than Megan and I could provide. Also, thanks to Ardit and Bevin for your help and listening when I needed someone to talk to.

To my parents and family, thank you for believing in me and supporting me through my education. I am very grateful forever thing that you have done for me. I would also like thank my fiancé Adam, his love, support, and patience have kept me going these past two years.

And last, but not least, I would like to thank God. Without him none of this would be possible.

TABLE OF CONTENTS

LIST OF TABLES

LIST OF FIGURES

ABSTRACT

The mechanical behavior of granular materials is highly dependent on the arrangement of particles, particle groups, and associated pore spaces. Changes in the internal structure due to large deformation may cause changes in the mechanical behavior. The changes include: particle sliding, rolling, and interaction; shear band formation; and fabric anisotropy. During those changes, stick-slip behavior may take place between the granular particles. The objective of the thesis is to study the factors that influence the stick-slip behavior of granular materials. The influence of particle size, uniformity, confining pressure, density, and strain rate are investigated in this thesis. A series of axisymmetric triaxial tests were performed on glass beads to study the shear strength of granular materials. Sizes that were used are labeled as Very Small (d = 0.15 – 0.25 mm), Small (d = 0.75 – 1.00 mm), Medium (d = 1.55 – 1.85 mm), Large (d = 3.30 – 3.60 mm), and Well-graded (d = 0.09 – 1.55 mm). The confining pressures were 25, 100, 250, and 400 kPa. The load oscillations that appeared in the stress-strain results were analyzed to find the causes of the stick-slip behavior. To study the internal structure of the particles, two axisymmetric triaxial tests were performed on the glass beads under low confining pressure (25 kPa). The specimens were composed of Very Small, Medium, and Well-graded. The specimens were scanned before and after compression using a X-ray computed tomography system.

In general, a slight post peak principle stress softening was observed as well as a continuous volume increase (dilation) even at relatively high strains. This appears to be caused by the uniform shape of the spherical particles. The load oscillations that appeared in the very small, small, and well-graded beads are due to the stick-slip phenomenon. From the computed tomography analysis, the specimens showed a bulging deformation mode. This is because the

particles roll each other continuously during compression; they do not interlock. In the medium beads after compression, columns of beads were found in the specimen to support the theory of the stick-slip behavior.

CHAPTER 1

INTRODUCTION

1.1 Problem Statement

Granular materials are an assembly of particles that behave differently than any other standard form of matter. The mechanical behavior of the material depends on the particle arrangement, particle group, and the pore spaces. When the internal structure fabric of the granular material is changed, this behavior produces different responses, which include: particle sliding, rolling, and interaction; shear band formation; and fabric anisotropy. Understanding this behavior is very important for geological processes involving landslides, erosion, and plate tectonics; and in the design of foundation systems, dams, and retaining walls.

The stick-slip phenomenon occurs in the granular material when the particles begin to slide and roll over each other. Sometimes one may observe sudden releases of stress during the deformation of granular material. In 1966, Brace and Byerlee proposed that stick-slip instabilities in laboratory friction experiments might be similar to earthquakes. In 1967, Burridge and Knopoff established one of the first models linking stick-slip with faulting. Since then a large amount of experimental work has been done to determine the nature of these instabilities. In the laboratory, it is easy to use local shear deformation tests on granular materials since it is easier to control (Adjemian et al 2004).

The changing of the internal structure can be analyzed using Computed Tomography (CT). CT uses x-ray technology and computer processing to reconstruct an image of a cross sectional plane of an object. The object is rotated while an x-ray beam passes through it. A detector on the other side of the object collects the x-ray beams that are absorbed and reflected. The information is compiled by the computer system and it reconstructs a 2-dimensional cross

section of the object. Alshibli et al (2000) used computed tomography to study the internal fabric change and the localization deformation in sand triaxial specimen.

1.2 Scope of Work

The experimental work discussed in this thesis was performed using uniform spherical glass beads with known particle size, surface texture, and shape. The objectives of this thesis are:

- Investigate the factors that influence load oscillations in glass beads
- Analyze the internal structure and shear localization phenomena using computed tomography under conventional triaxial compression tests.

A series of axisymmetric triaxial tests were performed on glass beads to study the shear strength of granular materials (glass beads). The test parameters include the particle size, uniformity (gradation) of particles, and confining pressure. For uniform specimens, the sizes that were used were labeled as Very Small (d = 0.15-0.25 mm), Small (d = 0.75-1.00 mm), Medium (d = 1.55-1.85 mm), and Large (d = 3.30-3.60 mm). The tests of the non-uniform specimens were carried out on a well-graded mixture of glass beads ranging from 0.09-1.55 mm in particle diameter. The confining pressures were 25, 100, 250, and 400 kPa. The surface textures of the particles for all of the experiments were “smooth”. The load oscillations that appeared in the stress-strain results were analyzed to find the causes of this stick-slip behavior.

To study the internal structure of the particles, two axisymmetric triaxial tests were performed on the glass beads under low confining pressure (25 kPa). The specimens were composed of Very Small, Medium, and Well-graded beads. The specimens were scanned utilizing the computed tomography system. The two scans were compared to see if there is a difference in the internal structure of the specimens before and after compression.

1.3 Thesis Outline

This thesis begins with a literature review (Chapter 2) to present an overview of the strength properties and stick-slip behavior of granular materials. A description of the glass beads, their chemical composition, their particle size distribution, and images of the surface and shape of the beads using Scanning Electron Microscopy are presented in the first part of Chapter 3. The description of the sensors, apparatus for testing, and specimen preparation are found at the end of Chapter 3. A summary of the experimental program is also presented in Chapter 3.

Chapter 4 discusses the results of the experimental work. The stress-strain responses of the specimens are described. The stick-slip behavior and the influence of particle size and confining pressure are also discussed. Chapter 5 briefly presents the Computed Tomography literature review, the description, testing procedure and the results of the analysis in the form of contour maps of the void ratios before and after compression.

CHAPTER 2

LITERATURE REVIEW

2.1 Friction

The shear resistance between two particles is the force that must be applied to cause a relative movement between the particles. The total shear resistance is proportional to the normal force pushing the two particles together. The frictional resistance is usually represented by the coefficient of friction or a friction angle. There are two basic laws of frictional behavior (Lambe and Whitman 1969):

- The shear resistance between two bodies is proportional to the normal force between them.
- The shear resistance between two bodies is independent of the dimensions of the two bodies.

Leonardo da Vinci created these laws, in the late 1400's, but they were forgotten. However, in 1699, Amontons, a French engineer, rediscovered the laws of frictional resistance, and today they are known as Amontons's laws.

In soil mechanics, different sources contribute to frictional resistance, including: sliding and rolling of particles, resistance to volume change, particle interlocking, and particle crushing. The behavior of soils is more complicated than a wooden block sliding across a wooden surface. One reason is that soils have a tendency to change in volume as they are sheared (Figure 2.1); therefore, it is very important to measure the change in volume during shearing (Powrie 1997).

2.2 Axisymmetric Triaxial Testing

The axisymmetric triaxial test is the most common test used to determine the stress-strain properties of a soil. In this test, a rubber latex membrane encases a cylindrical specimen in a cell

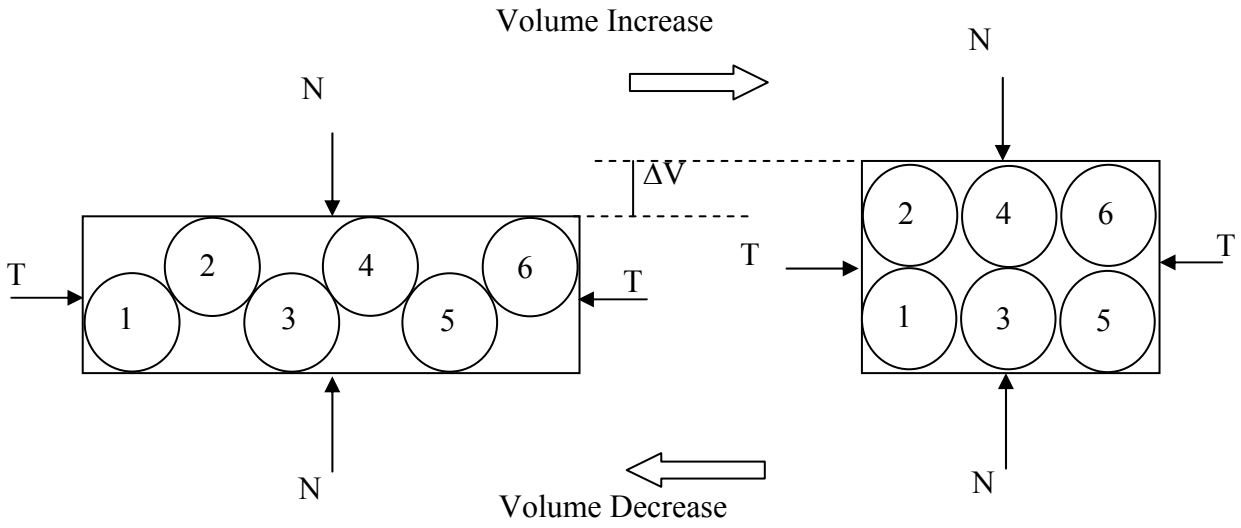

Figure 2.1 Volume change (dilatancy) due to shearing

filled with water. Pressurizing the water in the cell confines the specimen, and then it is subjected to loading at a constant strain rate in the axial direction until it reaches failure. Figure 2.2 shows a schematic of a triaxial testing system. A triaxial test is typically conducted under drained or undrained conditions depending on the field drainage conditions. During a drained test, the volume change of the specimen is measured by the amount of water that comes in or out of the cell. For the undrained test, the change in the pore water pressure inside the specimen is measured.

The conventional triaxial compression (CTC) test is the most common form of a triaxial test. In this test, a constant confining (cell) pressure (σ_c) is maintained while the specimen is loaded in the axial direction. It is assumed that no shear stresses occur at the end plates, σ_c and

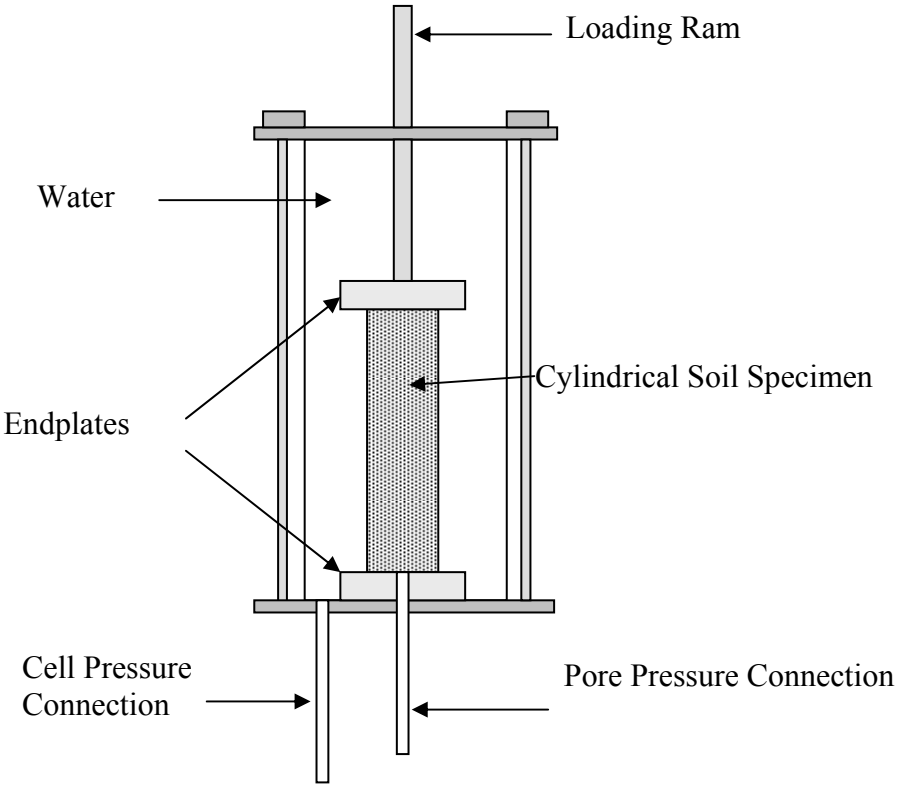

Figure 2.2 Schematic of a triaxial test cell

the axial stress: $\sigma_a \approx \sigma_c + (F_a/A)$ can be taken as the minor (σ_3) and major (σ_1) principal stresses, respectively. The following equations are used to analyze the results of a CTC test:

Deviator stress $q=\sigma_1-\sigma_3$ (2.1)

Nominal axial strain $\varepsilon_a=\Delta h/h_0$ (2.2)

Volumetric strain $\varepsilon_v=\Delta V/V_0$ (2.3)

Where: Δh = change in height

h_0 = initial height

ΔV = change in volume

V_0 = initial volume

Dense sand specimens exhibit a different response when compared to loose specimen. Figure 2.3 presents typical behavior of a dense and a loose soil specimen test under CTC. In a dense specimen, the behavior can be divided into three different stages: initial, peak, and post peak regimes. During the initial stage, a small decrease in volume is observed because the particles are being pushed together making it denser. The specimen fails at the peak stress stage, and the deviator stress at this stage is called the peak shear strength of the material. Also, at this stage, the shear forces move the particles, causing an increase in the volume of the specimen. As the shearing continues, the interlocking between the particles decreases, and a drop in the strength just after the peak occurs. The shear force required to produce that movement also decreases. In the post peak regime, shear deformation occurs without any change in volume where the soil reaches a critical state condition. For a loose specimen, the behavior is different, where a peak deviator stress is not commonly observed. The deviator stress remains constant once it reaches the maximum shear strength. At the initial stage, the specimen exhibits a decrease in volume. This volume change remains constant once the maximum shear strength is reached due to the lower density of the specimen. Therefore the interlocking between the particles is relatively small, less shear resistance occurs, and no change in volume is observed.

The stress-strain behavior of granular materials is also dependent on the particle arrangement, density state, shape, and surface roughness. These properties determine the level of interlocking and sliding resistance between the particles, and the higher the interlocking, the higher the friction resistance between the particles.

2.3 Stick-Slip Behavior

The slip-stick behavior is observed in some granular materials during shearing. During sticking, the particles at the interface are closely packed and have high shear strength (Cain 2001). The material dilates periodically and behaves like a fluid, allowing the slider to slip.

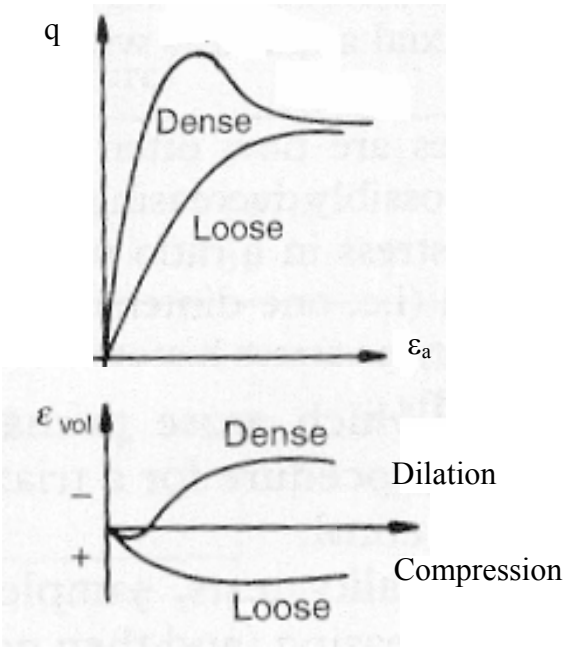

Figure 2.3 Typical behavior of a dense and a loose granular material subject to CTC (Powrie 1997)

Significant dilation occurs prior to the slip event. A well known property of granular materials is that the applied loads are not distributed uniformly. They are instead supported by chains of approximately linearly aligned particles. Breaking these stress chains results in redistributions of the granular packing. Under shear stress, as stress chains break and reform, small fluctuations in the global stress occur as the sample creeps, a likely mechanism for the precursor to slip in a granular material (Radjai 1995). The motion is periodic and may be due to some periodic arrangement of the grains.

Stick-slip phenomenon can be captured using apparatuses that can impose localized shear deformation conditions. Many studies have been carried out using shear tests. Radjai et al. (1995) used an array of cylinders that were pushed along a surface. The cylinders were placed on a track and pushed with a driving rod until they reached a fixed wall. Through their research and

experimentation, they found that the particles stuck to the plane while the driving force increased to the boundary until it was high enough to trigger a slipping motion of all the particles. Ragjai et al. (1995) have also studied the forces before and after each slip during the experiment as well as the rotations of the cylinders. They found that the global dynamic and static coefficients of friction of the system increased with the number of particles. Nasuno et al. (1998) investigated the behavior of granular layers that were subjected to shear forces and to the resulting frictional forces that are generated in the material. The apparatus used for experimentation included a granular layer with a transparent cover plate that is pushed by a spring and a sensor that detects the deflection of the spring. The effects of varying the stiffness of the driving system and the driving velocity were studied, and they found that stick-slip motion occurs for low driving velocity. Cain et al. (2001) used an annular shear cell to investigate the factors that influence stick-slip motion in an assembly of monosized glass spheres. They found that the drive velocity and the applied normal pressure influence the magnitude of the stick-slip spikes.

Stick-slip behavior was also studied in granular drag by Albert et al. (2001). They studied the fluctuations of the drag force experienced by an object moving through a granular medium (Figure 2.4). An applied external stress results in the development of an internal structure resisting the stress called jammed state. The origins of the jamming lie in the fact that the forces do not propagate uniformly through the granular sample but are localized along directional force chains. They also investigated the jamming of spherical granular media by carrying out tests to analyze the drag force opposing the movement of a solid object through the media. During a test, the object's motion is opposed by jamming the grains in front of the object. As the object moves, the surrounding grains are displaced. These breakdowns result in large fluctuations in the drag

force at low velocities. The motion of the cylinder attempting to advance relative to the grains is opposed by force chains that start at the cylinder's surface and propagate on average in the direction of the cylinder's motion. These force chains will terminate rather differently depending on the depth at which they originate (Figure 2.5).

Figure 2.6a shows the results from a small depth (H=60 mm) signal shape for different grain sizes. The small grains show a well defined periodicity, while the large grain sizes manifest a random pattern. Figure 2.6b shows the results from a large depth signal shape for different grain diameters. The changes due to the increase in grain size cause the pattern to change from nearly periodic to the stepped stick-slip motion with increasing grain size. From this study, they found stick-slip fluctuations are strongly influenced by the long range nature of the force propagation in granular materials, and the jamming originates from a localized applied stress.

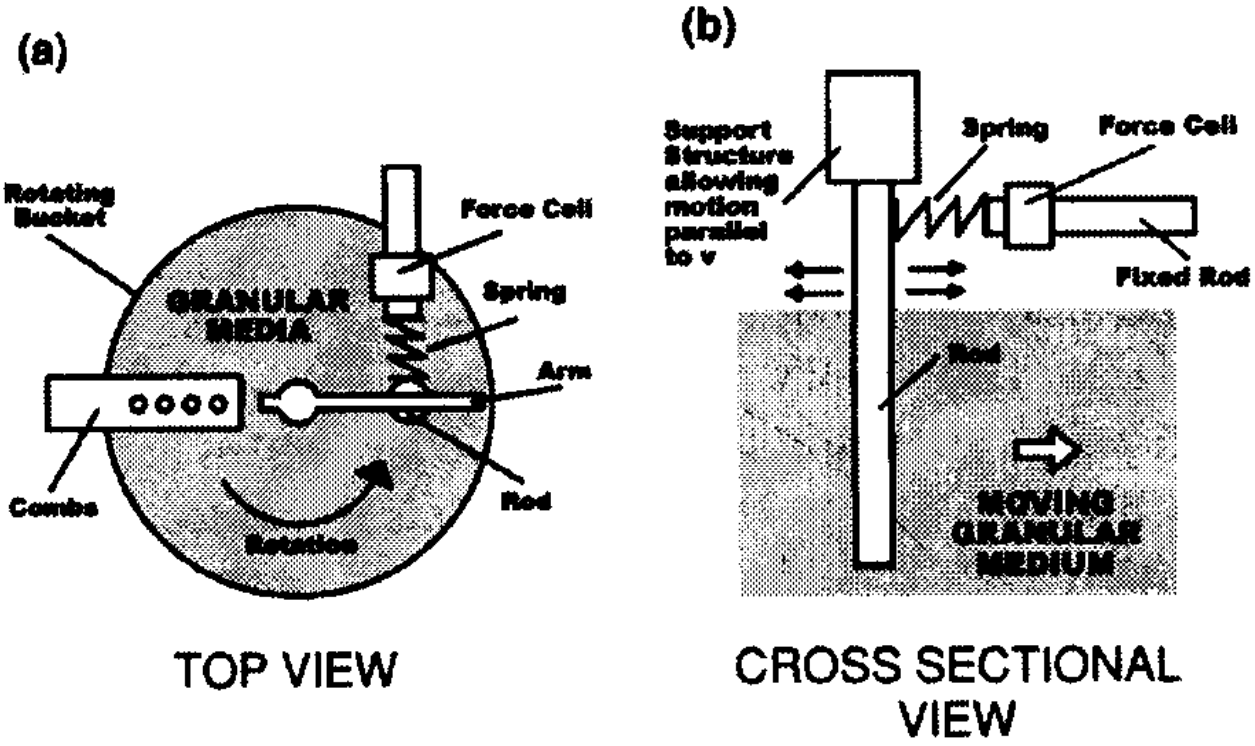

Figure 2.4 Schematic view of the testing apparatus (Albert et al 2001)

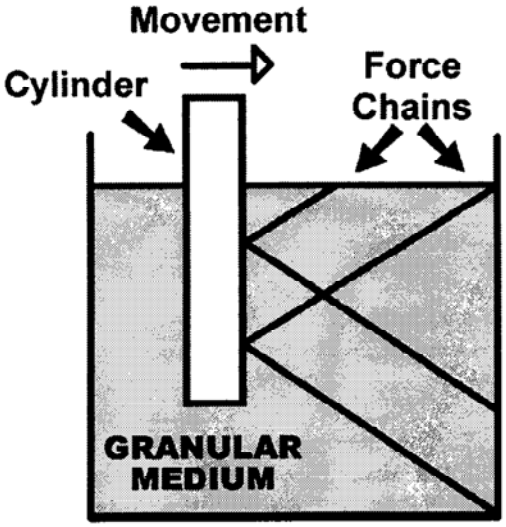

Figure 2.5 Schematic diagram of the force chains (Albert et al 2001)

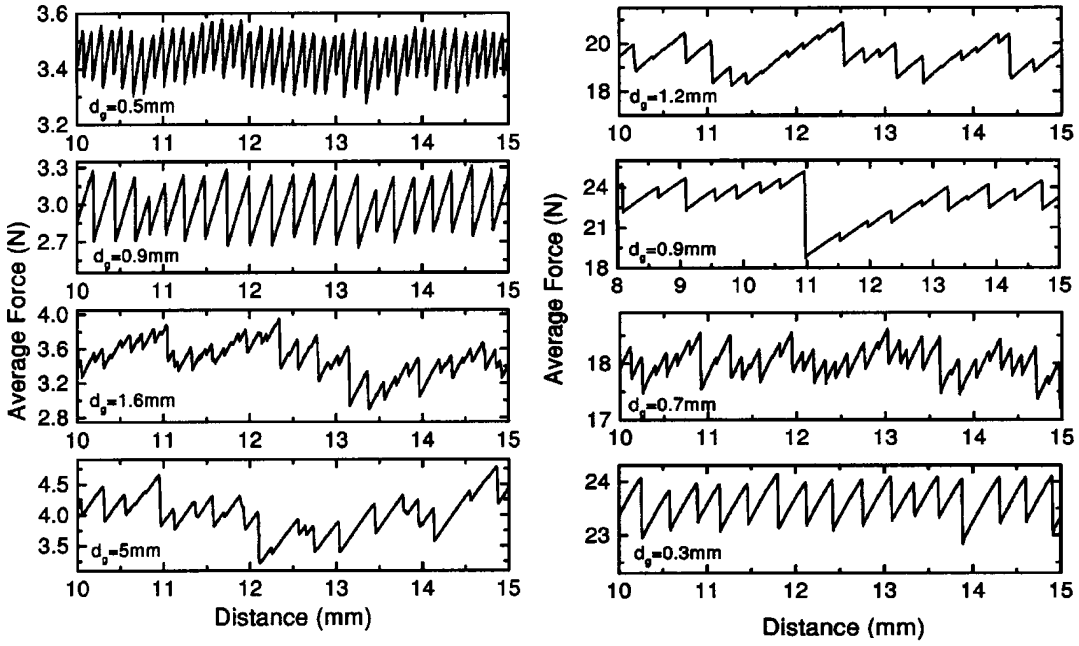

(a) (b)

Figure 2.6 (a) Small depth signal shape for different diameters of glass particles, (b) large depth signal shape for different diameters (Albert et al. 2001).

2.3.1 Stick-Slip Behavior in Soil Mechanics

In soil mechanics, the axisymmetric triaxial compression test is more commonly used than direct shear tests because it allows better control of applied stresses and boundary conditions. There are few studies that investigate stick-slip during axisymmertic triaxial compression tests on soils. In 2004, Adjemian and Evesque studied the stick-slip behavior in glass beads and Hostun sand. Figure 2.7 shows a typical deviator stress versus axial strain relationship for a loose Hostun sand specimen. The compression rate was changed twice during the test, and the stress response remained smooth. Also, the deviator stress did not decrease when the velocity was increased, concluding that the mechanics of the deformation are stable. Figure 2.7 (e) shows the volumetric strain versus axial strain for the Hostun sand sample. This is a classical result for a loose sand sample. Figure 2.7 (b) illustrates a typical response obtained from large mono-disperse glass spheres with no apparent stick-slip, but it is "noisy" due to the smallness of the sample (D= 50 mm, H= 84 mm) compared to the grain size (d= 3 mm). These results were always found for this case for the large mono-disperse glass spheres. Figure 2.7 (c) shows a typical behavior of from small polydisperse glass beads where three different loading speeds were used (0.083, 0.18, and 0.5 mm/min). Strong variations are noticed when the velocity changed. An increase of the loading speed implies a decrease in strength. This is called velocity weakening behavior which leads to unstable mechanical behaviors. Also, large stress drops are observed at large strains. The change in deviator stress (Δq) seems to diminish when the velocity increases. Figure 2.7 (c) is expanded horizontally to define typical features of the stick-slip. The variation of the volumetric strain versus axial strain for a large bead sample that produces the stick-slip which is shown in Figure 2.7 (f) does not present rapid volume changes when stick-slip occurs; therefore, the stick-slip is not related to the macroscopic dynamical dilation effect. It may

be possible to relate the sudden Δq changes to the sensitivity of q_{max} to the velocity, because stick-slip is caused by a decrease in stiffness when the strain rate is increased.

Figure 2.8 illustrates the results from the small polydisperse glass beads with a confining pressure of 70 kPa. The size of the beads and the chronology of strain rate vary for experiments. It was found that the strain rate plays an important role in the stick-slip amplitudes. When the loading speed increases, the Δq amplitude decreases. Also, when the strain rate is too fast, the stick-slip does not have enough time to develop completely. From these tests the strain rate seems to influence the stick-slip phenomenon.

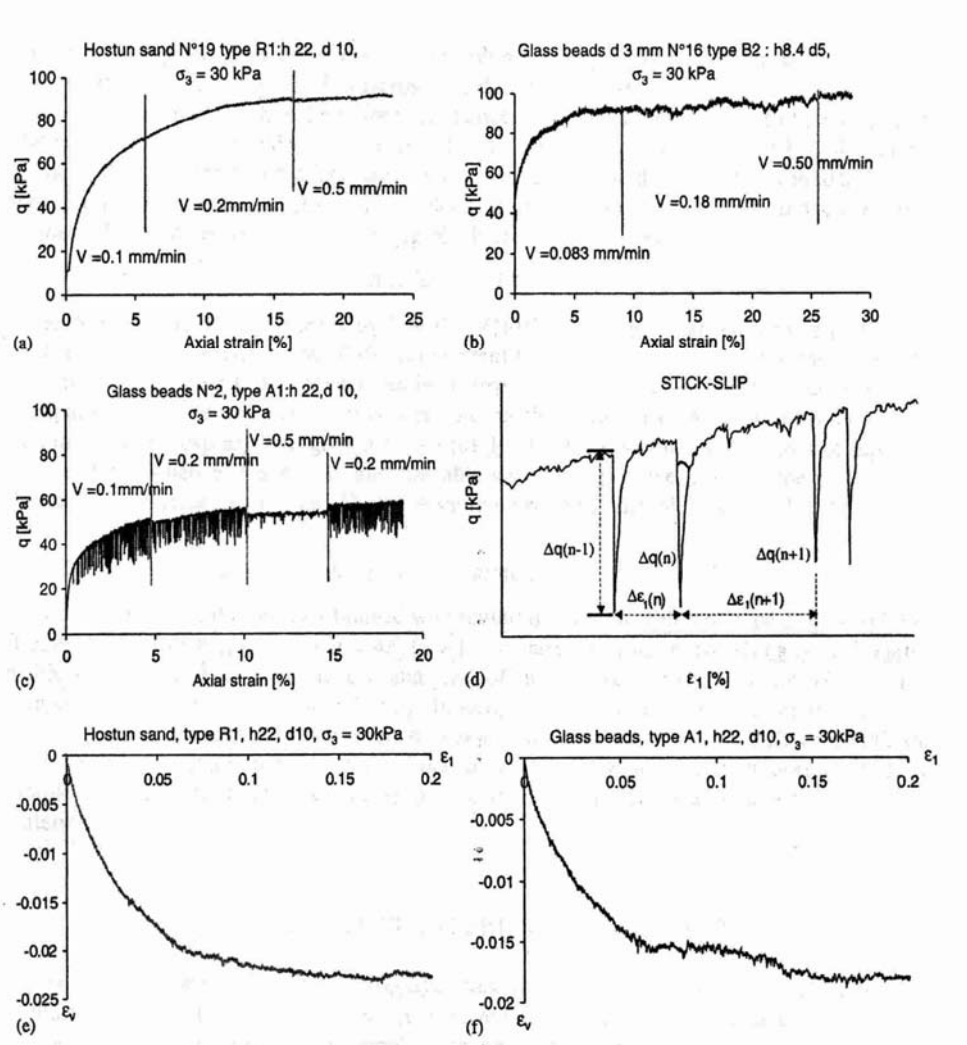

Figure 2.7 Test Results from Adjemian and Evesque (2004)

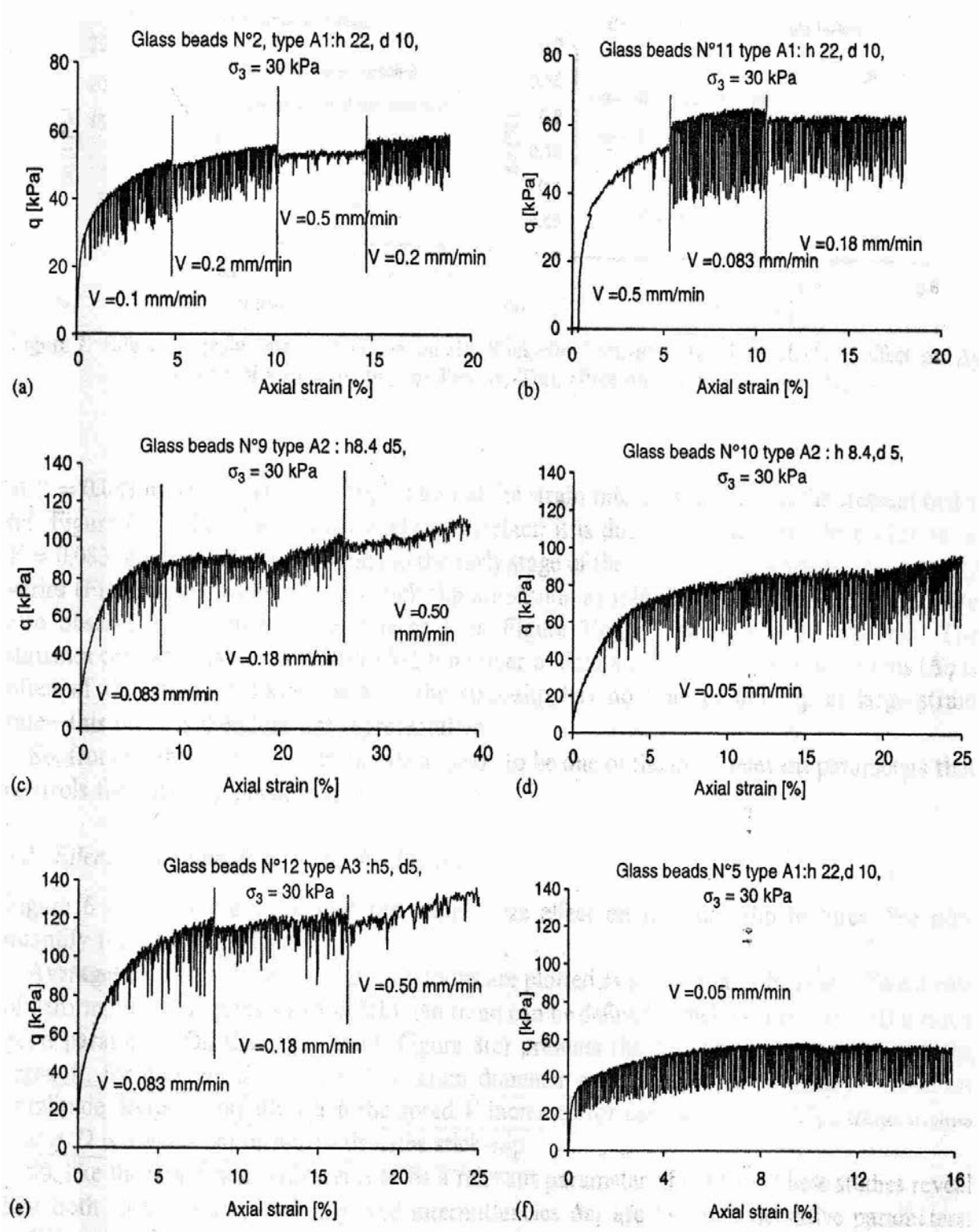

Figure 2.8 More Test Results from Adjemian and Evesque (2004)

The effect of specimen size on stick-slip is shown in Figure 2.9 where the average Δq amplitudes and the Δε variations are plotted as a function of height (H) to diameter (D) or H/D at different velocities. The stress amplitude decreases rapidly when the velocity increases for each d/D (particle diameter to specimen diameter) ratio. The effect of confining stress is shown in Figure 2.10 where Δq increases as $\sigma`_3$ increases. Figure 2.11 shows the effect of specimen density. Where the dense specimen composed of the glass beads behavior is similar to that of the dense sand specimens. It was found that the velocity weakening does not generate stick-slip behavior in dense specimens of glass beads.

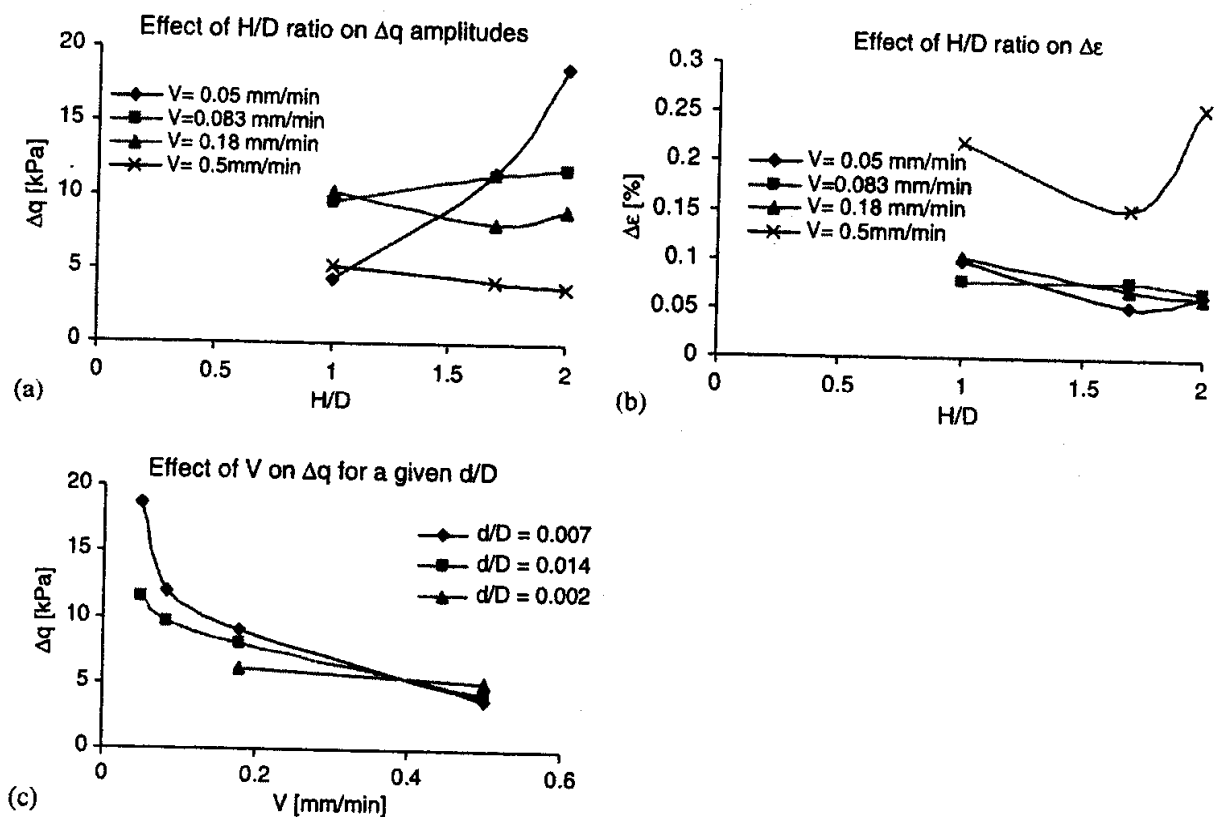

Figure 2.9 Effect of specimen size D/d and of the specimen ratio H/D on stick-slip behavior (Adjemian and Evesque 2004)

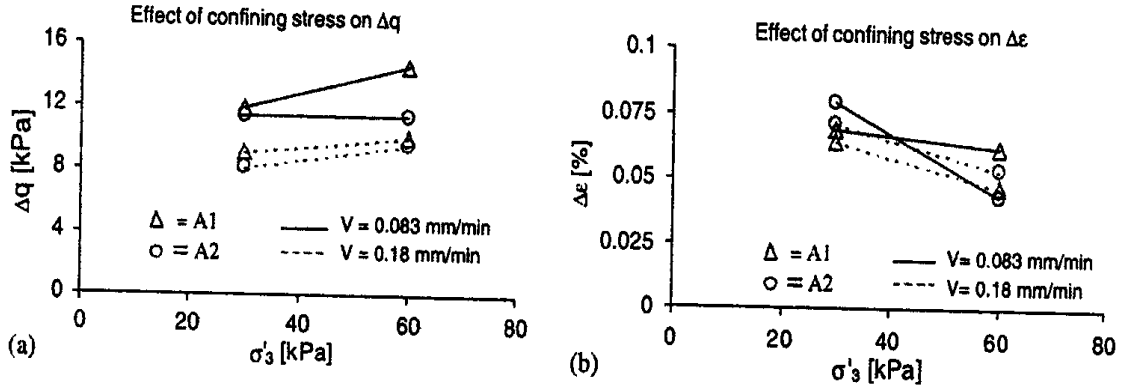

Figure 2.10 Influence of effective confining pressure on the stick-slip behavior (Adjemian and Evesque 2004)

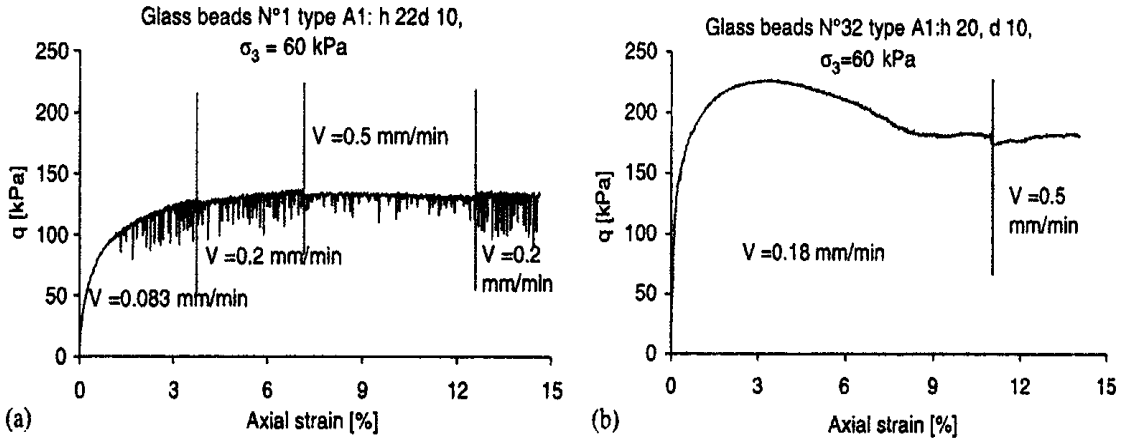

Figure 2.11 The influence of density on stick-behavoir (Adjemian and Evesque 2004)

Adjemian and Evesque (2004) concluded that stick-slip seems to disappear at large strain rates and that stick-slip is sensitive to rapid variation of deviator stress forcing it to disappear. They also concluded that slick-slip disappears in relatively large specimens with fast loading rates.

2.4 Stress Chains

During shearing, the load is distributed throughout the particles in the form of stress chains, an inhomogeneous stress profile caused by the absence of strong spatial disorder of grains. These forces are carried primarily by a small fraction of the total number of grains. Under slow deformations, the changes in stress chains lead to strong fluctuations. In physics, there has been some research on stress chains and stress fluctuations. Behringer et al (1999) conducted experiments on a slowly sheared 2D granular material to study the stress chains in the material. The experiments were carried out on a 2D granular system consisting of photoelastic polymer disks that were subjected to a steady slow shearing in a flat Couette geometry. The disks were viewed through an arrangement of circular polarizers so that the stress on the disks can be characterized using photoelasticity. Figure 2.12 depicts a schematic of the apparatus which consists of an inner shearing wheel (A) with a radius of 10.34 cm. and an outer shearing ring (B) with an inner radius of 19.14 cm. The two wheels are confined by planetary gears (C). During the experiment, the apparatus was placed in a polarmeter using a circular polarization scheme. The disks had a thickness of 6 mm and were confined between the wheel and ring as well as two smooth slippery horizontal plexiglas sheets. Each disk had a small dark bar that was used for tracking the position and the orientation of individual disks using a video.

The packing fraction was varied over the range 0.77 to 0.81 and the ratio of small to large disks was kept constant. The rotational rate of the inner wheel was also varied for the experiments. Near a contact, the stresses within a disk are not very uniform, which lead to bands in the polariscope image. The number of bands increased monotonically with the force at the contact. Part of Behringer et al.'s (1999) research was to identify a continuous transition in the dynamic behavior as the fraction of area occupied by disks (γ) approaches the packing fraction for a square lattice (γ_c). As γ approaches γ_c the fluctuations become more intermittent, and the

mean velocity vanishes at γ_c. At this point the system is highly compressible and easily sheared. The stress chain length, orientation, and distribution change significantly. Close to γ_c, the stress network consists of long uninterrupted chains which tend to be oriented primarily radially and propagate much of the distance between the inner and outer wheel. However, as γ increases, the network becomes more tangled with many shorter intersecting chains (Figure 2.13). As the disks are compressed, those bearing the largest forces will deform so that other disks can carry some of the load. To estimate the force chains, a force calibration (G^2) was calibrated by placing a known force on the boundary of a small number of disks (50-300) while measuring G^2. They defined the length of a chain to be any set of nearly collinear disks carrying stress larger than the mean. It was found that near γ_c the chains are unstable to buckling, unless they are perfectly aligned and supported at the ends by solid boundaries. For higher γ, the chains were better supported against buckling, and more contacts carried the applied loads. For a highly dense system, almost all of the contacts are actively carrying force, and the system appeared homogenous.

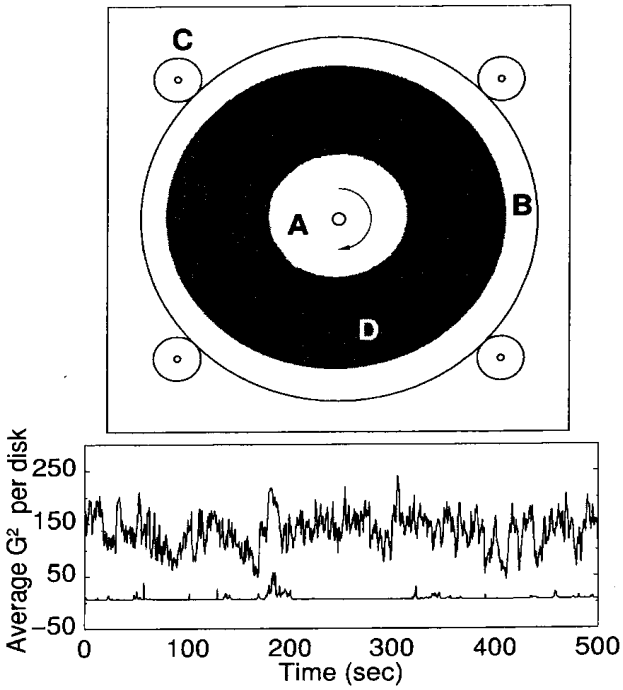

Figure 2.12 Diagram of Behringer's testing apparatus (Behringer et al. 1999)

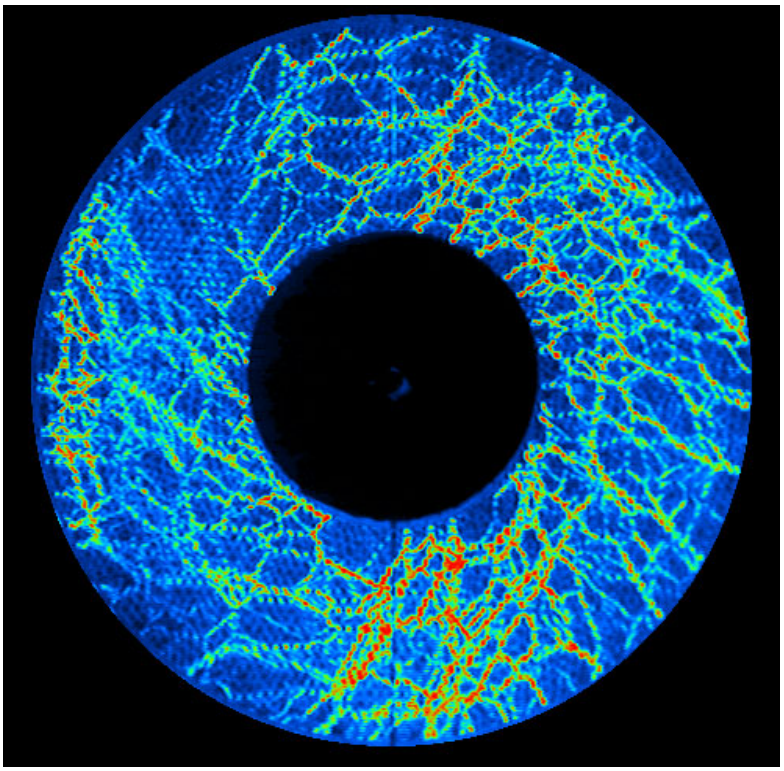

Figure 2.13 Image of stress chains from photoelastic disks (Behringer et al. 1999)

CHAPTER 3

EXPERIMENTAL WORK

3.1 Introduction

This chapter describes the materials used in the investigation and the experimental work presented in this thesis. The chemical analysis and the physical properties of the material are also reported. A description of the equipment, sensors, data acquisition system, the procedure for specimen preparation and testing, and a summary of the conventional triaxial compression test are presented.

3.2 Material Characterization

3.2.1 Material Description

The glass beads used for the experiments were obtained from Jaygo Incorporated, Union, New Jersey. They are composed of the following: silicon dioxide, sodium dioxide, calcium oxide, magnesium oxide, aluminum oxide, and potassium and ferrum oxides. The five different sets of beads were used for the experiments are listed in Table 3.1 with their corresponding diameters.

Table 3.1 Diameter of glass beads used in the experiments

Bead Label	Diameter (mm)
Very small	0.15 - 0.25
Small	0.75 - 1.00
Medium	1.55 - 1.85
Large	3.30 - 3.60
Well-graded mixture	0.09 - 1.55

The glass beads have a shiny smooth surface texture. To look at the surface and the shape of the beads, the Scanning Electron Microscope (SEM) was used at a high magnification level. Figures 3.1 to 3.3 show the Small, Medium, and Large Beads, respectively.

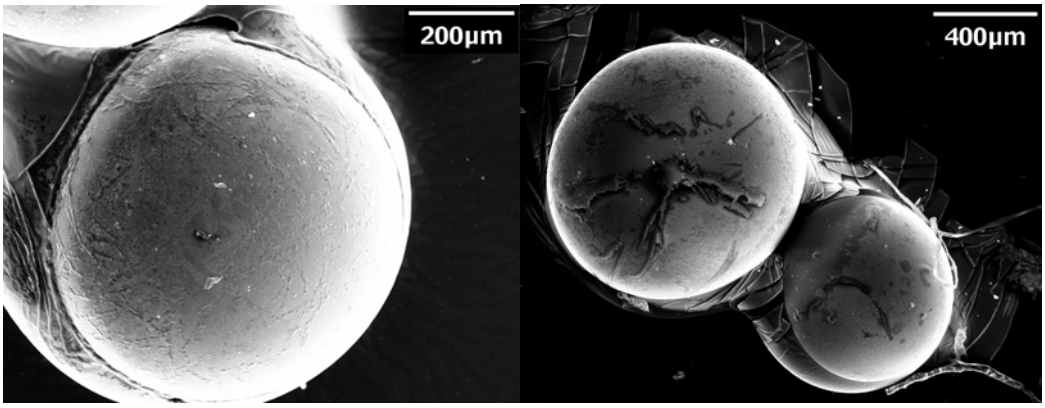

Figure 3.1 SEM images of the small glass beads

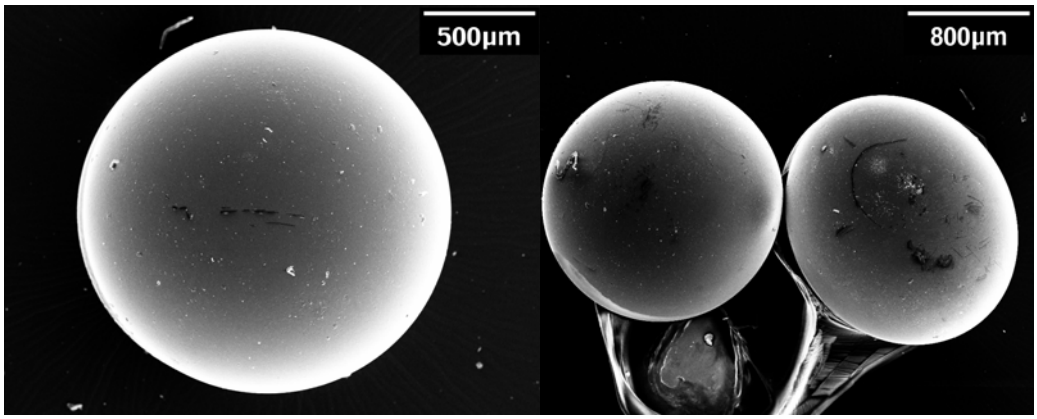

Figure 3.2 SEM images of the medium glass beads

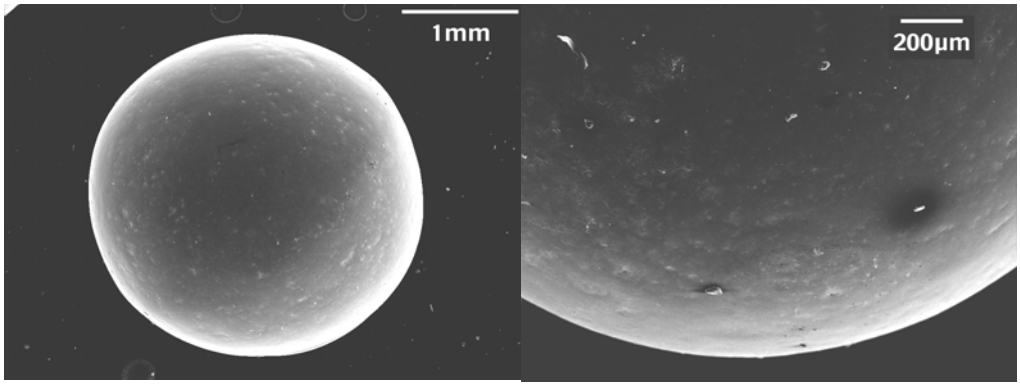

Fig 3.3 SEM images of the large glass beads

3.2.2 Chemical Analysis of the Glass Beads

The material data sheet from the Dragonite Solid Glass Beads listed the chemical characteristics of the soda lime glass and states that there are possibly slight deviations in the amount of chemicals. This could be the cause of the different color of the beads. The chemical analysis was also used for the calculation of the mass attenuation for the computer tomography results. To find the percentage of elements present in the glass beads, the AXIS 165 High Performance Multi-Technique Surface Analysis in the Mechanical Engineering Department's Materials Characterization Center was used. Because the equipment is complex and one must be trained to use it, Dr. Jiechao Jiang, the manager of the lab, conducted the analysis. The AXIS 165 High Performance Multi-Technique Surface Analysis has many flexible configurations and capabilities that allow it to perform surface and material analysis using Auger Electron Spectroscopy (AES), Ion Scattering Spectroscopy (ISS), and X-ray Photoelectron Spectroscopy (XPS).

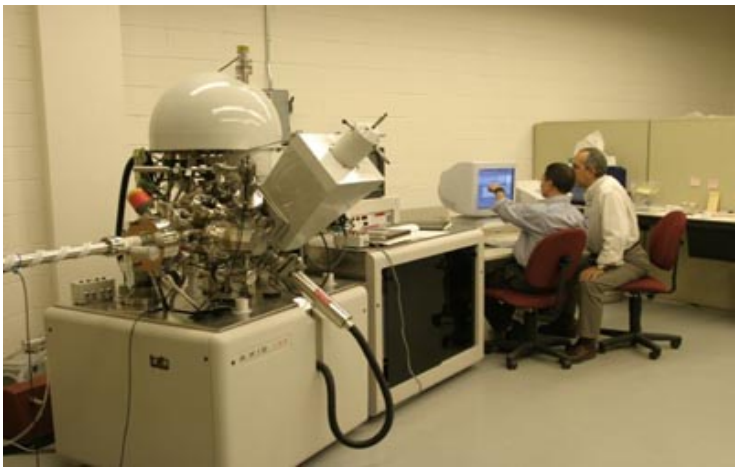

Figure 3.4 AXIS 165 High Performance Multi-Technique Surface Analysis in the Mechanical Engineering Department's Materials Characterization Center

It is based on a 165 mm mean radius hemispherical analyzer with an eight-channeltron detection system for excellent energy resolution and sensitivity at small analysis areas. The magnetic immersion lens enables the high performance XPS imaging to be obtained in a realistic time frame. The AXIS accommodates a 15kV, 1000Å Scanning Auger current capability, which is an electrostatic gun using a lanthanum hexaboride filament for a high current. A computer controls the gun allowing a reproducible setup. The system is connected to a workstation, which has a graphical interface for ease of use.

To prepare the sample, the glass beads were placed on the standard Kratos specimen stub (1 cm diameter). Then the sample was placed in the machine and was placed under a vacuum overnight. The tests were run on the beads and the computer workstation showed the energy intensity traces for the beads. From these plots the elements were located and the energy intensity determined the percentage of the element present. Table 3.2 compares the percentage results to those of the material data sheet of the glass beads. The amount of oxygen present in each bead was also compared (Table 3.3). The results from the chemical analysis on the glass beads showed a difference in the percentages of oxides in all three size beads. For the small beads, there were only three oxides present in the beads: silicon dioxide, sodium dioxide, and calcium oxide. The first two dioxides amounts are only off by around one percent; however, there was a 4.52 % difference between our analysis and the manufactured data sheet for the calcium dioxide. The medium beads had a slight difference for all of the oxides found in the beads. The largest difference in the amounts of oxides from the data sheets and the chemical analysis was found in the large beads. The silicon dioxide found in the large beads was 19.34% which is much smaller than the 72% reported on the data sheet from Jaygo Inc. Also, the calcium oxide, magnesium oxide, and potassium oxides all have at least a 15% difference in actual

amount found in the large beads. This difference in percentages from the Jaygo Inc. data sheet is probably because the material is produced for quantity and not quality. The large beads are blue, the small are blue green, and the medium are gray. This is shown in Figure 3.5.

Table 3.2 Chemical analysis of glass beads

Jaygo Inc. Data Sheet		This Study Analysis		
		Small Beads [%]	**Medium Beads** [%]	**Large Beads** [%]
SiO_2	72.0%	73.60	61.12	19.34
Na_2O	13.0%	12.87	19.88	7.47
CaO	9.0%	13.52	6.15	24.33
MgO	4.0%	0.00	4.28	25.43
Al_2O_3	1.0%	0.00	0.00	0.57
K_2O	0.5%	0.00	8.58	22.86
Fe_2O_3	0.5%	0.00	0.00	0.00

Table 3.3 Oxygen Content in Beads from the Tests

Bead Size	**Oxygen Content** [%]
Small	62.55%
Medium	67.54%
Large	61.60%

Figure 3.5 Color of Small, Medium, and Large Glass Beads

3.2.3 Particle Size Analysis

Particle size analysis (ASTM D 422-63) was performed to check the uniformity of the beads. Approximately 100 grams of glass beads were used for the very small, small, medium, and well-graded beads. For the large glass beads, approximately 200 grams were used. It was based on the particle size as recommended by Bardet (1997). The particle size distributions are presented in Figure 3.6. . The uniformity coefficient (C_u) and curvature coefficient (C_c) were calculated for each set of beads (Table 3.4). The particles ranged from 1.0 to 6.62. The values for the Very Small, Small, Medium, and Large glass beads indicate a high degree of uniformity. However the 6.62 C_u value for the Well-graded glass beads indicates that the mixture is not uniform and it is classified as well-graded according to the Unified Soil Classification System. The specific gravity of solids (G_s) was determined for the five different types of beads. The product data sheet from Jaygo Inc. lists a value of 2.5 for specific gravity. A small variation in specific gravity was obtained in the lab for the different beads and these values were later used in this investigation.

Table 3.4 C_u, C_c, and G_s values for the glass beads

Type of Bead	**C_u**	**C_c**	**G_s**
Very Small	1.17	1.00	2.59
Small	1.22	0.90	2.50
Medium	1.32	0.92	2.59
Large	1.10	1.02	2.55
Well-graded	6.62	1.43	2.53

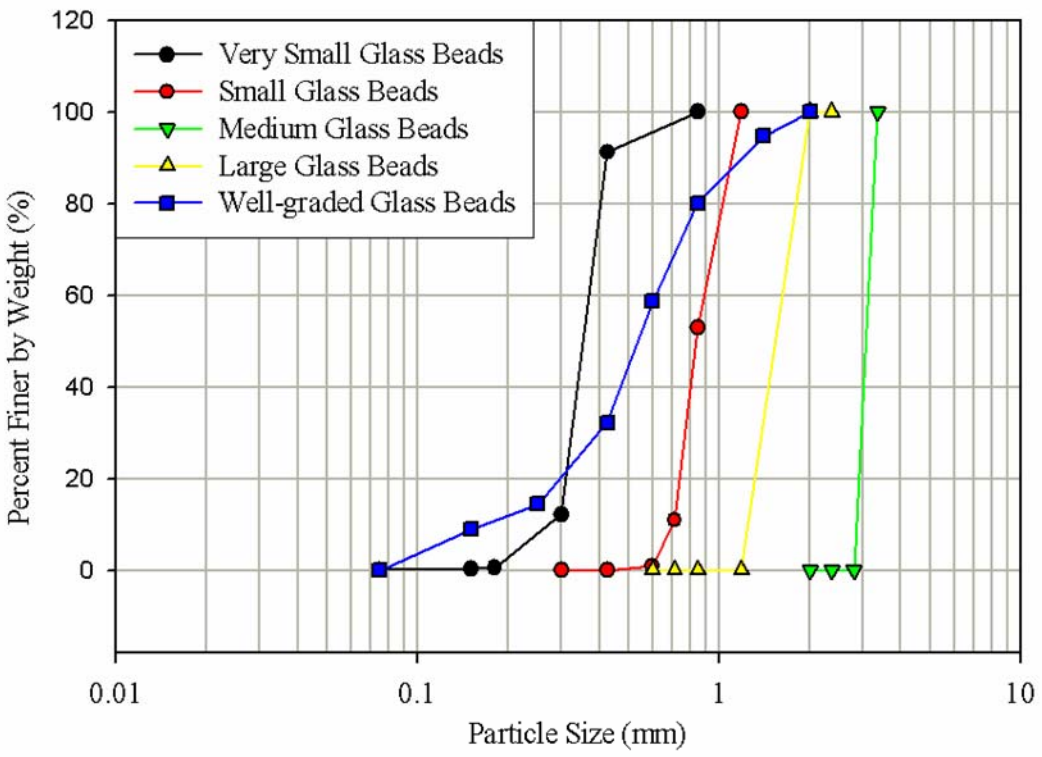

Figure 3.6 Grain size distributions for the different glass beads

3.3 Experimental Work

3.3.1 Sensors

Four instruments were used for the CTC tests: Linear Variable Displacement Transducers (LVDT's), a Load Cell, a Differential Pressure Transducer (DPT), and an Absolute Pressure Transducer (Table 3.5). The instruments used for this study are listed in Table 3.5.

Table 3.5 Instruments used for the study

Instrument	Make	Model	S/N
LVDT	RDP	DCTH500A	57458
LVDT	RDP	1000A	60816
Load Cell	Totco	90 lb	----
Load Cell	Omegadyne	LC101-250	171457
Load Cell	Omegadyne	LC101-1k	150752
DPT	Validyne	P305D	----

Two pressure control systems were used for this study. P1 has a 200 kPa confining pressure limit and P2 has a 550 kPa confining pressure limit. System P1 has a 32 psi Validyne DPT-P305D to measure the pressure. The two DPT's used to measure volume change (Validyne DPT-P305D) have a range of 0.125 psi and 0.5 psi. System P2 has a 100 psi Validyne DPT-3505D to measure pressure and a 2 psi Validyne DPT-3505D to measure the volume change.

Four load cells were used in this study: Totco 90 lb, Omega 250 lb, Omega 500 lb, and Omega 1000 lb. The estimated maximum load was calculated and then the appropriate load cell was selected. To investigate whether the load cells has any influence on the oscillations, two load cells were placed on the load frame to record the readings. It was found that the load cell closer to the range of the applied load was more accurate and had a better resolution than the other one. The load cells gave similar results as a whole but a close look at the results reveals that some points had a better resolution than the larger load cell points (Figure 3.7).

The two LVDT's were used for this study: a RDP-DCTH500A (25.4 mm range (1in)) and RDP-DCTH1000A (50.8 mm range (2 in)). They have different ranges, which cause them to be sensitive to movement. During testing the 1000A LVDT had a lower resolution causing the readings in height change to remain constant for a period of time. The other LVDT had the better resolution and smaller increments of displacement were recorded. To further investigate this, two LVDTs were placed on the triaxial cell to record the displacement. The two reading are shown in Figure 3.8. Also the accuracy was checked for the two LVDT's: 1000A – 0.05196 and 500A-0.02553.

3.3.2 Apparatus Description

The apparatus used for the investigation consists of the following parts: loading frame, pressure control system, triaxial cell, and control panel. The triaxial cell used for the testing was

a conventional axisymmetric cell with enlarged endplates that measure 101.6 mm (4in) in diameter and have polished Tungsten carbide facing. The loading frame (Figure 3.9) operates under a strain-controlled mode. A linear variable differential Transducer (LVDT) was used to measure axial deformation and a load cell was attached to the loading frame. Three different load cells were used. A load cell with the maximum capacity of 90 lbs was used for all the 25 kPa tests, 250 lbs load was used for all the 100 kPa tests, and 1000 lbs was used for all the 250 kPa and 400 kPa tests.

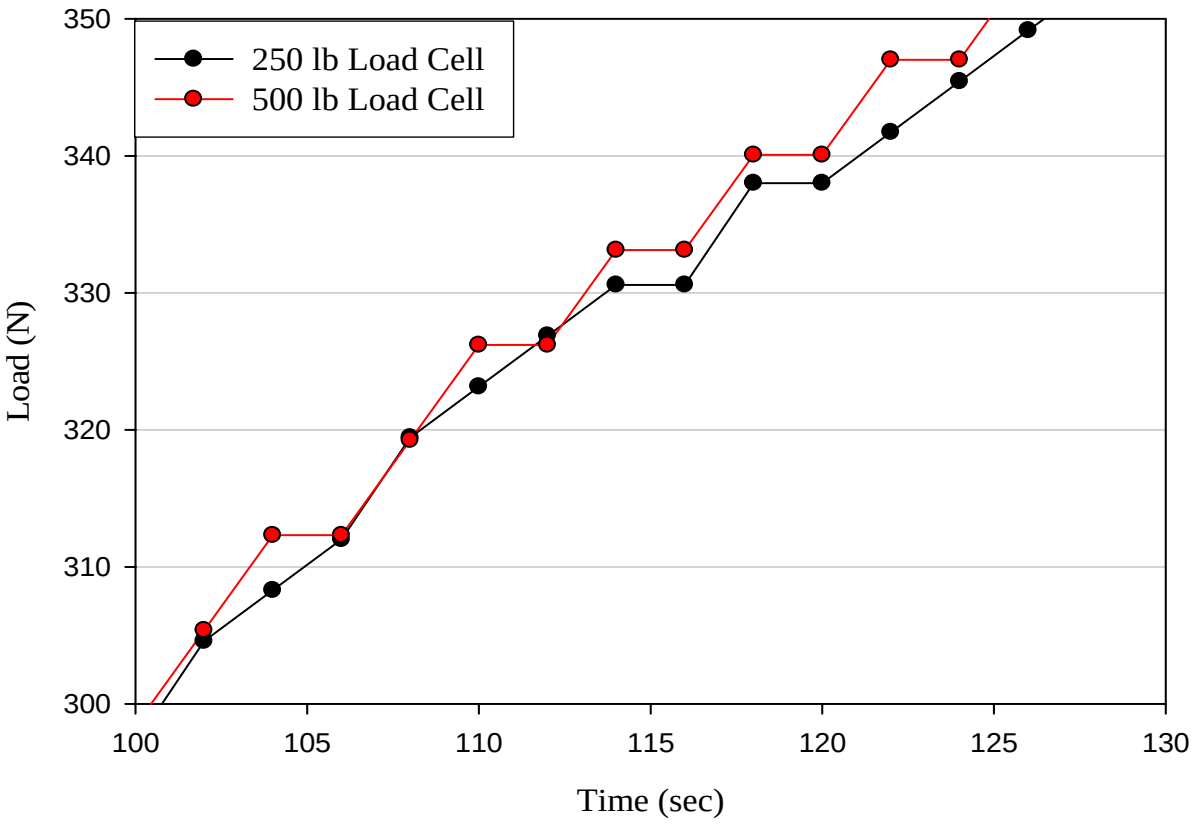

Figure 3.7 Load verses time for 250 lb and 500 lb load cells

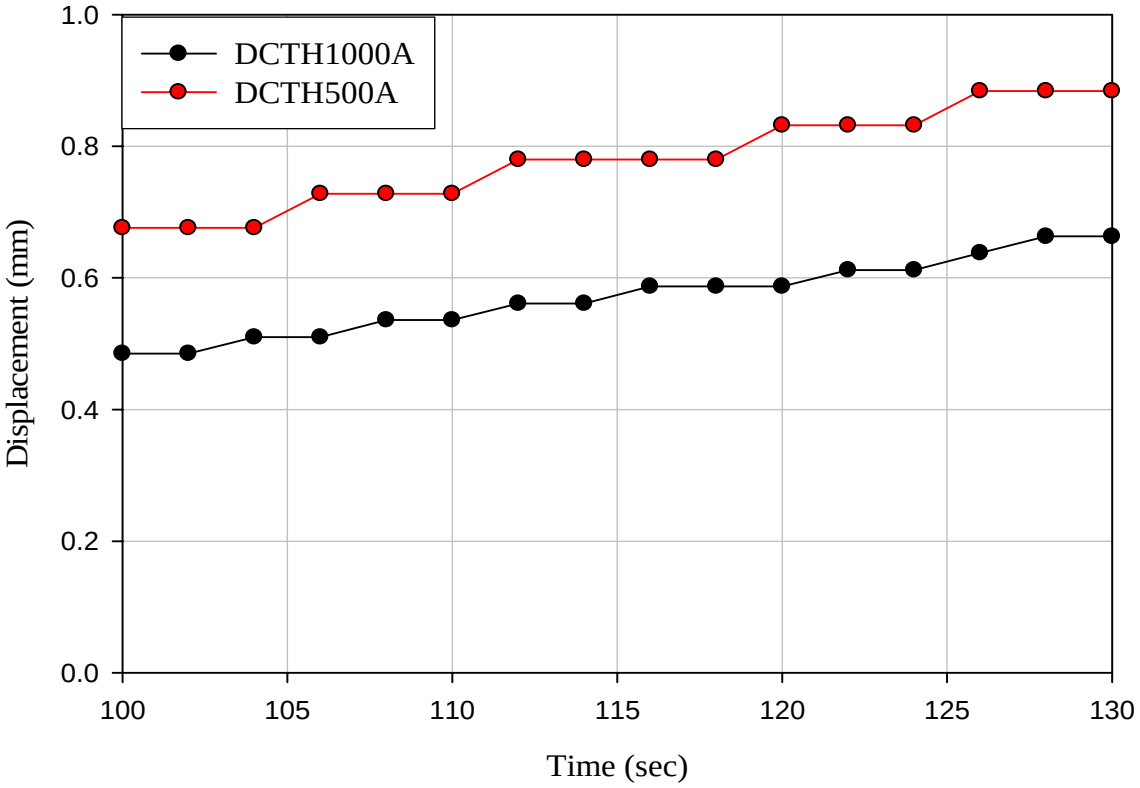

Figure 3.8 Displacement versus time for the DCTH1000A and DCTH500A LVDT's

Figure 3.9 Loading Frame

Two different pressure control systems were used for the different tests. The pressure system shown in Figure 3.10 has a confining pressure capacity of 200 kPa and was used for the 25 kPa and the 100 kPa experiments. On the control panel there are regulators for the cell pressure and vacuum. Behind the board there are two Differential Pressure Transducers (DPT) with capacities of 0.8 kPa (0.125 psi) and 220 kPa (32 psi). The pressure reservoir consists of two cylinders with deaired water, one inside the other. The inner cylinder is the volume change reservoir while the outer is used to apply the cell pressure. To apply the cell pressure, the top of the reservoir is pressurized with air. During the test, the DPT's measure the changes in cell pressure caused by the changes in the volume of the specimen. When the specimen expands, water is purged out of the cell to the inner cylinder and vice versa. These changes in pressure are converted to volume using the water level difference between the inner and outer cylinders. The other pressure control system (Figure 3.11) has a maximum capacity of 550 kPa and was used for the 250 kPa and 400 kPa confining pressure experiments. A regulator controls the pressure in the cell, which is supplied from the two burettes on the side of the panel.

The data acquisition system consists of a data acquisition unit and a computer with LabView software. The data acquisition unit (Figure 3.12) captures the voltage change of the instruments during testing and the signal is sent to the computer via a data acquisition card. A LabView program was custom-written for the experiments to acquire data, perform calculations, and display results numerically and graphically (Figure 3.13).

3.3.3 Specimen Preparation

The specimens were prepared in an aluminum split mold which measures 71 mm (2.8 in) in diameter (Figure 3.14). A cylindrical latex membrane was attached to the bottom endplate using an O-ring; and the mold was placed around the endplate. The membrane was stretched

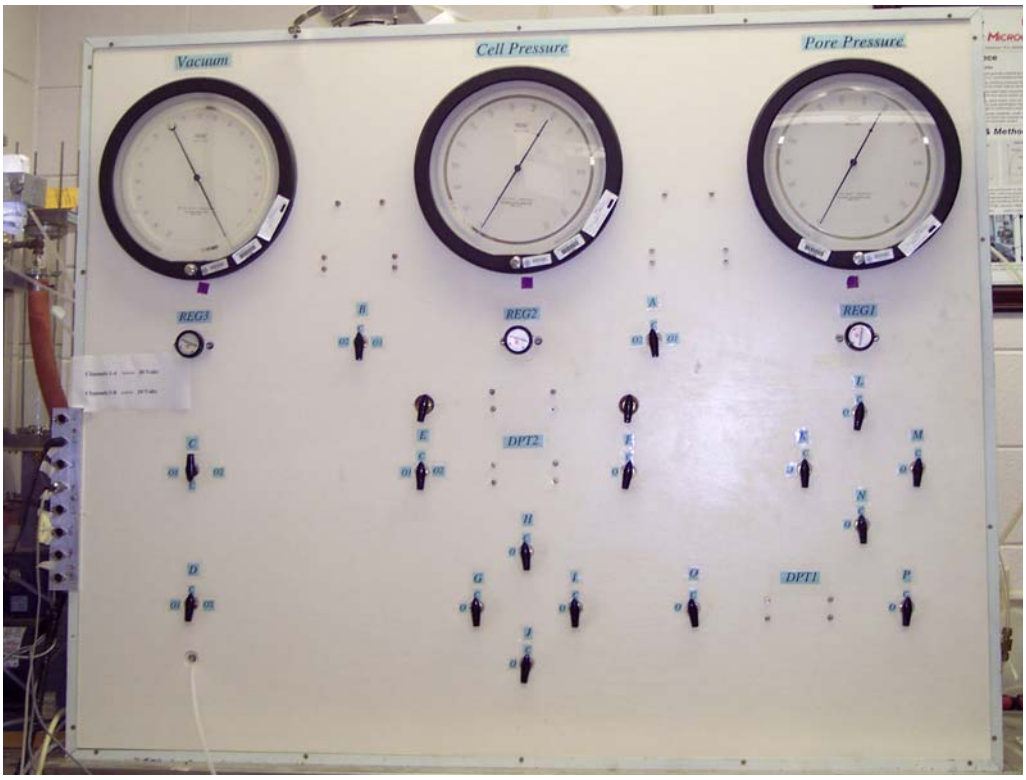

Figure 3.10 The 200 kPa confining pressure control system


Figure 3.11 The 550 kPa confining pressure control system

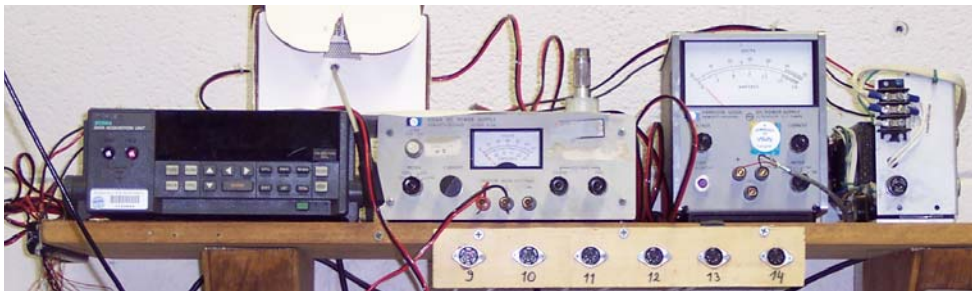

Figure 3.12 Data Acquistion System

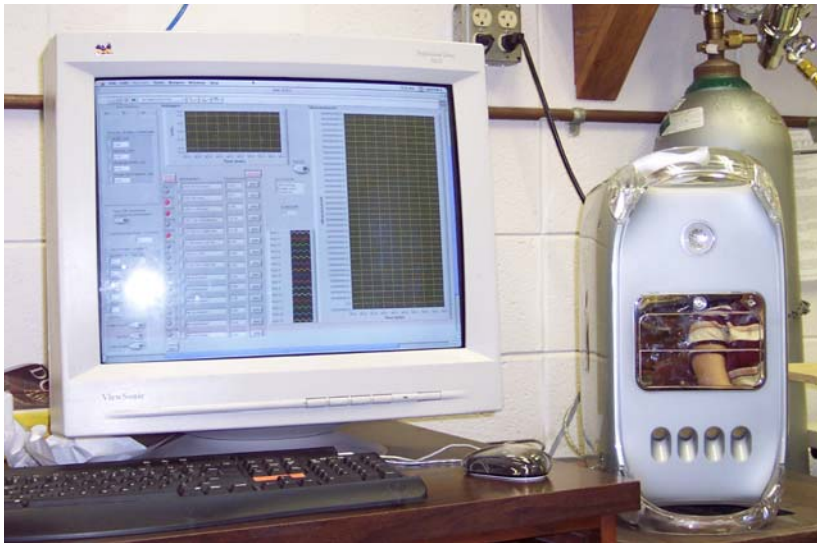

Figure 3.13 Computer with LabView Software

around the mold and a vacuum of 20 kPa was applied to the mold. The membrane was then filled with the beads in layers of approximately 36 mm (1.4 in). Each layer was tapped gently with a plastic rod (Figure 3.15 a). When the mold was completely filled, the excess beads were removed and the weight of the specimen was recorded. The top endplate was attached with an O-ring and a 20 kPa pressure was applied inside the specimen and the vacuum pressure was vented. The mold was carefully split to prevent disturbance to the specimen. The cell jacket and loading ram were then assembled.

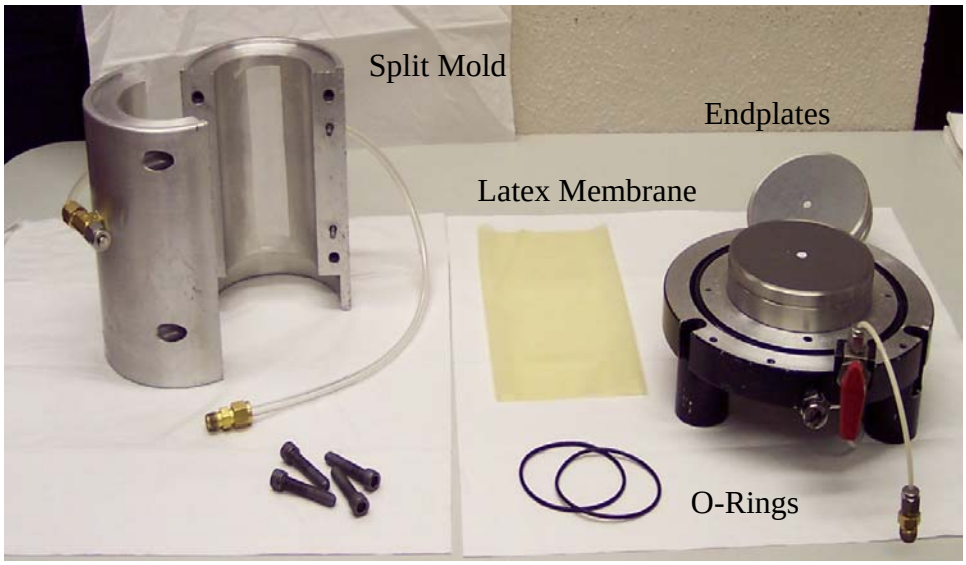

Figure 3.14 Parts used for specimen preparation

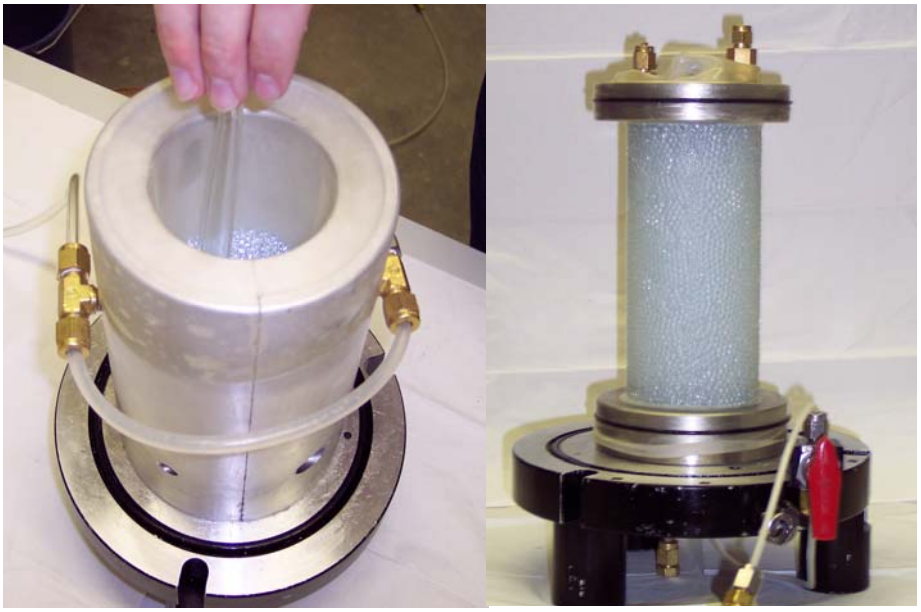

(a) (b)

Figure 3.15 (a) Glass beads being tapped with plastic rod (b) Assembled specimen

3.3.4 Apparatus Preparation

When the test cell was completely assembled, it was placed on the loading frame. The LVDT and load cell were mounted; the cell was then filled with water. The vacuum was reduced

while pressure was applied until the desired value was reached. The vacuum was vented, and then the test was commenced.

3.3.5 Conventional Triaxial Compression Testing Procedure

Conventional drained triaxial compression (CTC) experiments were carried out on the specimens. Each specimen was compressed under a constant rate of displacement of 0.5 mm/min. The LVDT measures the axial displacement of the triaxial cell relative to the load frame. Specimens were compressed up to 25% axial strain. Measurements included axial load, specimen deformation, cell pressure, and volume change. Drained CTC tests were performed on the glass beads with different test parameters of particles size, confining pressure, uniformity, loading rate, density, and endplates. The following tests were performed.

Table 3.6: List of Experiments

Beads	Filename	Pressure (kPa)	Void Ratio	Bulk Density (g/cm^3)	Load Cell (lb)
Very Small	vs25kpa,10,14	25	0.614	1.55	90
	vs100kpa,8,5	100	0.605	1.56	250
	vs250kpa,10,12	250	0.610	1.55	1000
	vs100kpa,9,10	400	0.613	1.55	1000
	CT Scan: vs_1, vs_2	25	0.604	1.55	90
Small	ss25kpa,5,31	25	0.561	1.60	90
	ss100kpa,7,29	100	0.568	1.59	250
	ss250kpa,11,21	250	0.576	1.59	1000
	ss400kpa,6,24	400	0.566	1.60	1000
Medium	ms25kpa,9,8	25	0.611	1.61	90
	ms100kpa,7,30	100	0.615	1.60	250
	ms250kpa,4,1	250	0.638	1.58	1000
	ms400kpa,9,8	400	0.610	1.61	1000
	CT Scan: ms_1, ms_2	25	0.60	1.62	90
Large	ls25kpa,	25	0.609	1.58	90
	ls100kpa	100	0.632	1.56	250
	ls250kpa	250	0.631	1.56	1000
	ls400kpa	400	0.624	1.57	1000
Well-graded	wg25kpa	25	0.371	1.82	90
	wg100kpa	100	0.392	1.80	250
	wg250kpa	250	0.371	1.82	1000
	wg400kpa	400	0.378	1.81	1000
	CT Scan: wg_1, wg_2	25	0.402	1.82	90
Strain Rate influence	ss25kpa,11,18	25	0.571	1.59	90
Density	ss25kpa,6,16	25	0.623	1.54	90
	ss25kpa,5,31	25	0.561	1.60	90
Endplates	ss25kpa,5,31	25	0.561	1.60	90
	ss25kpa,6,3	25	0.574	1.59	90

CHAPTER 4

EXPERIMENTAL RESULTS

4.1 Introduction

The results of the axisymmetric triaxial compression experiments that were reported in Chapter 3 are described in this chapter. The tests were performed for each combination of test conditions (beads size and confining pressure). The results are presented by displaying the principal stress ratio (σ_1/σ_3) versus nominal axial strain and volumetric strain versus axial strain. The volume increase (dilation) is taken as negative. Most experiments were carried out until 20% nominal axial strain; however, the glass beads punctured the latex membrane during some experiments, and tests were terminated at smaller axial strains.

4.2 Stress-Strain and Volumetric Strain Behavior

The results from the axisymmetric triaxial compression experiments (listed in Table 3.6) for the five different size glass beads at different confining pressures are shown in Figures 4.1 through 4.5. In general, a slight post peak principal stress softening is observed; after which, the principal stress ratio decreases at a very small rate. On the other hand, all experiments exhibited a continuous volume increase (dilation), even at relatively high strains. The oscillations in the responses will be discussed in section 4.4.

Figure 4.1 presents the axial strain versus principal stress ratio and axial strain versus volumetric strain for the very small glass beads. For the stress-strain curves of the four tests, a post peak softening is observed. The volumetric strain curves for the four tests show a continuous increase in volume change throughout the tests. Oscillations are observed in all tests;

however, they appeared in the post peak stage for the 25 kPa and 100 kPa experiments; whereas the oscillation was observed at earlier stages (i.e. during the hardening regime) for the 250 kPa and 400 kPa confining pressure experiments. The oscillation in the volumetric strain responses is less pronounced when compared to σ_1/σ_3 measurements. This might be due to smaller global volume change due to slip-stick between particles which causes the stress/load oscillation.

Figure 4.2 shows the axial strain versus principal stress ratio and axial stain versus volumetric strain for the small glass beads. The post peak softening is also observed in the 25 kPa and 100 kPa experiments. The other curves decrease slowly until a residual (plateau) condition was reached. Like the very small beads, the volume change increases throughout the test, and a critical state condition is not attained. Oscillations in stress response were observed in all responses for this class of beads; also they appear before the peak stress ratio. The oscillations were also noticed in the volumetric strain curves and they are noticeable when compared to the very small glass beads.

Figure 4.3 presents the axial strain versus principal stress ratio and axial strain versus volumetric strain for the medium glass beads. A post peak softening is observed in all experiments. The volumetric strain curve is similar to those of the very small and small beads where the volume continues to increase throughout the tests. Oscillations appear in the 250 kPa and 400 kPa experiments. Only one large drop in the principal stress ratio was observed in the 250 kPa experiment at approximately 21% axial strain. Two major drops in the principal stress ratio in the 400 kPa experiment are recorded which is associated with a noticeable sudden reduction in the volumetric strain. Such responses are attributed to a collapse mechanism of the particles' column structure that forms inside the specimen. One also can notice that the 25 kPa

and 100 kPa experiments have minor oscillations in the principal stress ratio results and almost no oscillation in the volumetric strain responses.

Figure 4.4 presents the axial strain versus principal stress ratio and axial strain versus volumetric strain for the large glass beads. The post peak softening is also observed in the stress-strain curves. All specimens exhibit continuous volume increase throughout the test. Only small amplitude oscillations were observed in the large glass beads.

The axial strain versus principal stress ratio and axial strain versus volumetric strain for the well-graded glass beads are shown in Figure 4.5. In the stress-strain curves, the 25 kpa and the 100 kpa experiments show a post peak softening. The other two experiments slowly decrease after the peak principal stress is reached. The volumetric strain responses for the well-graded beads are different than that of the uniform beads when it continues to increase throughout the test, but the volumetric strain reaches a maximum of ~4%. The uniform glass beads have reached a maximum of ~8% volumetric strain. This is logical since a well-graded specimen is expected to have less volume change because small particles will fill the voids between the large particles.

From these tests we can make two observations: the load oscillations and the continuous volume increase even at large strains. A thorough analysis of load oscillations and their occurrences will be discussed later in this chapter. The continuous volume increase observed even at high strains is caused by the shape of the particles. Since the particles are smooth and spherical, they do not interlock with each other, causing the beads to roll over each other and they continuously roll and slide and cause the volume to increase.

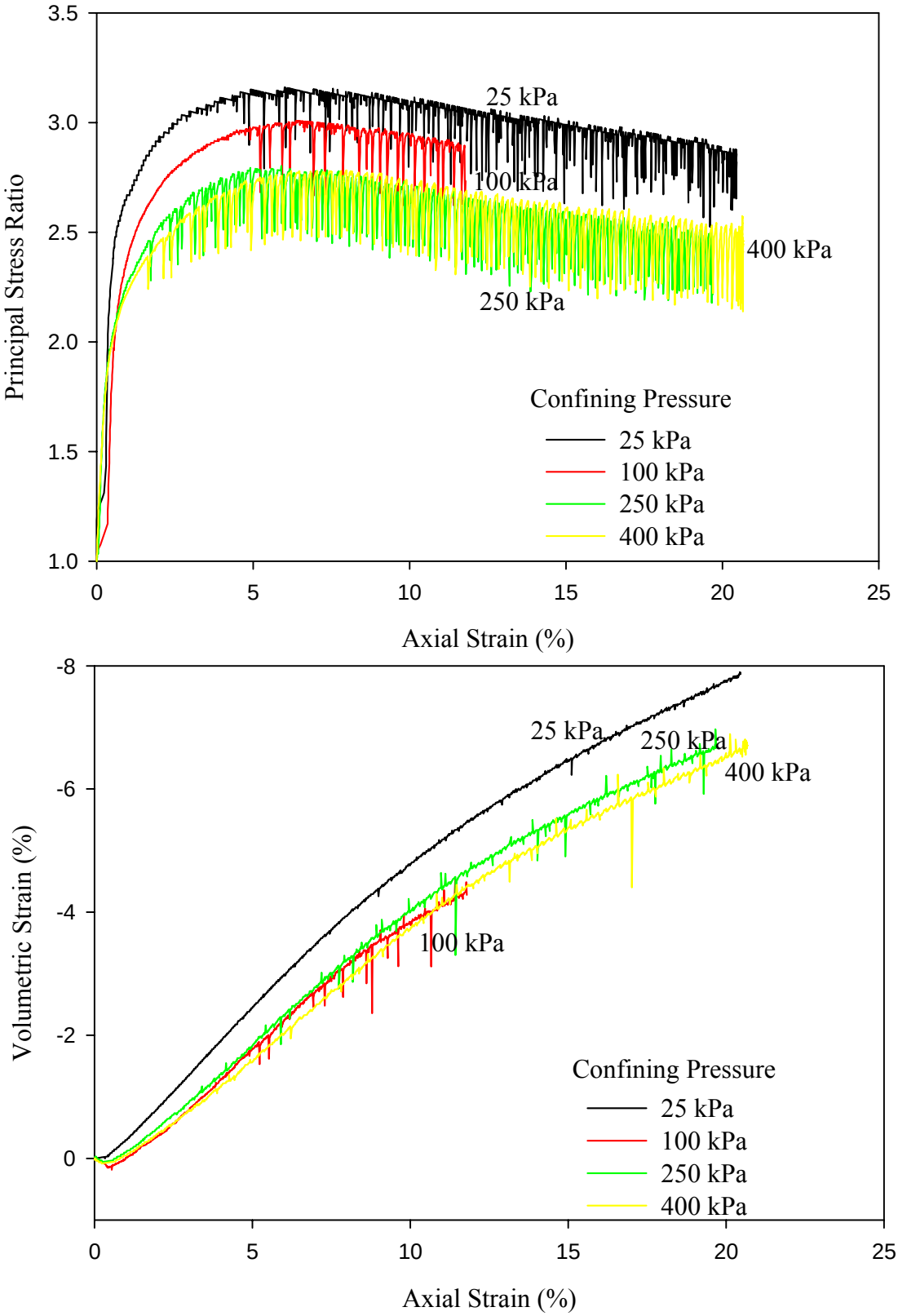

Figure 4.1 Axial strain versus volumetric strain and axial strain versus principal stress ratio for the very small glass beads

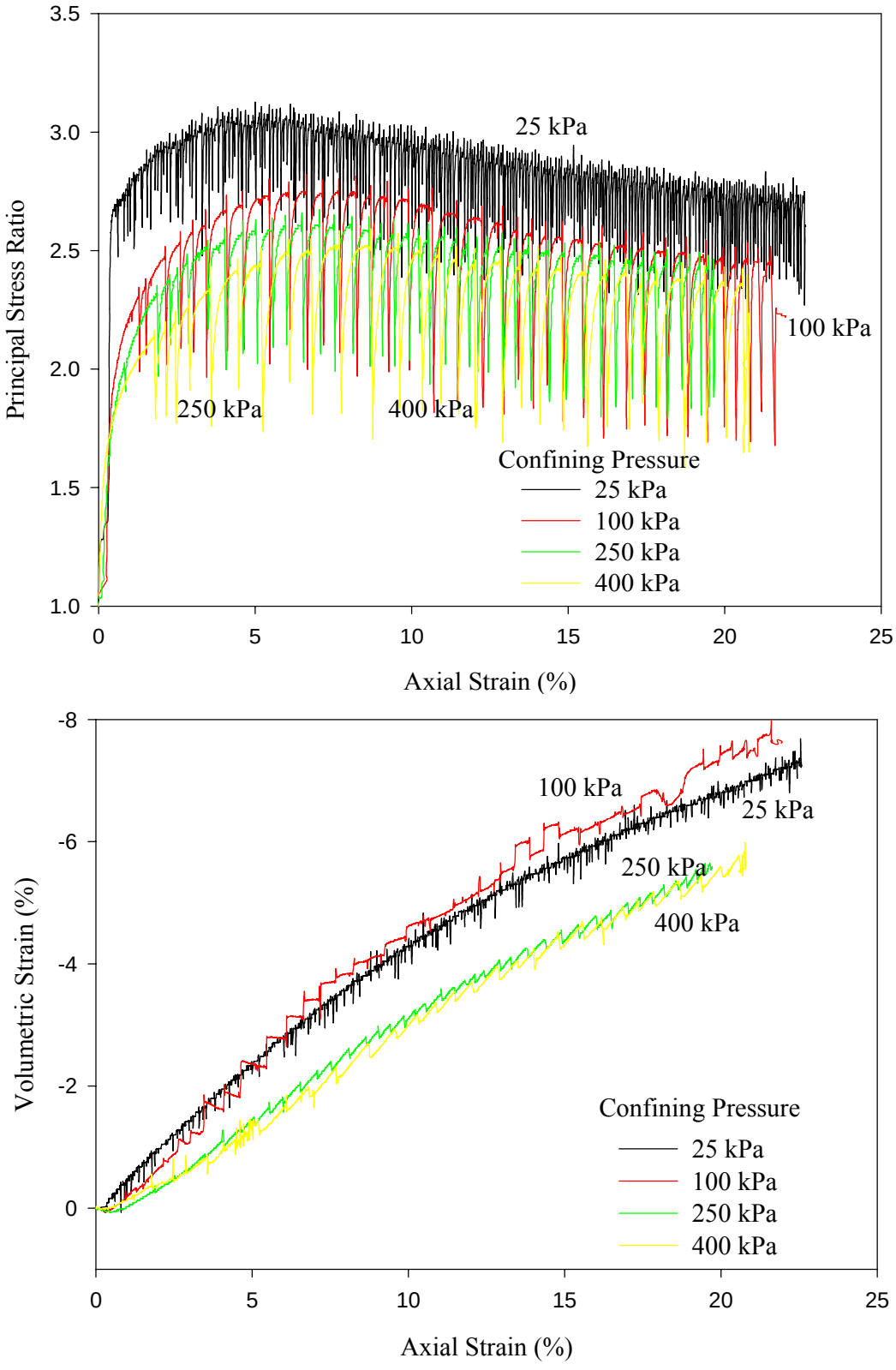

Figure 4.2 Axial strain verus volumetric strain and axial strain versus principal stress ratio for the small glass beads

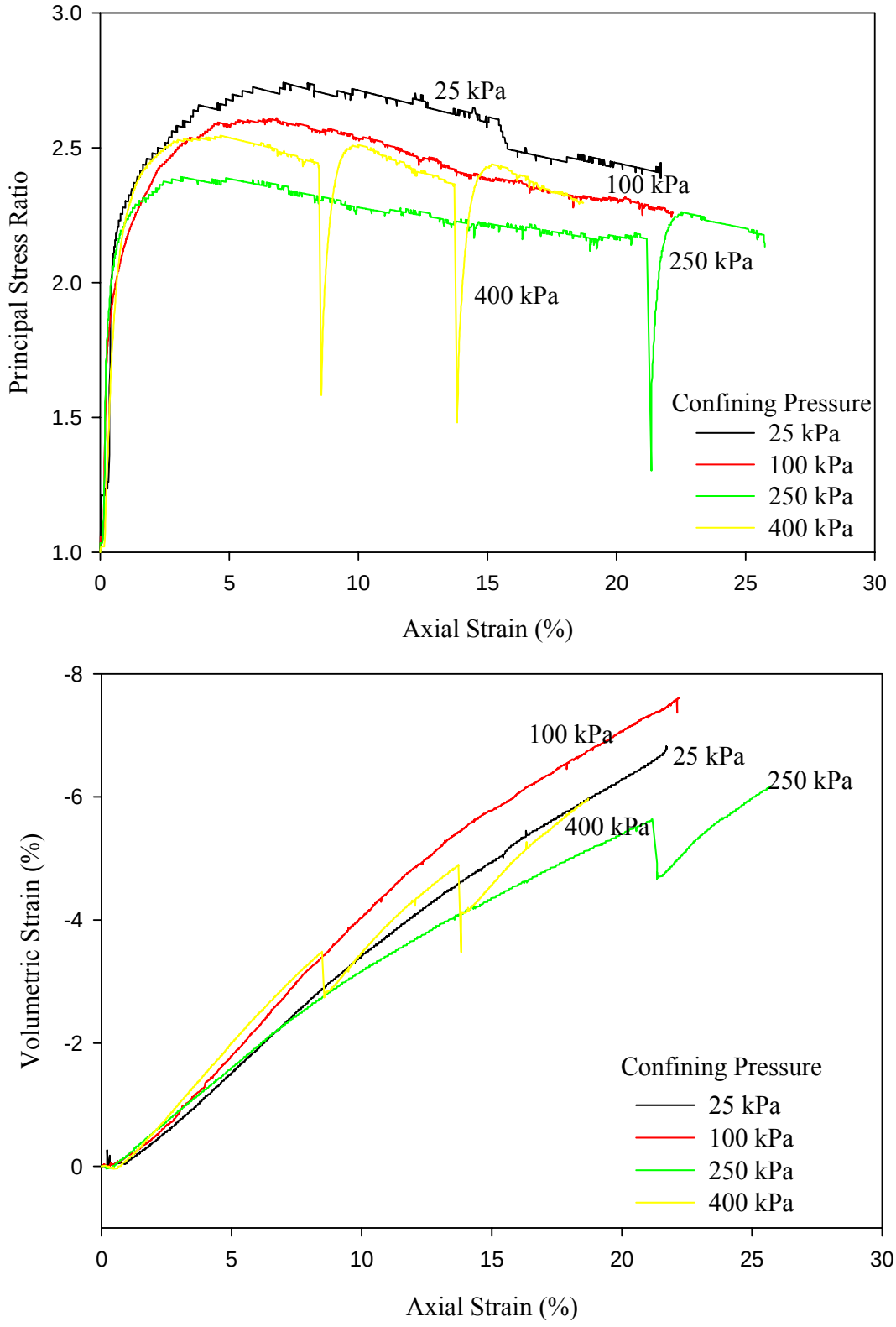

Figure 4.3 Axial strain versus volumetric strain and axial strain versus principal stress ratio for the medium glass beads

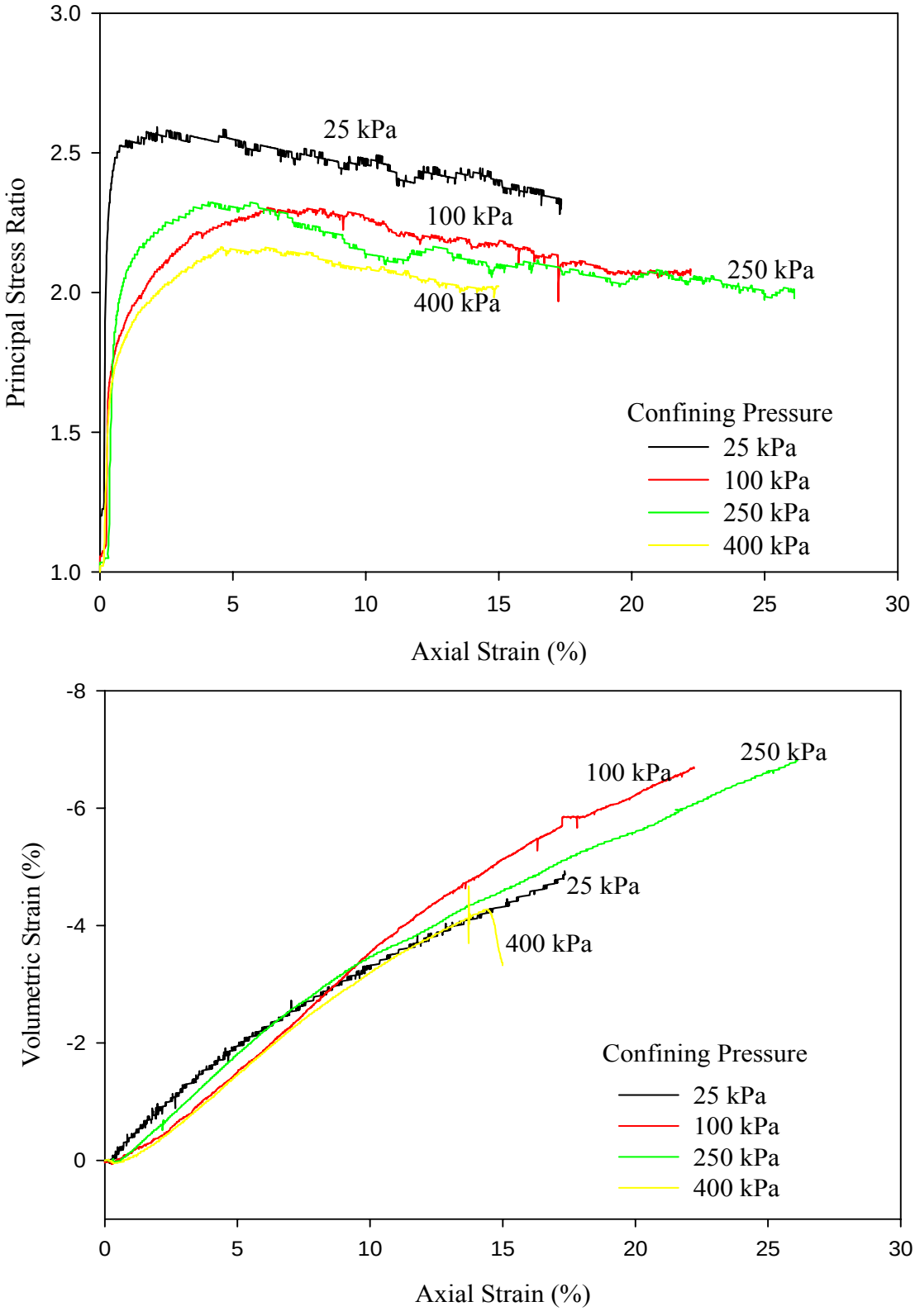

Figure 4.4 Axial strain versus volumetric strain and axial strain versus principal stress ratio for the large glass beads

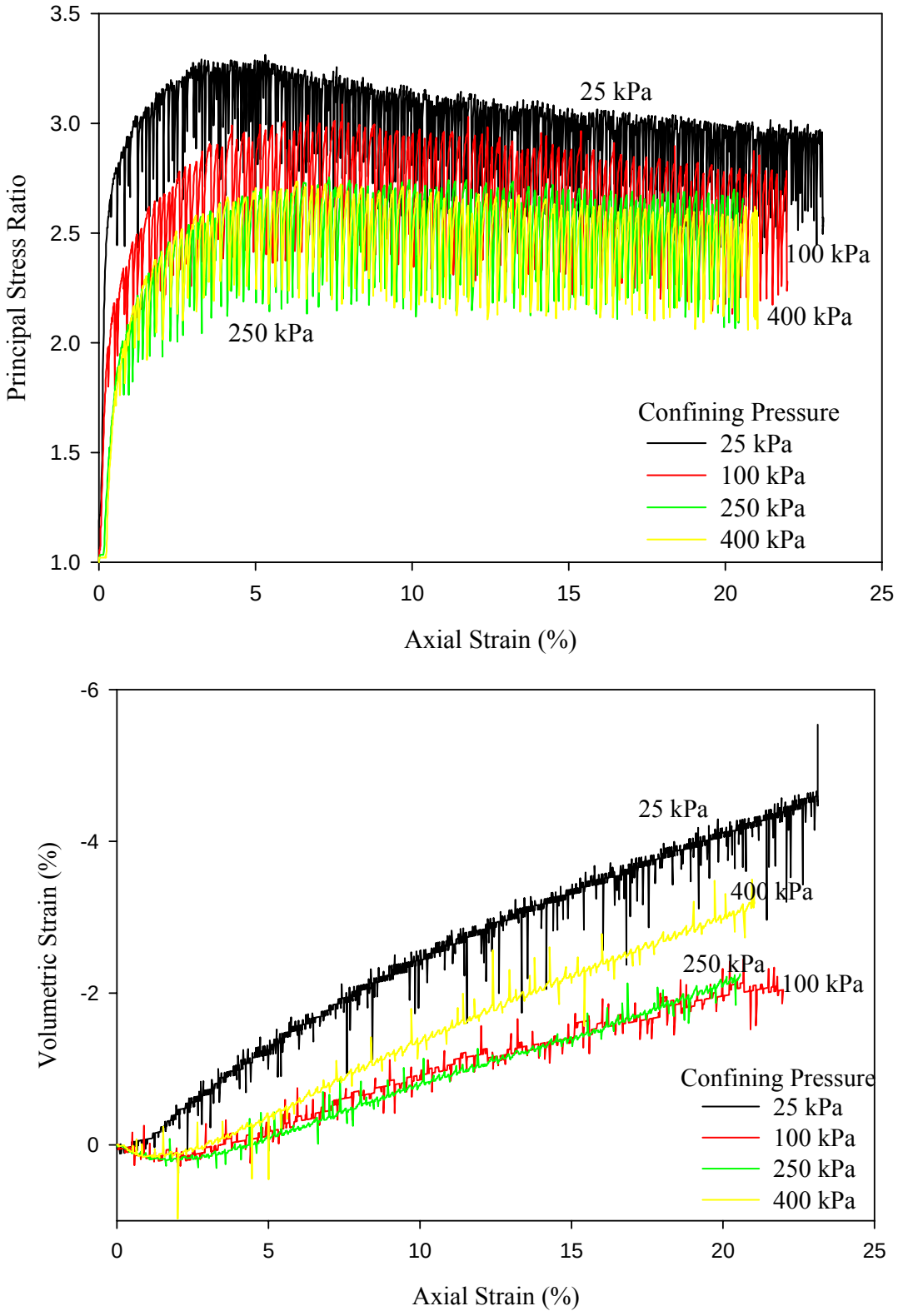

Figure 4.5 Axial strain versus volumetric strain and axial strain versus principal stress ratio for the well-graded glass beads

4.3 Peak Friction and Dilatancy Angles

The peak friction and the dilatancy angles for all experiments were calculated and are summarized in Table 4.1. The peak fiction angle was calculated using the following equation:

$$\phi`_p = \sin^{-1}\left(\frac{\sigma`_1 - \sigma`_3}{\sigma`_1 + \sigma`_3}\right)_p \tag{4.1}$$

The dilatancy angle was calculated from the maximum slope of the volumetric strain versus axial strain curves. The steepest part of the $\frac{d\varepsilon_v}{d\varepsilon_a}$ curves was used for the calculation, where $\frac{d\varepsilon_v}{d\varepsilon_a}$ is taken as positive for dilation.

$$\psi = \sin^{-1}\left(\frac{\frac{d\varepsilon_v}{d\varepsilon_a}}{2 + \frac{d\varepsilon_v}{d\varepsilon_a}}\right) \tag{4.2}$$

Table 4.1 Summary friction angle and dilatancy angle for experiments

Confining Pressure (kPa)	Very Small Glass Beads		Small Glass Beads		Medium Glass Beads		Large Glass Beads		Well-graded Glass Beads	
	$\phi`_p$ (deg)	ψ (deg)	$\phi`_p$ (deg)	ψ (deg)	$\phi`_p$ (deg)	ψ (deg)	$\phi`_p$ (deg)	ψ (deg)	$\phi`_p$ (deg)	ψ (deg)
25	31.3	12.3	30.9	9.7	27.7	10.6	26.3	9.5	32.4	8.2
100	30.1	10.9	27.9	12.2	26.5	12.2	23.2	9.9	30.7	3.6
250	28.3	10.5	26.7	10.5	24.2	8.5	23.5	9.9	27.9	3.7
400	28.1	9.6	25.6	7.9	25.8	10.8	21.6	9.4	27.7	6.0

The influence of the confining pressure (σ_3) on the peak friction angle is illustrated in Figure 4.6, which shows that the friction angle decreases as the confining pressure increases. The results are consistent with the literature and prove that as the confining pressure increases the

peak friction angle of the material decreases. Figure 4.6 also shows that the friction angle decreases as the particle size increases and the experiments on well-graded beads exhibited higher friction angles.

Dilatancy angle generally decreased as the confining pressure increases. However, the variation in ψ value is very small and within the margin of error of experimental measurements (Figure 4.7). The well-graded specimens have smaller ψ values when compared to uniform beads. It appears that particle sphericity is the main factor influencing the ψ-value. The experiments reported in this thesis are for spherical particles with no apparent influence of the particle size (for specimens composed of uniform particles) or the confining pressure on the ψ value.

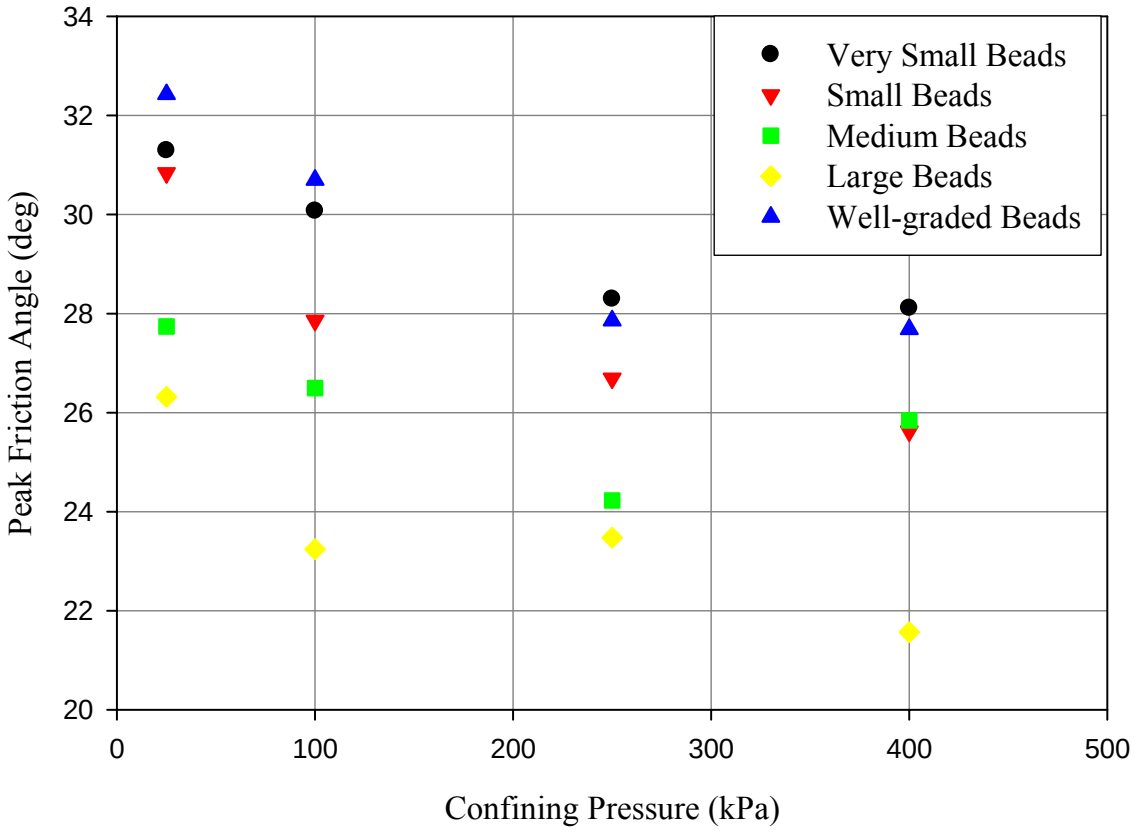

Figure 4.6 Peak friction angle verses cell pressure

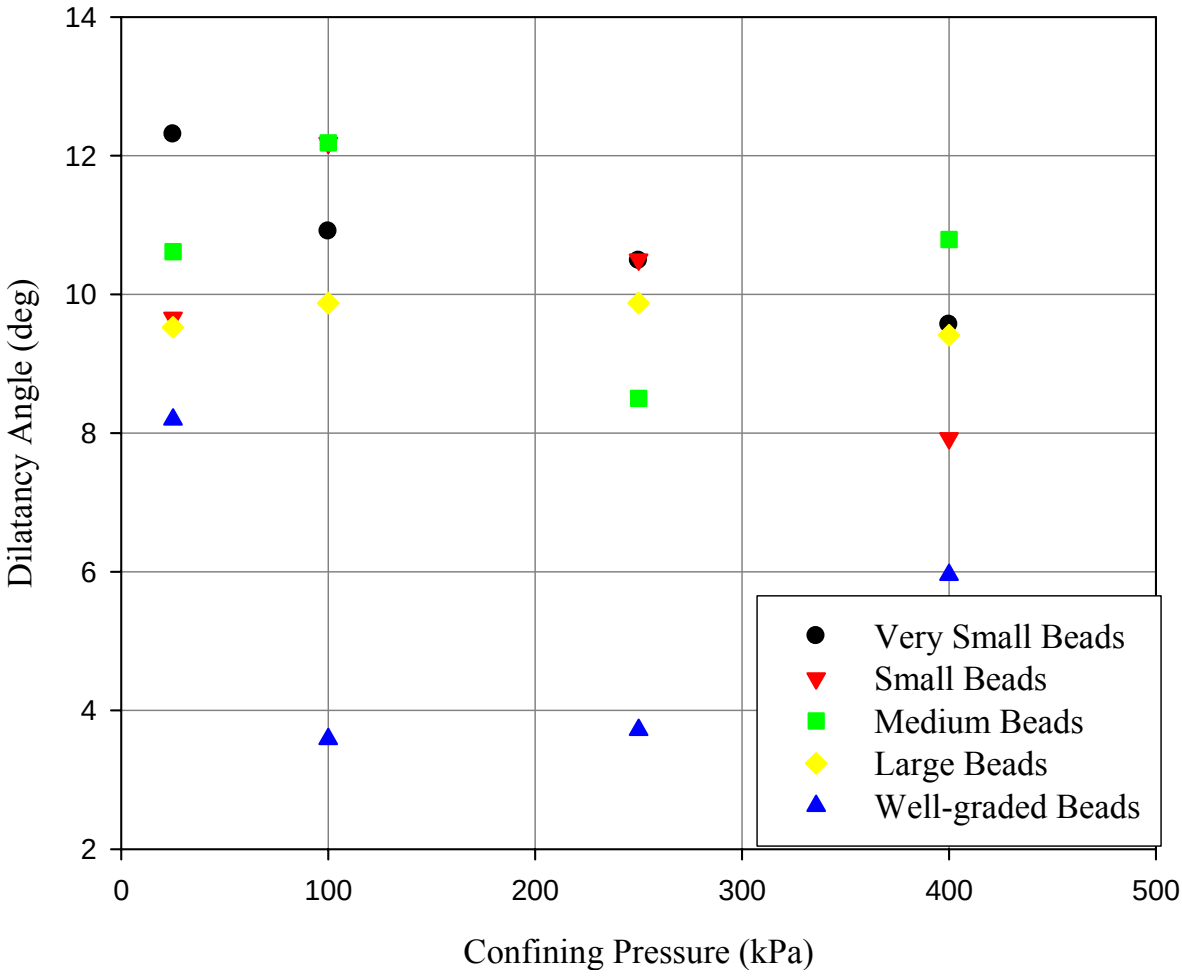

Figure 4.7 Dilatancy Angle verses cell pressure

4.4 Stick-Slip Behavior

In the stress-strain results, load oscillations were observed in the very small, small, and well-graded beads at each confining pressure. For the medium beads, the oscillations appeared at high confining pressure (250 kPa and 400 kPa), and they did not appear in the large beads.

To further analyze the oscillations in the test results, the following terminologies are defined: DSA is the deviator stress amplitude, which is the difference between the highest and

the lowest values of the deviator stress, and the oscillation period is defined as the difference in the axial strain as illustrated in Figure 4.8.

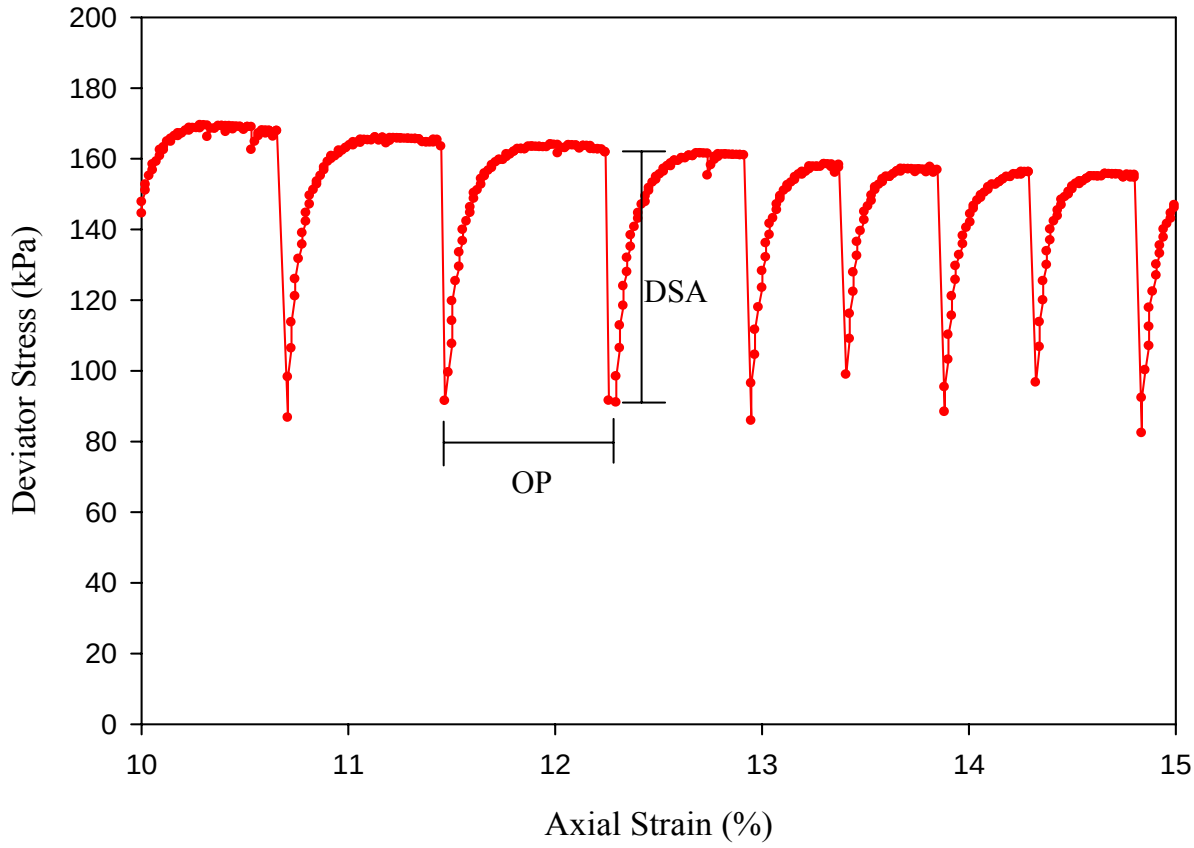

Figure 4.8 Definition of DSA and OP

4.4.1 Possible Causes of Load Oscillations

To eliminate the possibility of limitations of data acquisition, sensor limitations on the observed principal stress oscillations, the following investigation was carried out.

4.4.1.1 Data Acquisition

To test the data acquisition system, two factors were considered: loading strain rate and data acquisition. A test was carried out on the small glass beads at 25 kPa, and the strain rate was changed during the course of the experiment to investigate the influence of the loading rate on the DSA and the OP. Figure 4.9 shows the test results from the experiment and the stages where

the strain rate was changed during testing. The DSA and OP were calculated for the experiment. The influence of loading rate on the DSA and the OP are shown in Figures 4.10 and 4.11, respectively, which show that the DSA and OP decrease as the loading rate increases. The load oscillations diminish as the loading rate increases since fast loading rate will reduce the possibility of triggering more frequent collapse of chains of particles and have less frequency of oscillations.

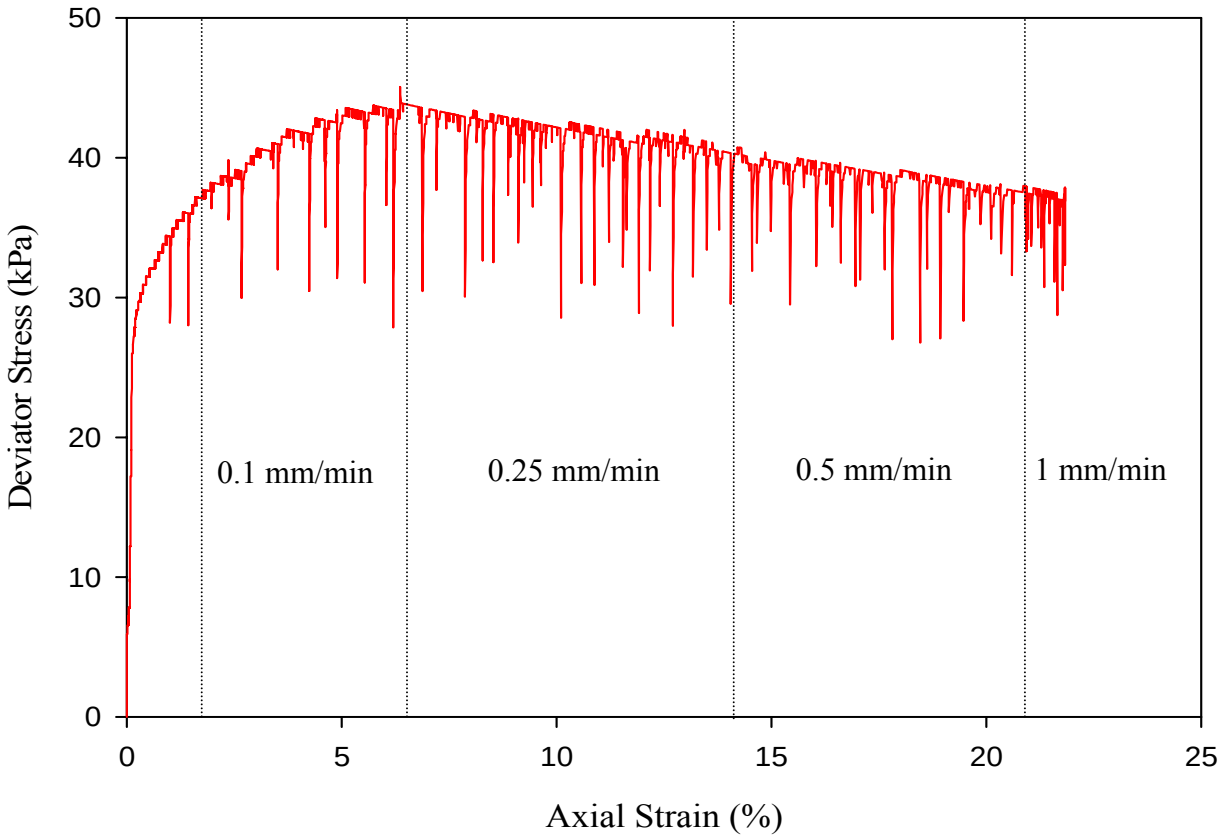

Figure 4.9 Test Results from the small glass beads tested at 25 kPa confining pressure and changing the loading rate throughout the test

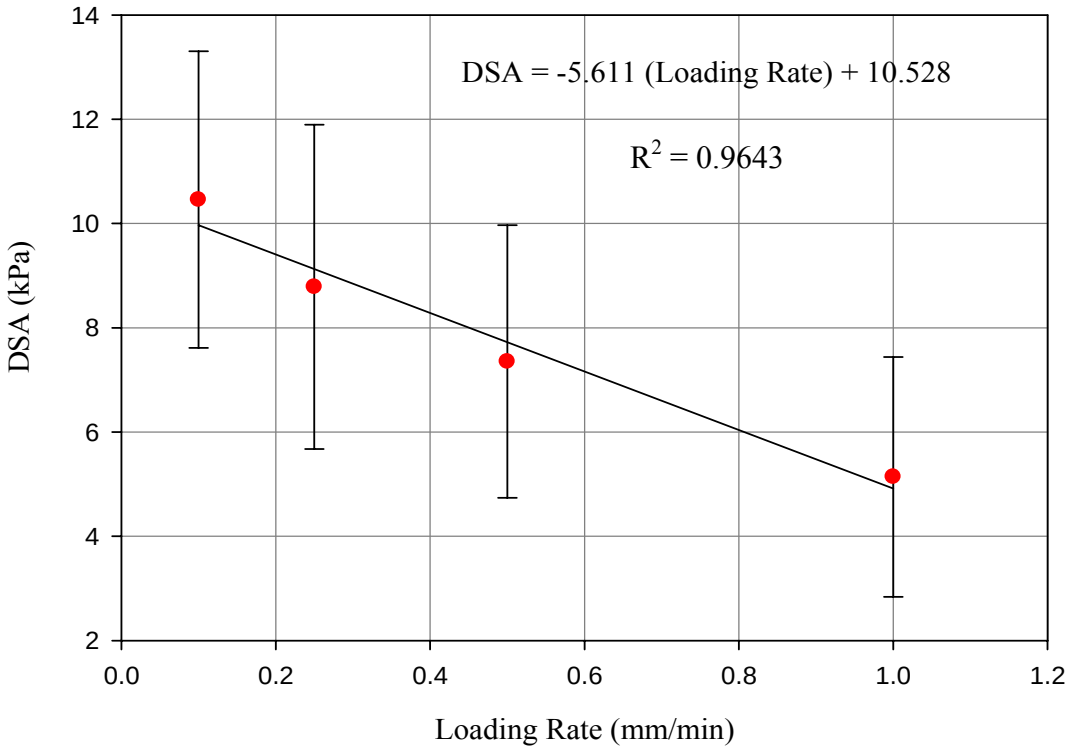

Figure 4.10 Influence of loading rate on deviator stress amplitude (DSA)

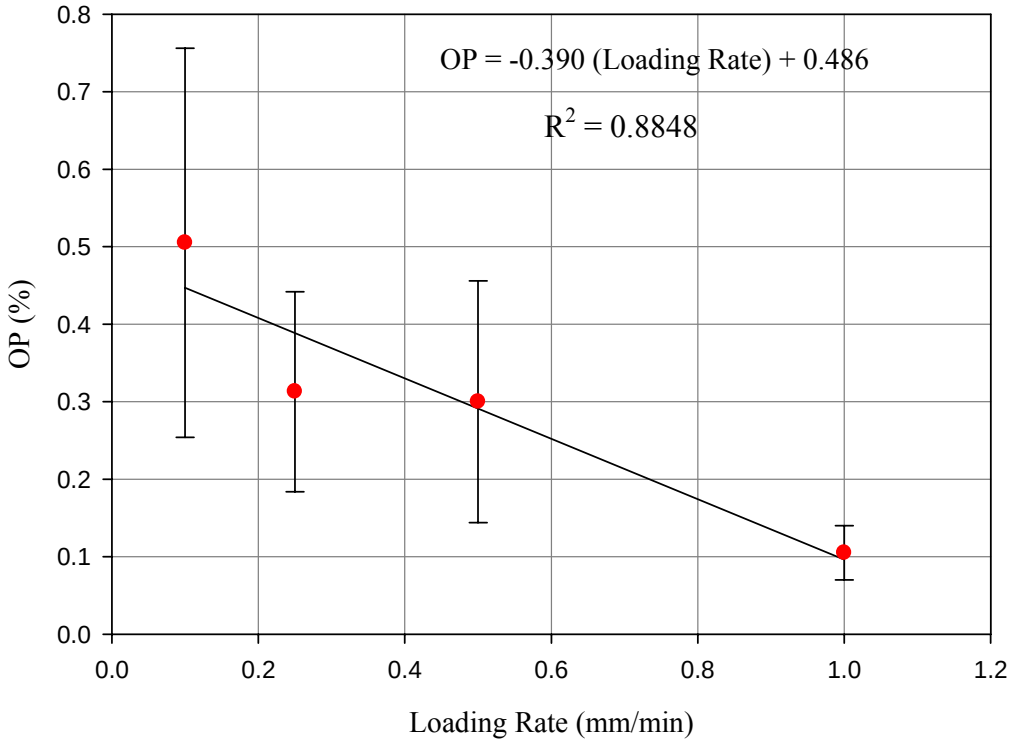

Figure 4.11 Influence of loading rate on oscillation period (OP)

The data acquisition scan interval time was also investigated. The data acquisition system had 14 channels. When it is scanned at every second, it never completes scanning all 14 channels. In order to get a complete scan, the scan time was changed to two seconds. After changing this, the data did not have many points that overlapped. This had no effect on the stick-slip behavior that occurred in the specimens during testing.

4.4.1.2 Material

Possible causes of load oscillations are the specimen density and the friction between the endplates and the specimen. Experiments were conducted on two specimens using small glass beads at 25 kPa at 1.54g/cm^3 (loose) and 1.60g/cm^3 (dense). The results are illustrated in Figure 4.12 and the DSA and OP were calculated for the tests and the difference was negligible when comparing the two cases. For this study the bulk density of the specimen does not affect the stick-slip behavior in the glass beads. However in the literature, it was found that as bulk density increases, the stick-slip behavior disappears (Adjemian and Evesque 2004).

Table 4.2 Deviator Stress Amplitude and Oscillation Period for dense and loose specimens of small glass beads

Density	**DSA (kPa)**	**OP (%)**
loose	10.53	0.12
dense	9.99	0.15

Experiments were also performed using the acrylic endplates with a diameter that matches the diameter of the specimen. They have a pyrex glass facing which has a relatively low coefficient of friction and the enlarged stainless steel endplates with polished tungsten carbide facings. The results are shown in Figure 4.13. The DSA and OP were calculated for both endplates (Table

4.3). The differences in the DSA and OP for the two tests were also negligible. Therefore the endplate facing does not influence the stick-slip behavior.

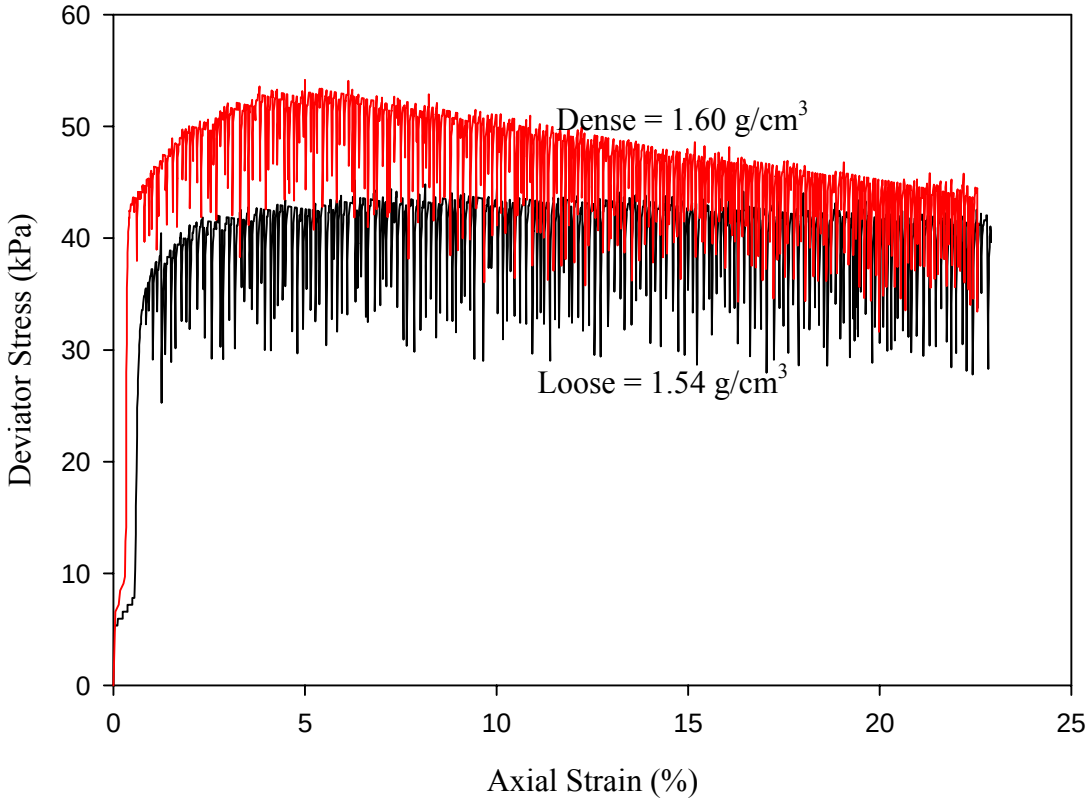

Figure 4.12 Influence of density on the DSA and OP for small glass beads

Table 4.3 The influence of endplates on DSA and OP on small glass beads

Endplate facing	**DSA (kPa)**	**OP (%)**
pyrex glass	9.77	0.19
tungsten carbide	10.53	0.12

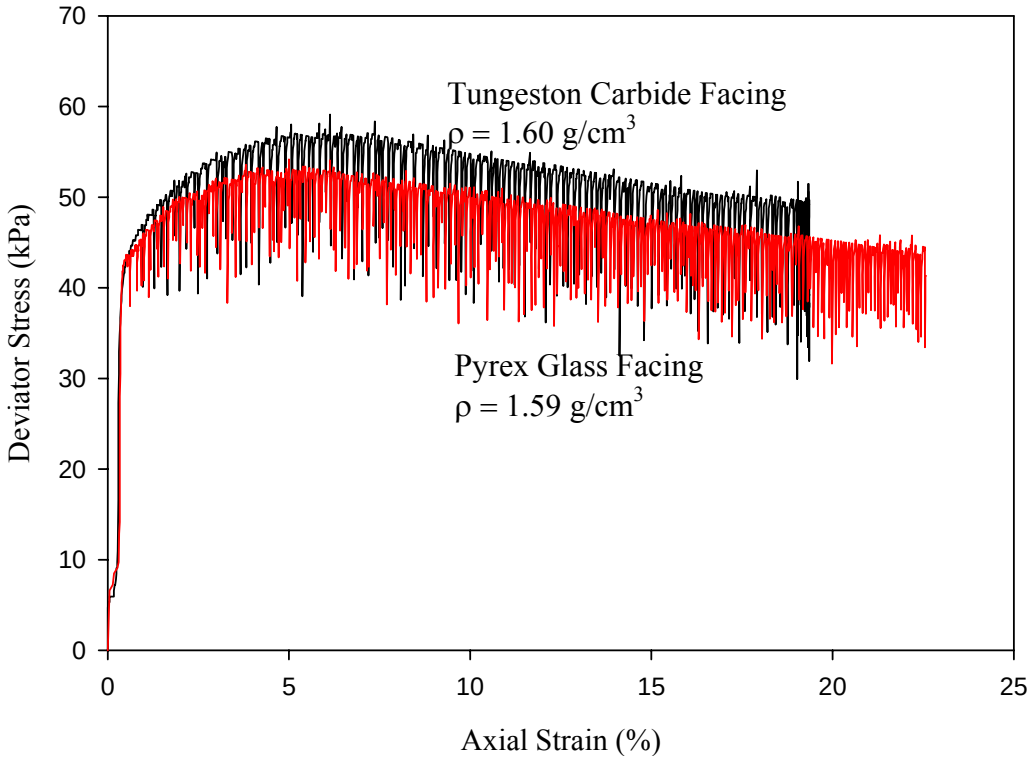

Figure 4.13 Test Results from the pyres glass facing and tungsten carbide facing endplates

4.4.2 Stick-slip Analysis from Test Results

The load oscillations may be due to the stick-slip between the glass beads. The beads form chains of particles to support the applied load. When the chain becomes unstable, some beads will slide out of the column causing the load to drop. This drop causes a sudden drop in the stresses during compression. The load then builds up again as new chains of columns form followed by collapse. Since the particles are spherical and smooth, they do not interlock with each other so they roll over one another.

Taking a close look at the test results of the small glass beads (Figure 4.14), one can notice that the DSA increased as the confining pressure increases. To examine this further, the DSA was calculated for the experiments that exhibited this behavior: very small, small, and well-

graded glass beads. A linear relationship was found between the DSA and the confining pressure (Figure 4.15). In Adjemian and Evesque's (2004) research, they used two different confining pressures (30 kPa and 60 kPa) and found that the change in deviator stress increased as confining pressure increases (Figure 2.10 (a)). Since they presented only two points, it is hard to conclude that this is a linear relationship. When the DSA was compared in relation to the mean grain size (d_{50}) for each experiment, the trend showed that the DSA increased as the grain size increased. The specimen composed of well-graded particles fall in between the very small and small particles (Figure 4.15).

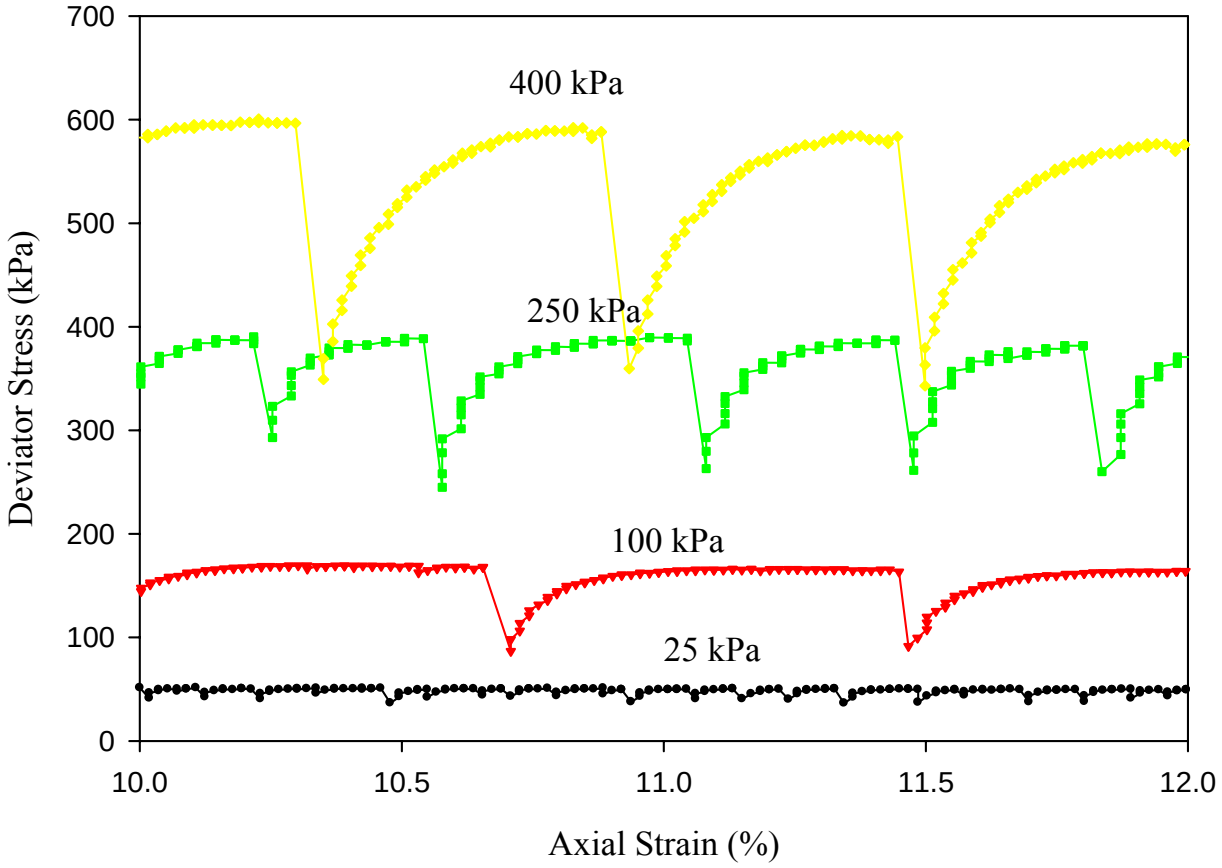

Figure 4.14 Close up of small glass bead test results for deviator stress versus axial strain

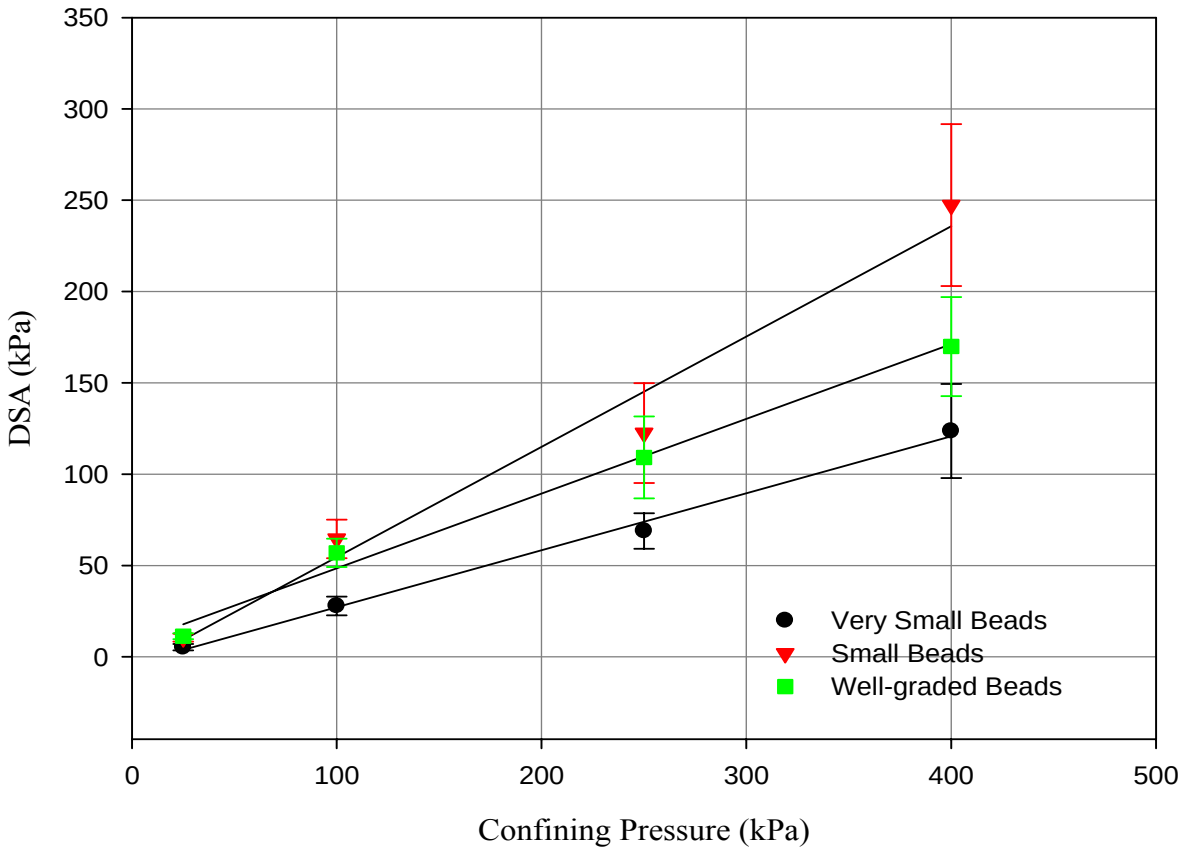

Figure 4.15 Influence of cell pressure on deviator stress amplitude

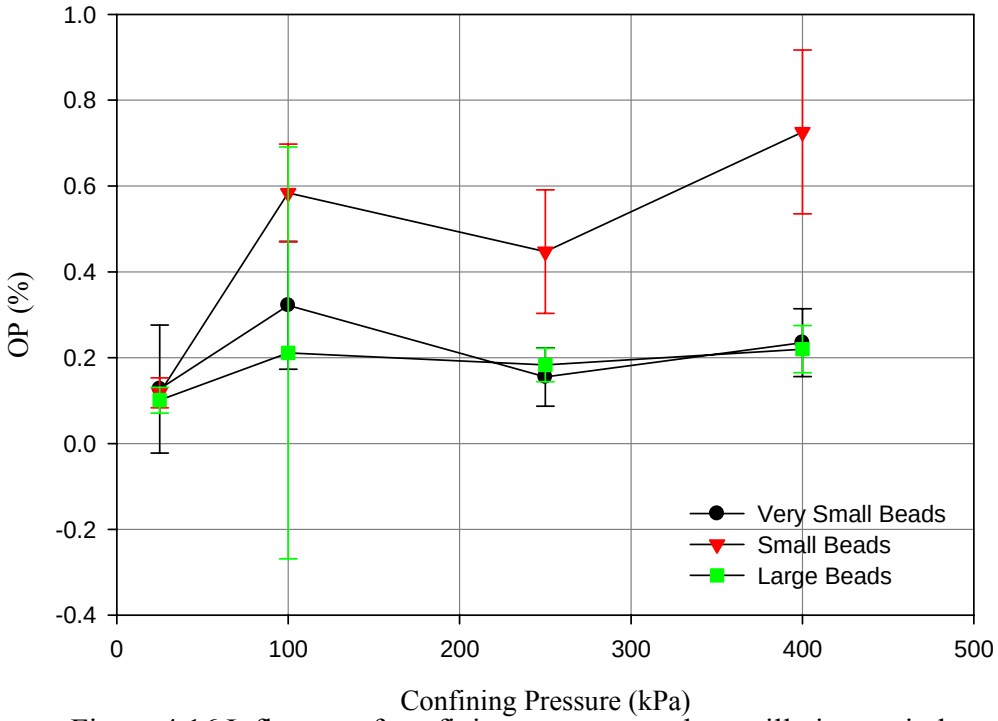

Figure 4.16 Influence of confining pressure on the oscillation period

The OP was also calculated for each experiment that exhibited stick-slip behavior (i.e., very small, small, and well-graded glass beads). Referring to Figure 4.9, the OP increased between the 25 kPa and 100 kPa experiments; however, it decreased between the 100 kPa and 250 kPa experiments and then increases again between 250 kPa and 400 kPa. When the OP was compared to the confining pressure, this trend was found for all of the experiments, not only for the small glass beads (Figure 4.11). In the Adjemian and Evesque's (2004) research (e.g., Figure 2.10 (b)), it was found that the OP decreased with an increase in confining pressure between 30 kPa and 60 kPa. They presented only two data points therefore it is difficult to describe this trend as a linear relationship. Figure 4.11 also shows the influence of the particle size on the oscillation period. For the uniform specimens, the OP increased with an increase in particle size. The well-graded beads had a smaller OP than the uniform particles because the smaller particles in the specimen were able to fill in the void spaces between the larger particles during compression.

The medium beads only show oscillations in the 250 kPa and 400 kPa experiments. For the large beads, no oscillations were found in the experiments. This is because the particles are larger and more stable when they form columns. It is known that the contact point between two rigid spherical particles is a point (Figure 4.17). For this study the glass beads are not perfectly rigid so there is a contact radius between the particles when the load is applied. The contact radius can be calculated using equation 4.3 (Santamarina et al. 2001).

$$r_c = R\sqrt[3]{\frac{3*(1-\upsilon_g)*N}{8*G_g*R^2}} \tag{4.3}$$

where N = applied load

R = radius of sphere

υ_g = Poisson's ratio = 0.23

G_g = shear stiffness = 25.61 GPa

The contribution area for one sphere in a simple cubic packing is $4R^2$. Therefore, one can estimate the normal load (N) through the contact between particles as $N = 4R^2\sigma$. The contact radius is a function of the applied stress to the particles and the diameter of the particle. As the stress and diameter increase, the contact radius increases. This allows the columns of particles to become more stable and they do not collapse. The calculated contact radius for each particle is represented in Figure 4.18.

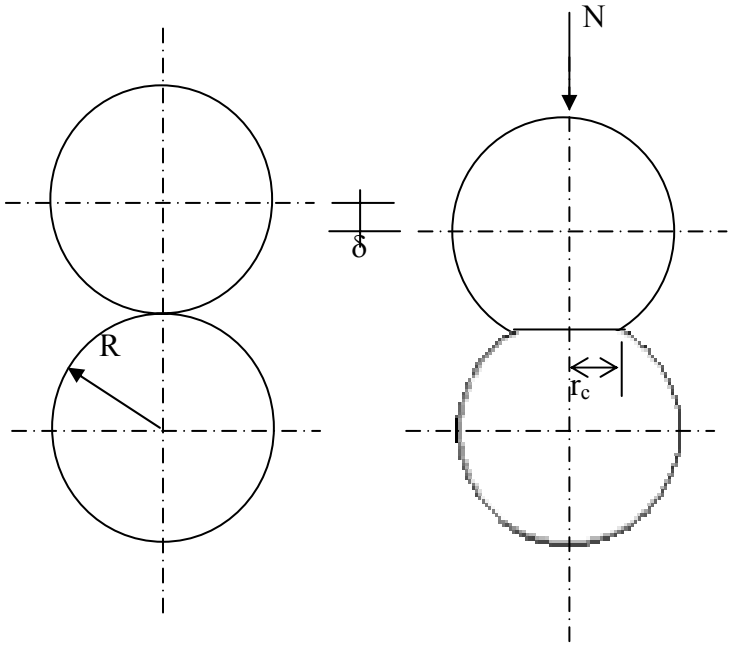

Figure 4.17 Schematic of column of spherical particles before and after compression (Santamaria et al. 2001)

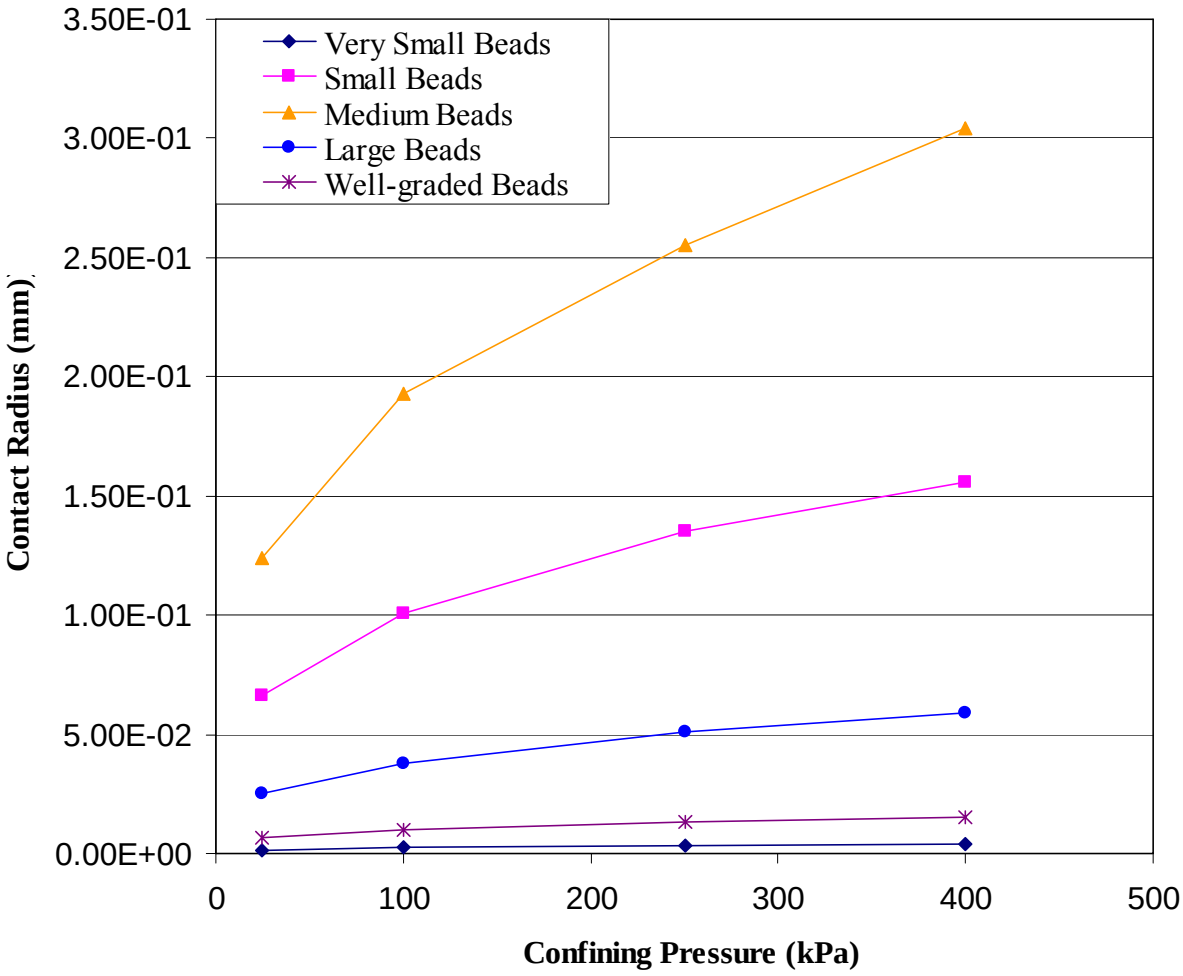

Figure 4.18 Influence of confining pressure on contact radius

CHAPTER 5

COMPUTED TOMOGRAPHY

5.1 Introduction

In 1895, the X-ray was discovered by Wilhelm Konrad Rontgen, a German physicist. He was awarded the first Noble Prize in physics in 1901 for his discovery. Since then, x-rays have been widely used in medicine to capture two and three-dimensional images of organs and tissues of the human body.

X-ray computed tomography is an imaging technique that produces a 2D image of a plane through a material. When the radiation passes through the matter, three different types of basic interactions take place: photoelectric effect, Compton scattering, and pair production. Different processes will dominate depending on the energy of the radiation. Photoelectric effect is the complete absorption of an incoming photon upon interaction with an electron. All of the energy of the photon is transferred to the electron. The Compton scattering process is the scattering of photons on initially free electrons. There are no free electrons in matter, but if the photon energy is large compared to the binding energy of the electron, and then the electron is considered free. The photon is not absorbed, and it loses energy and continues after a change of direction. Only the photons that have not undergone any interaction remain in the beam. As the beam goes through the matter and makes it to the detector, it is attenuated in intensity (KTH 2001).

The linear attenuation coefficient (μ) is the fractional change in intensity of the incident beam per unit thickness of the attenuating material, It is a function of the energy of the photons and the elemental composition of the attenuating material. The linear attenuation depends on the

density of the absorbing material, and it can be overcome by normalizing the linear attenuation coefficient for density. The normalized term is called the mass attenuation coefficient (μ_m)

$$\mu_m = \frac{\mu}{\rho} \tag{5.1}$$

This value can be found for different materials from the National Institute of Standards and Technology website. For composite materials, the sum of the mass attenuation of each material in the mixture is multiplied by the fraction of the weight (Michael 2001).

The CT scanner measures density as a CT number. Such numbers are directly proportional to the local electron density of the material under investigation. Each pixel represents a CT number which corresponds to color intensity between black and white. Low CT numbers appear in the reconstructed CT image as a dark grey or black pixel. An example of a low CT number is air. For denser materials, the pixel is assigned a lighter color or white. An example of a slice image is shown in Figure 5.1. Slices can be stacked together to create a volume of the scanned object (Figure 5.2).

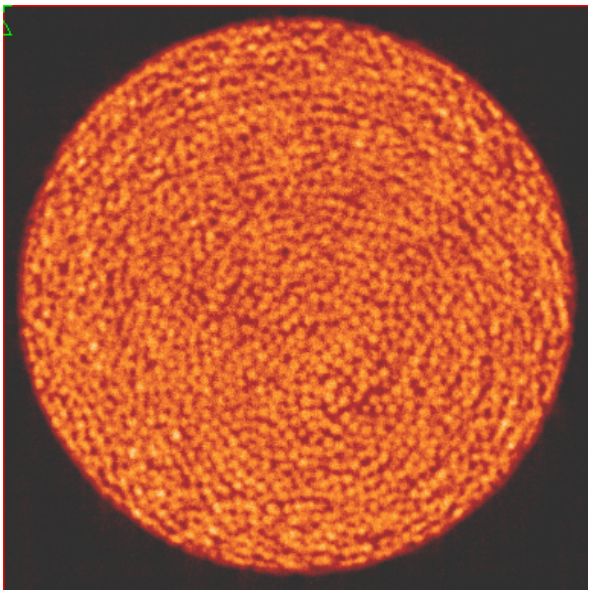

Figure 5.1 A slice from a triaxial specimen of glass beads

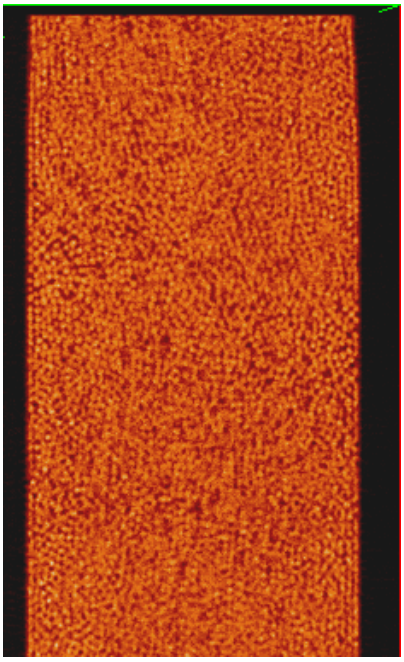

Figure 5.2 Vertical cross section of a volume image of a triaxial specimen composed of glass beads

5.2 Uses of Computed Tomography

There have been many developments in X-ray Computed Tomography (CT) outside of the medical field, especially in the oil industry where it has been used to evaluate the flow of different fluids through porous media (e.g. Angulo et al 1992). In industry, CT was initially used to scan wood and coal; however, today it is used for quality management, development, and analysis for materials and products. CT measures the transmitted intensity of a beam of radiation. The attenuation measurements over many views are collected, and a 2-D cross sectional area is mathematically reconstructed. This results in a map of linear attenuation coefficients for the cross section. The linear attenuation coefficient depends on the mass attenuation coefficient and the mass density. Using this, researchers were able to map the mass density of objects.

In geotechnical engineering, CT was used to study strain localization patterns (shear bands) in axisymmetric triaxial tests, void ratio variations in specimens, and to characterize the

failure of soils. It allows the observation of the evolution of the density inside the sand specimen without contact or destruction (e.g., Desrues 1996, Alshibli et al. 2000).

5.3 Computed Tomography Experimental Work

Three specimens were scanned using the CT system of NASA/ Marshall Space Flight Center before and after being subjected to axisymmetric triaxial compression in order to study the internal structure of the glass beads. This section describes the CT system used to scan the specimens, the procedure for specimen preparation, testing, and a list of the scanned experiments.

5.3.1 Apparatus Description

The apparatus used for the tests included the following: conventional triaxial cell, loading frame, and data acquisition system. The triaxial cell is the same as the one described in Section 3.3. The loading frame is also strain-controlled, with a load cell and an LVDT attached to it; and the data acquisition system consists of a personal computer with a test monitoring software. The CT system of the NASA Marshall Space Flight Center (MSFC) in Huntsville, Alabama was used to perform the CT scans. It is a Flash CT system manufactured by Hytec Incorporated (Figure 5.3) that produces cross sectional CT images and projects digital radiographs. The specimen is rotated so that the CT images are obtained. It has a great detection capability of extremely small cracks, porosity, and voids that are normally not visible with film radiographic inspection. The Computed Tomography system consists of the following:

- 450 kV x-ray source.
- Solid-state detector array (2048 channels, 200 μm aperture).
- 18-bit dynamic range data acquisition system.
- Slice width collimator.

- Dual Pentium III workstation, software, image processor, and color image display.
- Six axis machine tool grade precision manipulator with linear servo drives.
- Slice position indicator: red laser line illumination.
- Detector resolution up to 0.127 mm/pixel.

It uses a Flash CT-Viz software package to acquire, process, and visualize the CT images.

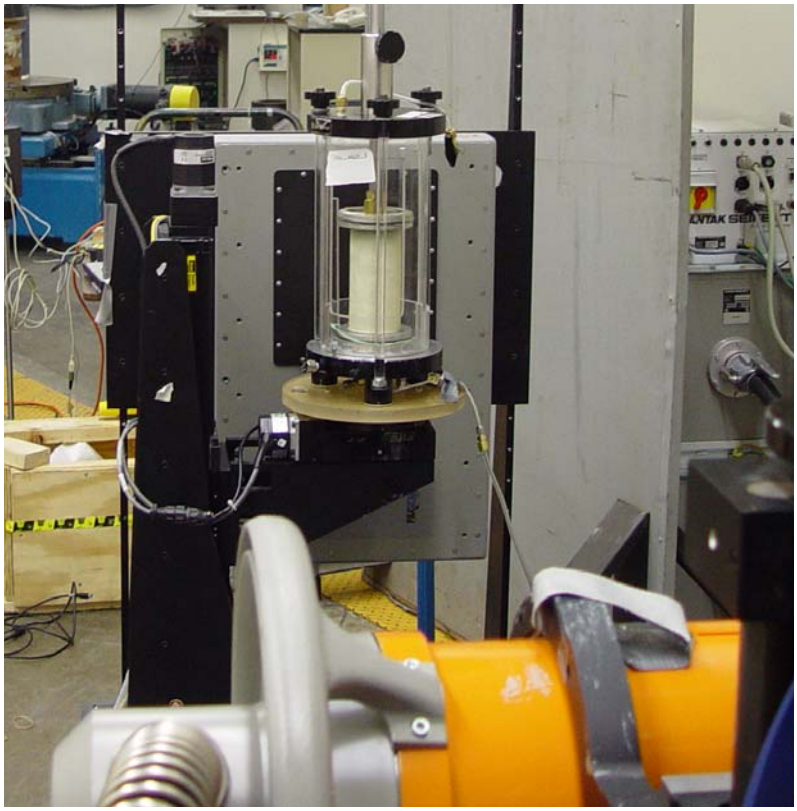

Figure 5.3 Computed tomography system at NASA/Marshall Space Flight Center

5.3.2 Specimen Preparation and Testing Procedure

The specimens scanned with the CT system were prepared at MSFC using the procedure described in Section 3.3.3. Figure 5.4 shows a specimen ready for CT scanning. In each test, the specimen was prepared and kept under vacuum. It was then placed on the stage of the CT scanner and was scanned. The energy level used for the very small and well-graded beads was

335 keV and for the medium beads was 150 keV. After the first scan, the specimen was compressed under a drained axisymmetric CTC while under 25 kPa vacuum (Figure 5.5). The specimen was compressed to 20% nominal axial strain and then scanned again. Figure 5.6 shows a specimen ready to be scanned before compression. After the scanning, the acquired CT images were saved for further analysis with the Flash CT-Viz computer software and custom-developed IDL procedures. Three specimens were prepared using the very small (VSB), medium (MS-25CT), and well-graded glass beads (WG) and were scanned with the Computed Tomography (CT) system. The specimens were prepared with an initial void ratio of 0.604 (VSB), 0.60 (MS_25CT), and 0.402 (WG), respectively.

Figure 5.4 A specimen of well-graded Bead on the stage of the CT Scanner

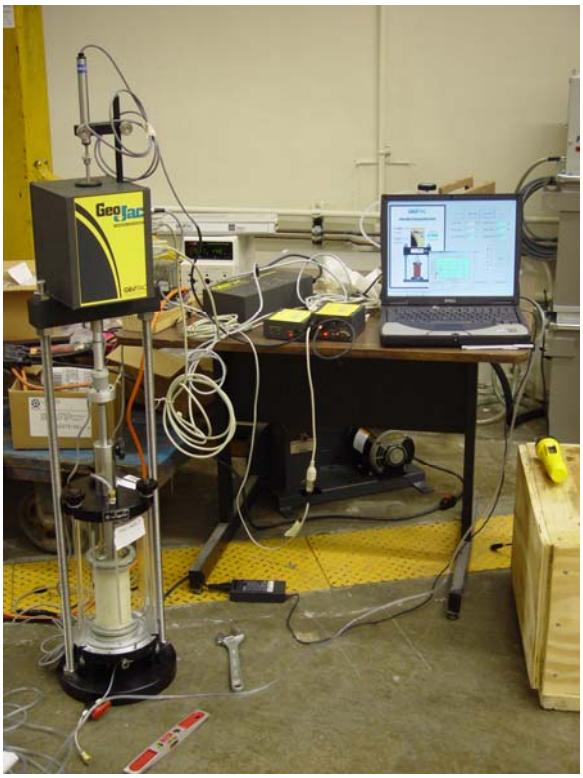

Figure 5.5 A specimem of well-graded beads being compressed

Figure 5.6 Well-graded beads specimen after compression

5.3.3 Density Calibration

A CT density calibration was performed according to the ASTM E-1935-97 Standard. A plexiglass disk (Figure 5.7) with known materials was also scanned at the same energy as the specimens (335 keV). The disk contains the following materials: air, water, pyrex glass, graphite, polyetholene, and aluminum. This was only done for the very small and well-graded beads.

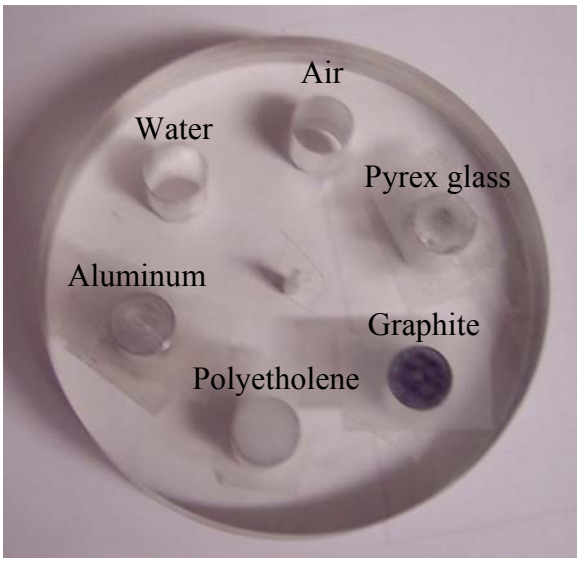

Figure 5.7 Plexiglass disk with known materials

Using the plexiglass disk, the mean CT number (CTN) for each material was calculated. The mass attenuation coefficient (μ/ρ) was obtained from the National Institute of Standards and Testing (NIST) website for each material. The linear attenuation (μ) was then calculated by multiplying the mass density (ρ) by the mass attenuation. Table 5.1 lists the information for each material in the standard. Figure 5.8 shows the relationship between the linear attenuation coefficient and CT Number. The following equations were used for the correlation:

$$\mu[cm^{-1}] = 0.0002 * CTN - 0.0746 \tag{5.2}$$

$$\rho = \frac{\mu}{\mu_m} \tag{5.3}$$

Since the NIST website did not have a listing for soda lime glass beads, the mass attenuation was found by the sum of the mass attenuation of each material in the glass beads multiplied by the fraction of the weight. The weights of the compounds in the glass beads were obtained from the chemical analysis results (Section 3.2.2). The mass attenuation for the small, medium, and large beads was calculated; then the average value was used for density calculations (0.103447 cm^2/g). Table 5.2 lists the mass attenuations of the glass beads. The linear attenuation was then calculated for the glass beads using equation 5.2 and was found to be 0.25862 cm^{-1}.

Table 5.1 Calibration Material Information

Material	**CT Number**	**Mass Attenuation [cm^2/g]**	**Mass density [g/cm^3]**	**Linear Attenuation [cm^{-1}]**
Aluminum	1695.17	0.100196	2.667	0.26719
Air	364.67	0.102777	0.000	0.00000
Water	929.77	0.114225	1.000	0.11423
Pyrex Glass	1479.99	0.102875	2.241	0.23054
Graphite	1238.78	0.102701	1.810	0.18589
Polyetholene	923.87	0.117220	0.942	0.11037

Table 5.2 Mass Attenuation for the glass

Material	**Percent in Beads**			**Mass Attenuation [cm^2/g]**	**Mass Attenuation By Percent**	
	S	**M**	**L**		**S**	**M**
Na	5.31	7.38	2.97	0.0990325	0.005259	0.007309
Ca	9.72	3.98	16.68	0.1067805	0.010379	0.004250
Mg	0.00	1.68	10.69	0.102447	0.000000	0.001721
Si	37.07	27.74	9.39	0.103979	0.038545	0.028844
K	0.00	5.42	15.46	0.1034325	0.000000	0.005606
Al	0.00	0.00	0.27	0.100196	0.000000	0.000000
O	47.91	53.80	44.37	0.103031	0.049362	0.055431

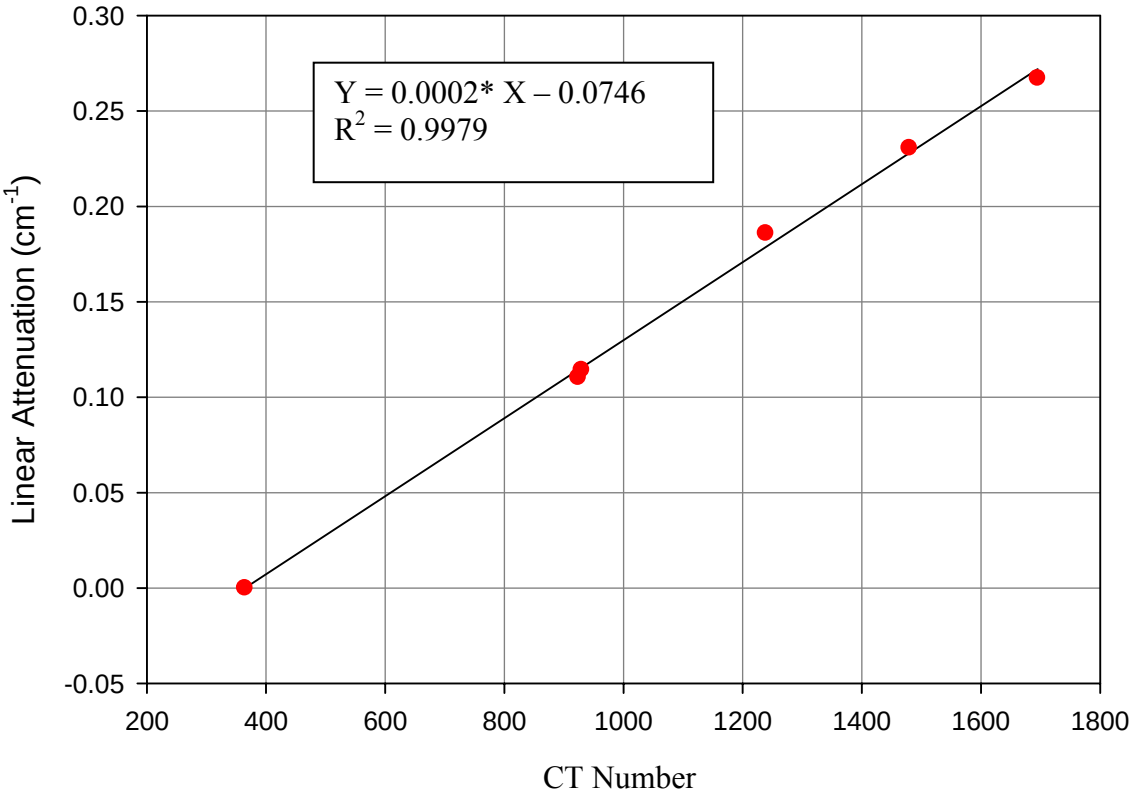

Figure 5.8 Density Calibration curve

5.3.4 Reconstruction of CT Images

The files from the CT Scans were loaded into the computer. Each uncompressed specimen had a set of around 1300 slices (700 x 700 pixel). The compressed specimens had around 1000 slices. A procedure was written in Interactive Data Language (IDL) program to reconstruct the 3D rendering of the data volume. A vertical slice of each volume was created in order to look at the shape of the specimens. Also, horizontal slices of the specimen were taken at five locations (H/4) along the specimens (Figure 5.9). The thickness of each slice was 5.5 mm.

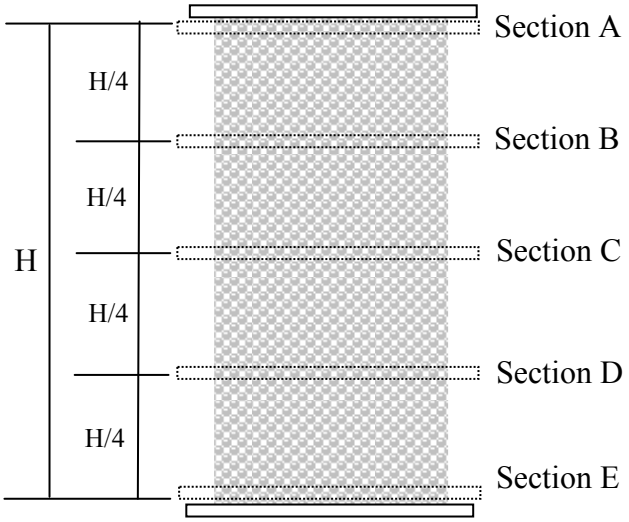

Figure 5.9 Schematic of horizontal sections taken to construct contour maps

5.3.5 Void Ratio of the Specimens

Since the mass density of each specimen was calculated from the CT Numbers, the void ratio was then calculated using the following equation:

$$e = \frac{G_s * \rho_w}{\rho} - 1 \tag{5.4}$$

The void ratio was calculated for each horizontal cross section on a voxel basis before and after compression for the very small and well-graded beads. The distribution of the local void ratio was represented in contour maps. For the well-graded beads (Figure 5.10 through 5.15), the initial "global" void ratio for the specimen was 0.402. Using the CT Number correlation, the void ratio along the sides of the specimen ranged from 0.15 to 0.30 because of the confinement of the latex membrane and boundary conditions. The void ratio close to the center of the specimen ranges from 0.4 to 0.6. This is close to the global void ratio. Near the top of the specimen, the void ratio ranged between 0.6 and 0.9. At the bottom corners of the specimen, the void ratio is less than 0.15 because of the restraints of the endplates. After compression, the local

void ratios in the center of the specimen ranged from 0.75 to 1.20. As the specimen dilates, it becomes loose in the center causing the void ratio to increase. At the bottom of the specimen, the void ratio ranges from <0.15 to 0.30 because the bottom endplates restrain the beads from moving. The beads in the bottom area do not have a place to move; as a result the specimen becomes denser and the void ratio decreases.

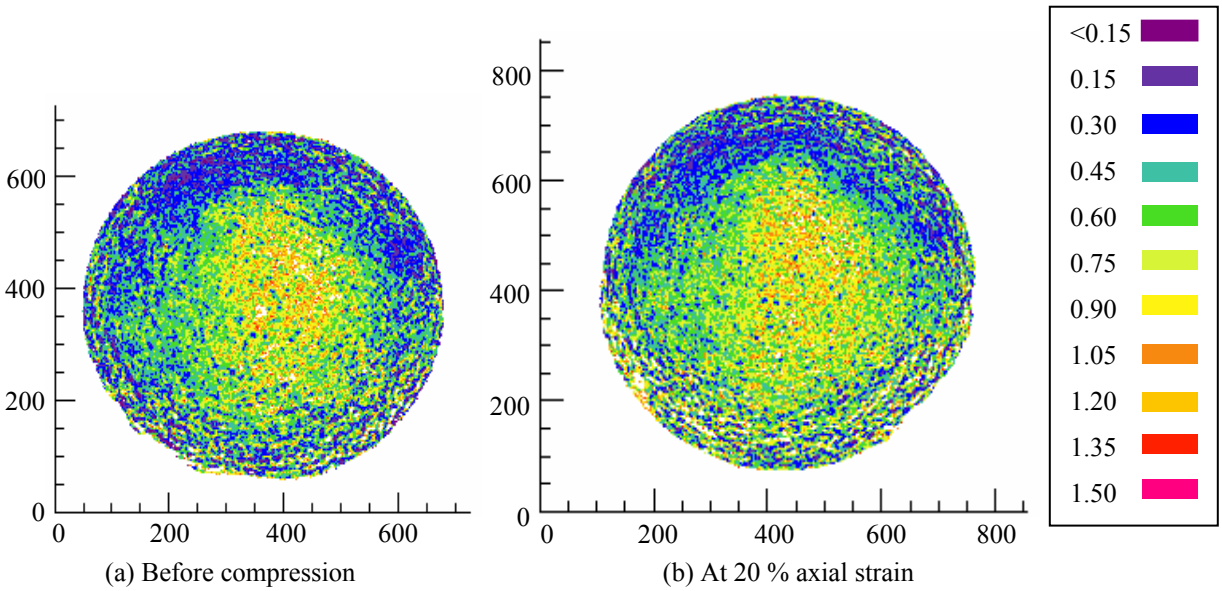

(a) Before compression (b) At 20 % axial strain

Figure 5.10 Void Ratio Contour maps at section A for well-graded beads

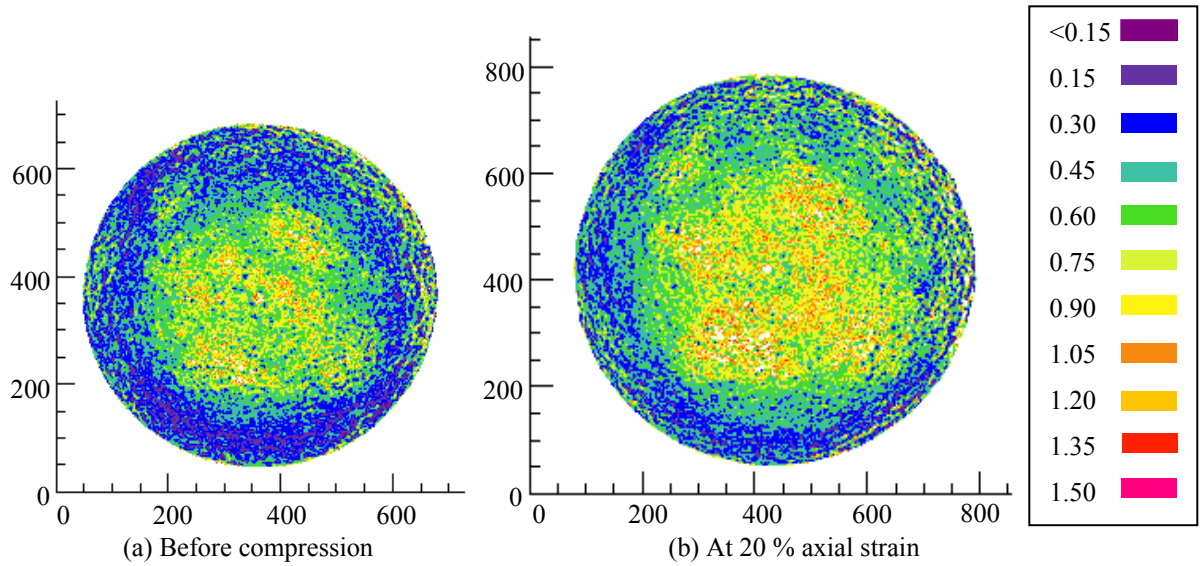

(a) Before compression (b) At 20 % axial strain

Figure 5.11 Void ratio contour maps at section B for well-graded beads

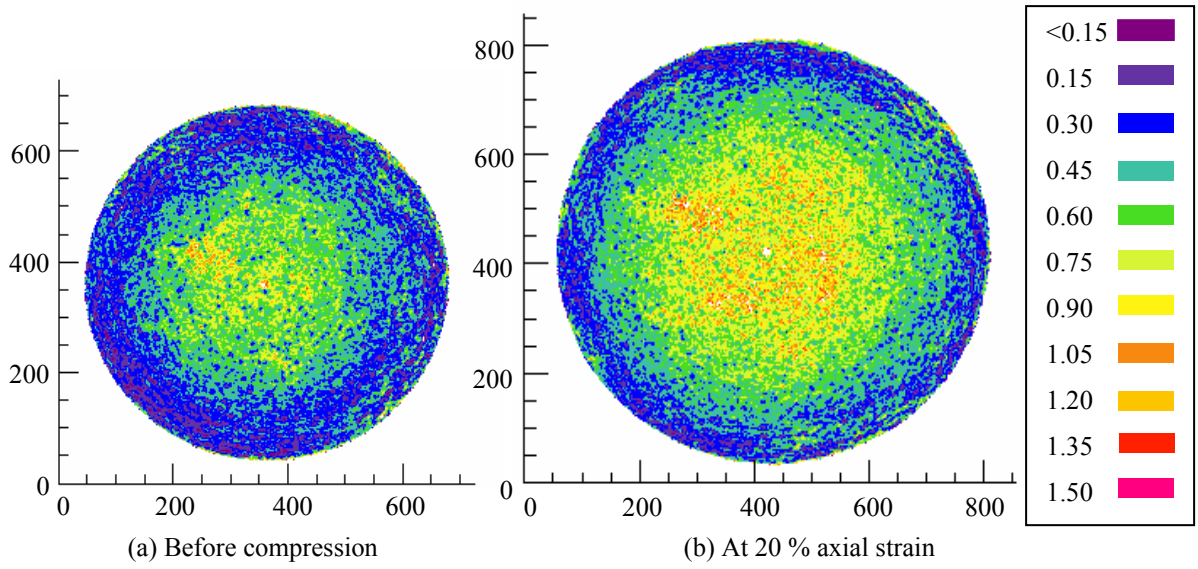

(a) Before compression (b) At 20 % axial strain

Figure 5.12 Void ratio contour maps at section C for well-graded beads

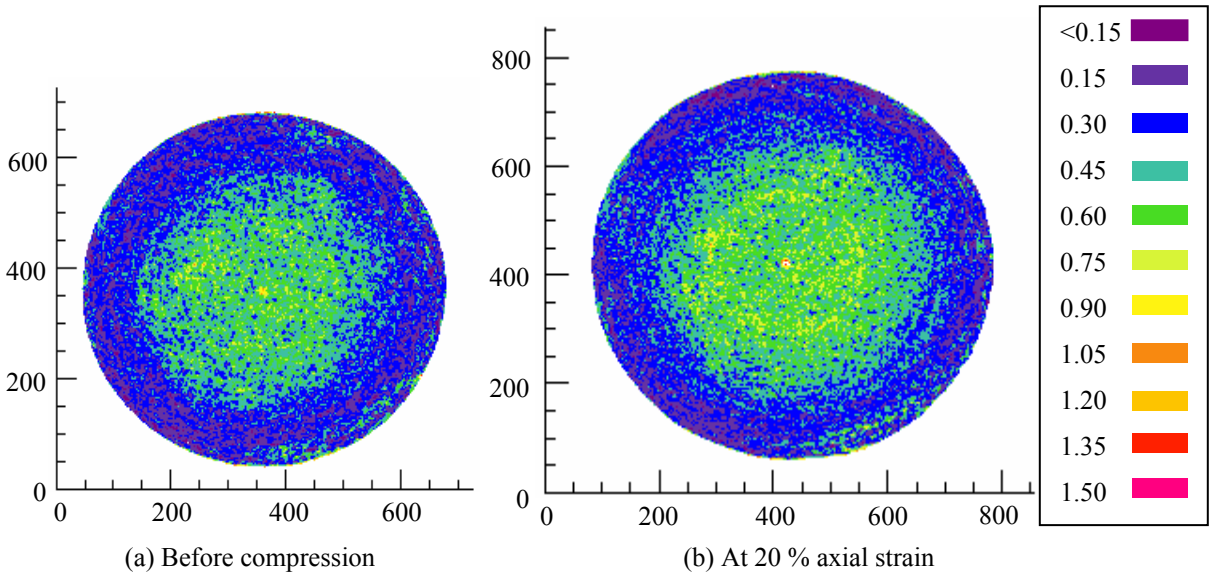

(a) Before compression (b) At 20 % axial strain

Figure 5.13 Void ratio contour maps at Section D for well-graded beads

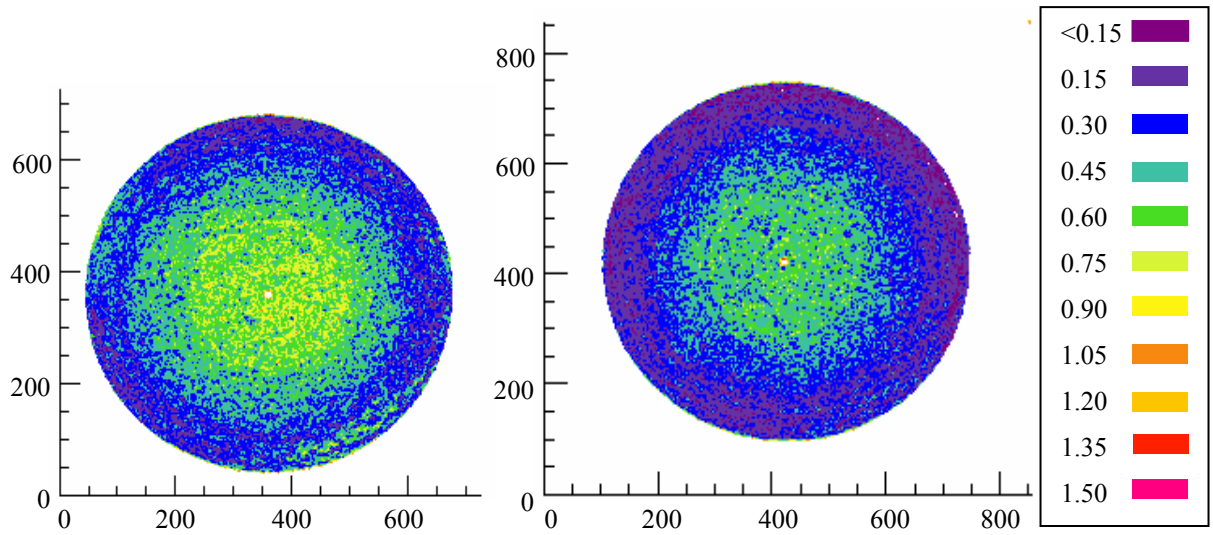

(a) Before compression (b) At 20 % axial strain

Figure 5.14 Void ratio contour maps at Section E for well-graded beads

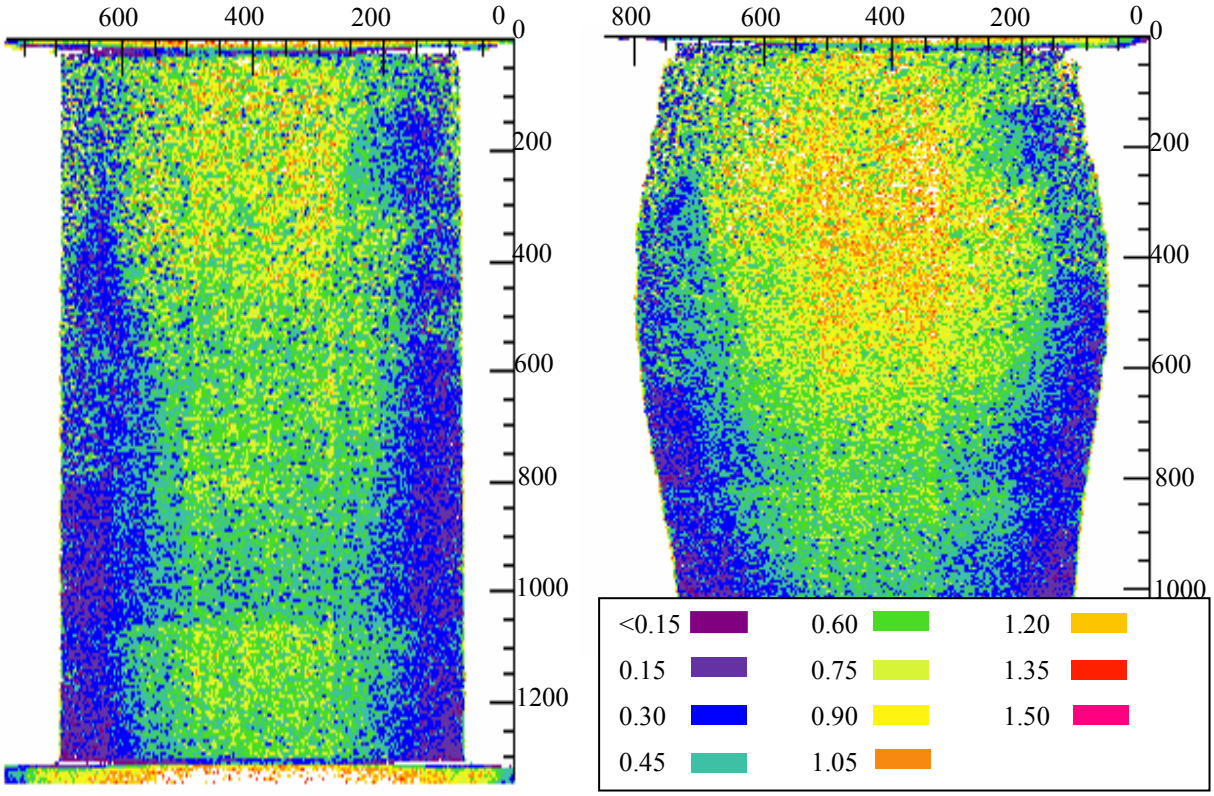

(a) Before compression (b) At 20 % axial strain

Figure 5.15 Void ratio contour maps at a vertical section for well-graded beads

For the very small beads (Figure 5.16 through Figure 5.21), the specimen has a local void ratio ranging from 0.30 to 0.45 around the edge before compression. The center of the specimen has a void ratio range of 0.60 to 0.90. After compression the specimen dilates, and the void ratio range for the center of the specimen increases to 1.05. The bottom slices have a void ratio range of <0.15 to 0.30 because of the restraints of the endplates and the effect of specimen weight.

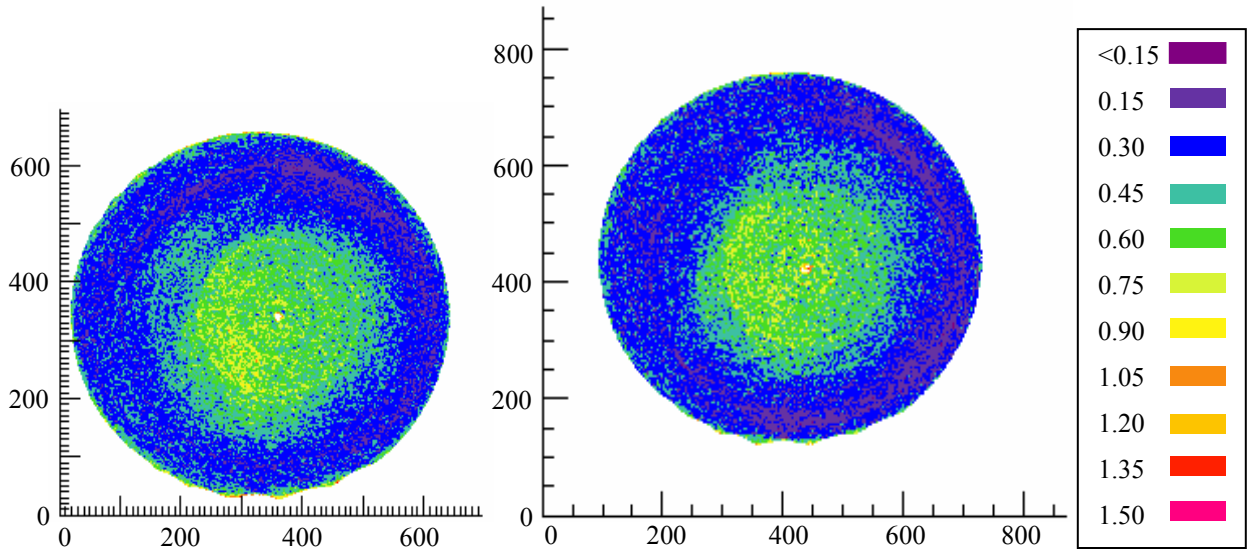

(a) Before compression (b) At 20 % axial strain

Figure 5.16 Void ratio contour maps for Section A for very small beads

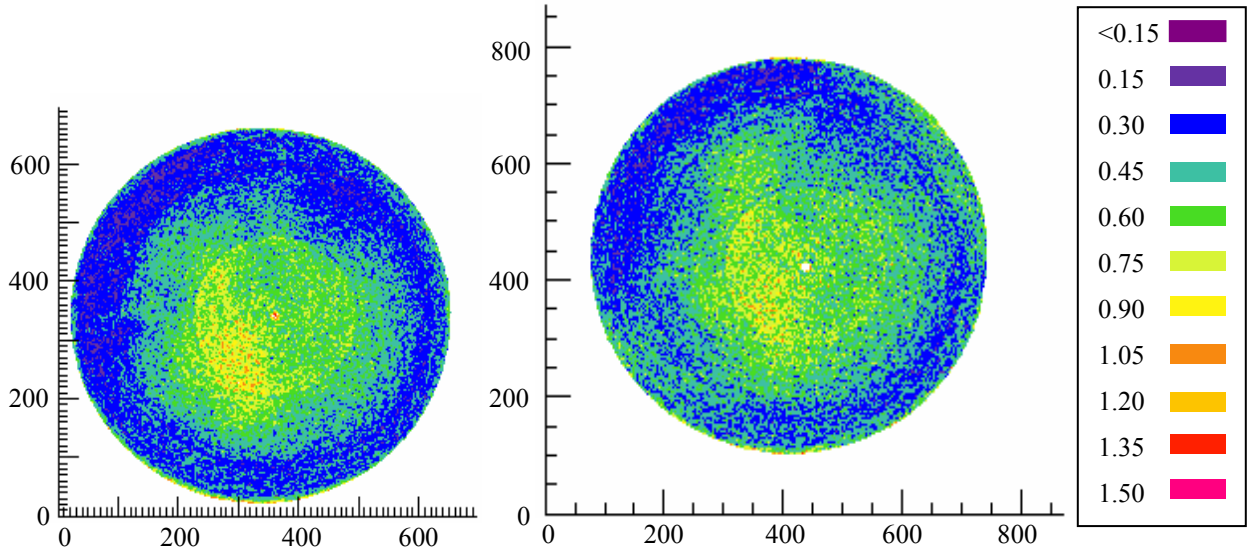

(a) Before compression (b) At 20 % axial strain

Figure 5.17 Void ratio contour maps at Section B for very small beads

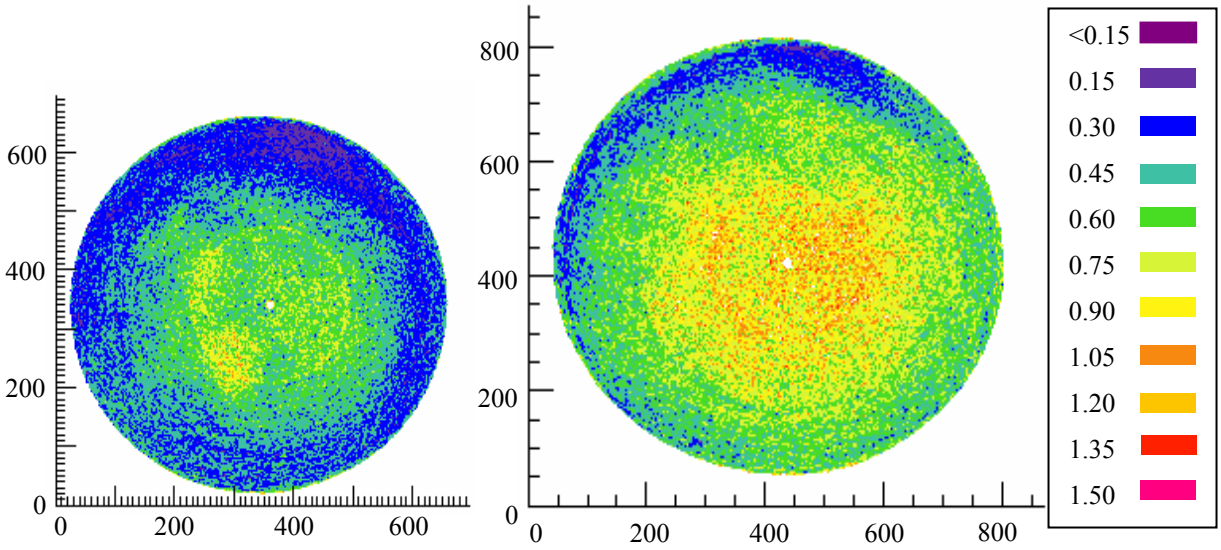

(a) Before compression (b) At 20 % axial strain

Figure 5.18 Void ratio contour maps at Section C for very small beads

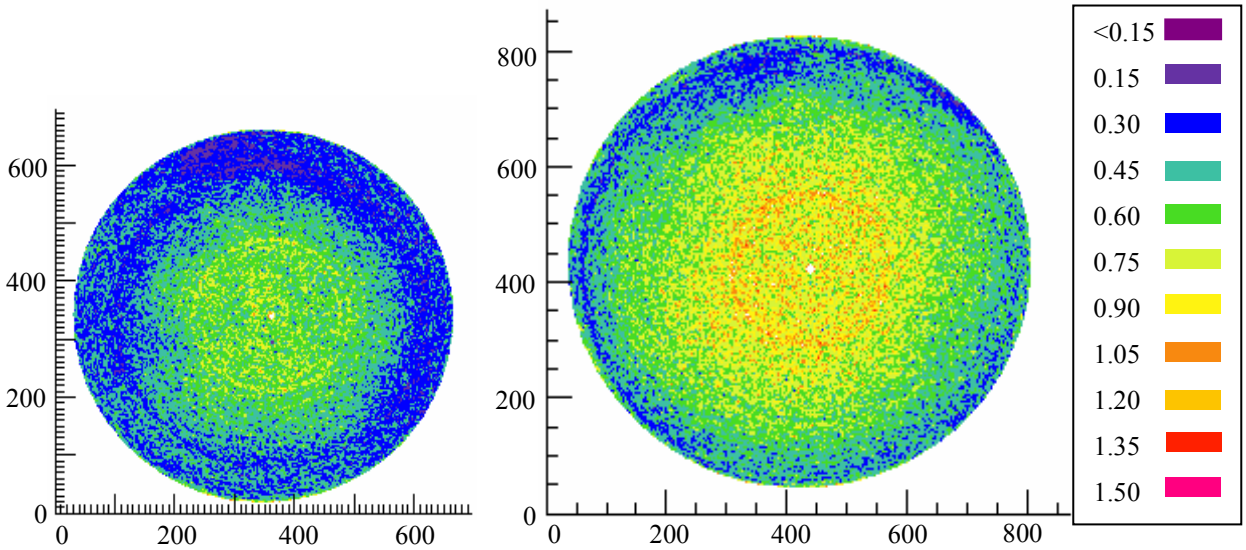

(a) Before compression (b) At 20 % axial strain

Figure 5.19 Void ratio contour maps at Section D for very small beads

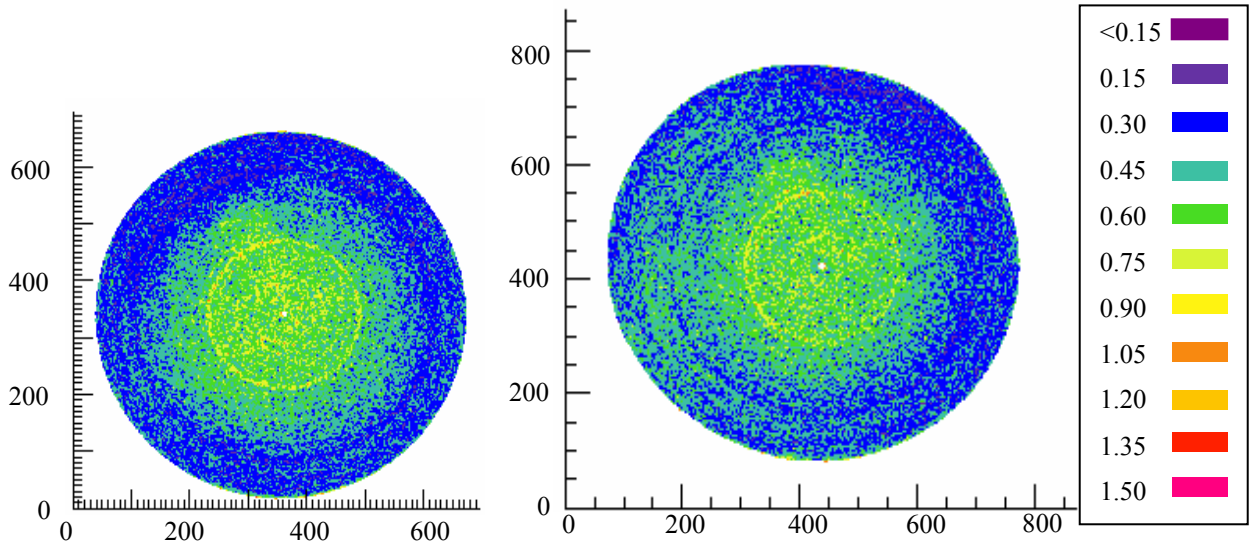

(a) Before compression (b) At 20 % axial strain

Figure 5.20 Void ratio contour maps at Section E for very small beads

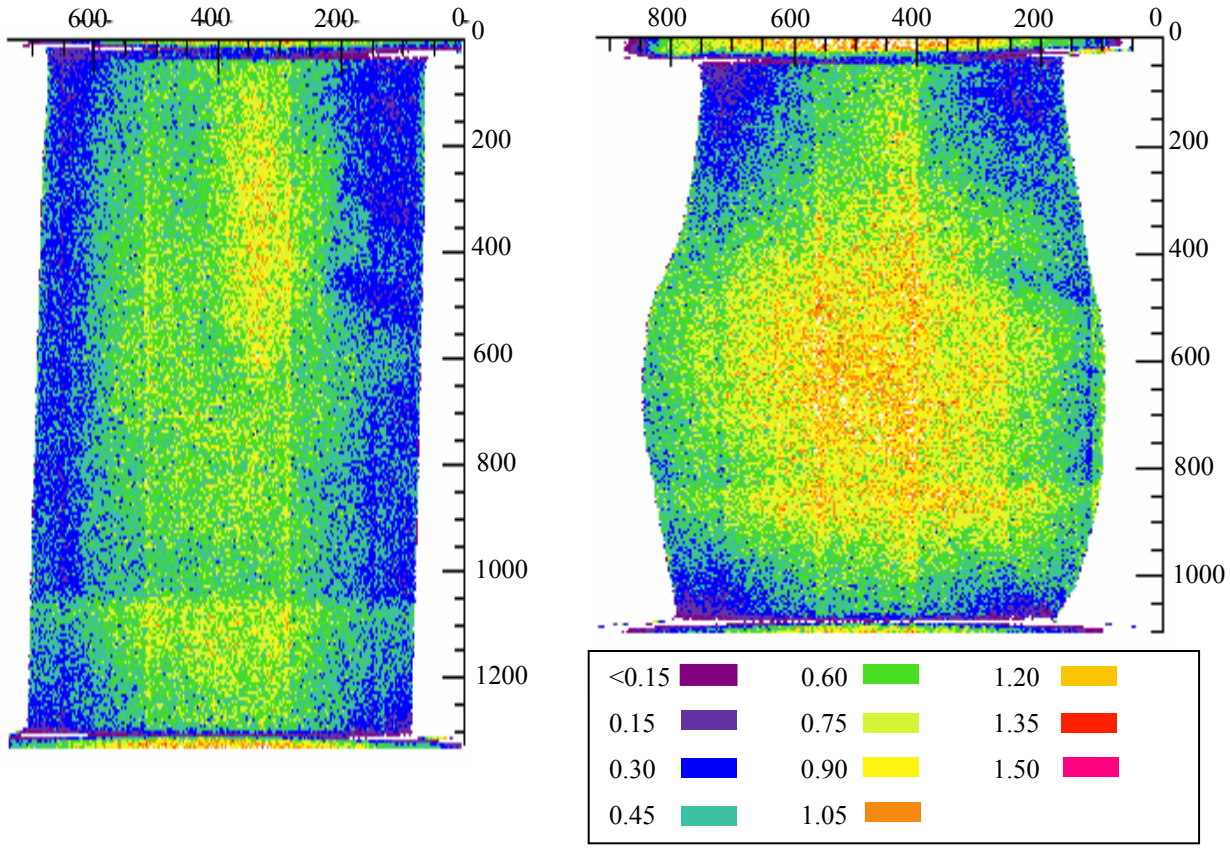

(a) Before compression (b) At 20 % axial strain

Figure 5.21 Void ratio contour maps at a vertical section of the very small beads

For the medium beads (Figure 5.22 through 5.26), the contour maps show local void ratios based on the density calibration used for the very small and well-graded beads. The initial global void ratio for the specimen was 0.60. Using the CT Number correlation that was used for the well-graded and very small beads, a void ratio was calculated for the medium beads. Since the slice from the specimen was 5.5 mm and the average particle diameter was 1.7 mm, actual particles can be found in the contour maps. The purple and blue areas in the contour maps represent particle locations, while the yellow, orange, red, pink, and white areas represent void spaces. In the vertical cross section of the specimen, the contour maps shows how the particles were arranged before the specimen was compressed. The particles were evenly distributed in the specimen. The average void ratio from the contour map for the specimen before compression was between 0.60 and 0.75. After compression a smaller void ratio was found in the top half of the specimen and along the bottom. This occurred because the restrains of the endplates. Where the specimen was bulging in the middle, the void ratio in that area increased to 0.90 - 1.05. As the specimen dilates, it becomes loose in the center causing the void ratio to increase.

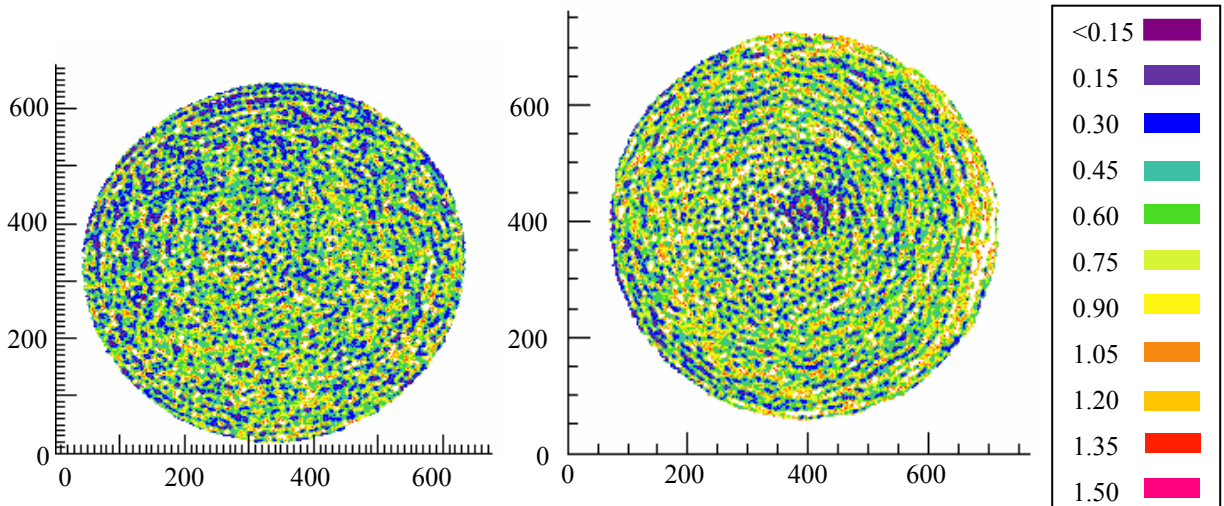

(a) Before compression (b) At 20 % axial strain

Figure 5.22 Void ratio contour plots at Section A of the medium beads

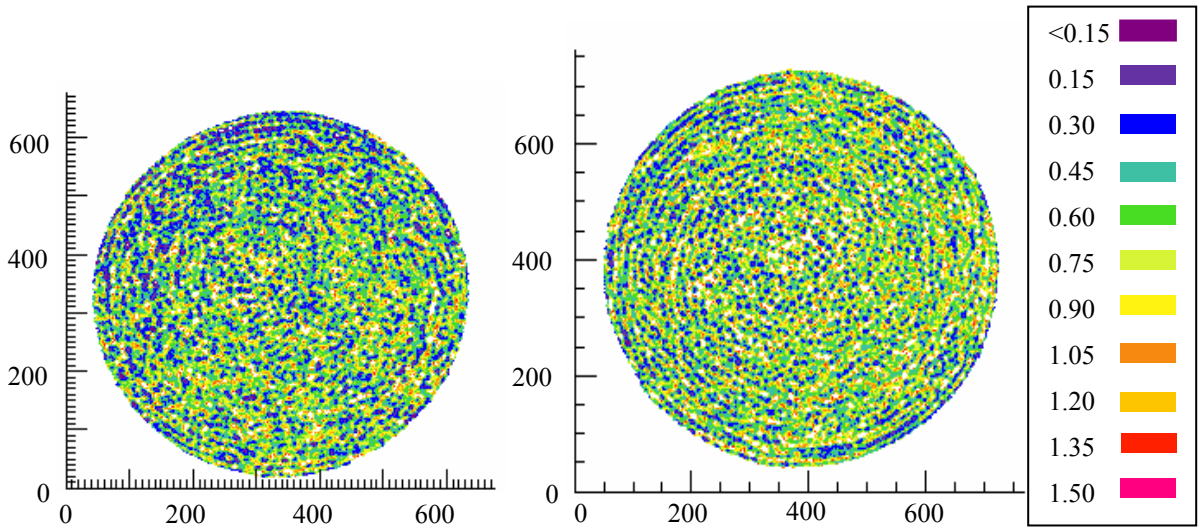

(a) Before compression (b) At 20 % axial strain

Figure 5.23 Void ratio contour plots at Section B of the medium beads

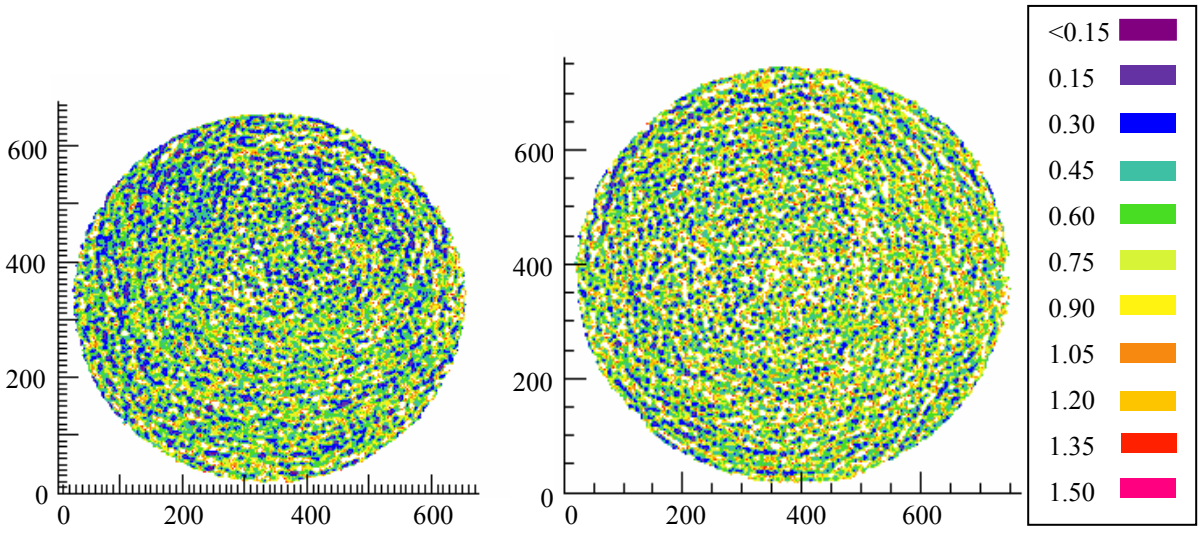

(a) Before compression (b) At 20 % axial strain

Figure 5.24 Void ratio contour plots at Section C of the medium beads

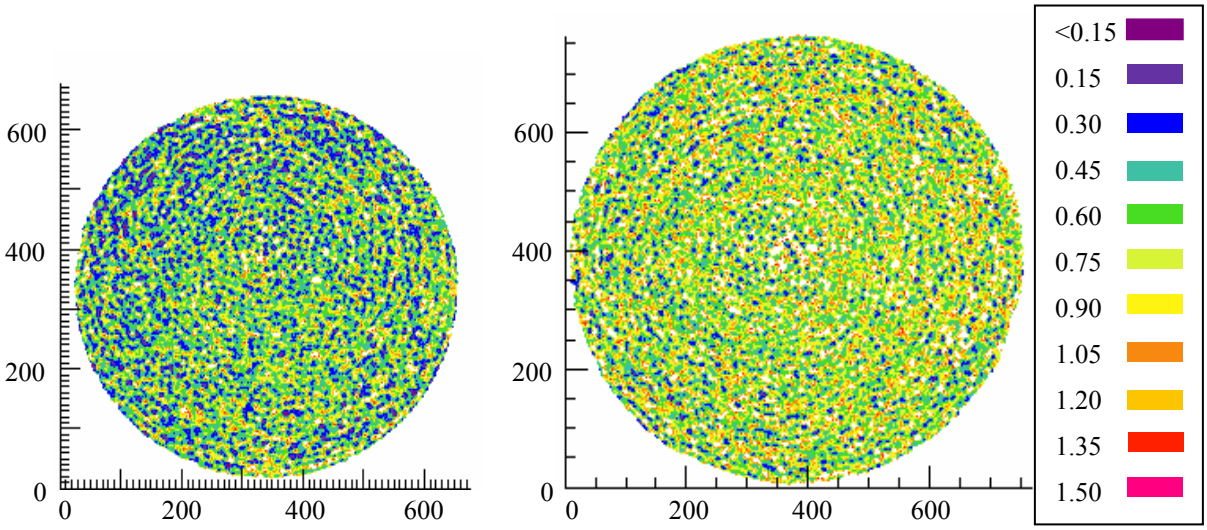

(a) Before compression (b) At 20 % axial strain

Figure 5.25 Void ratio contour plots at Section D of the medium beads

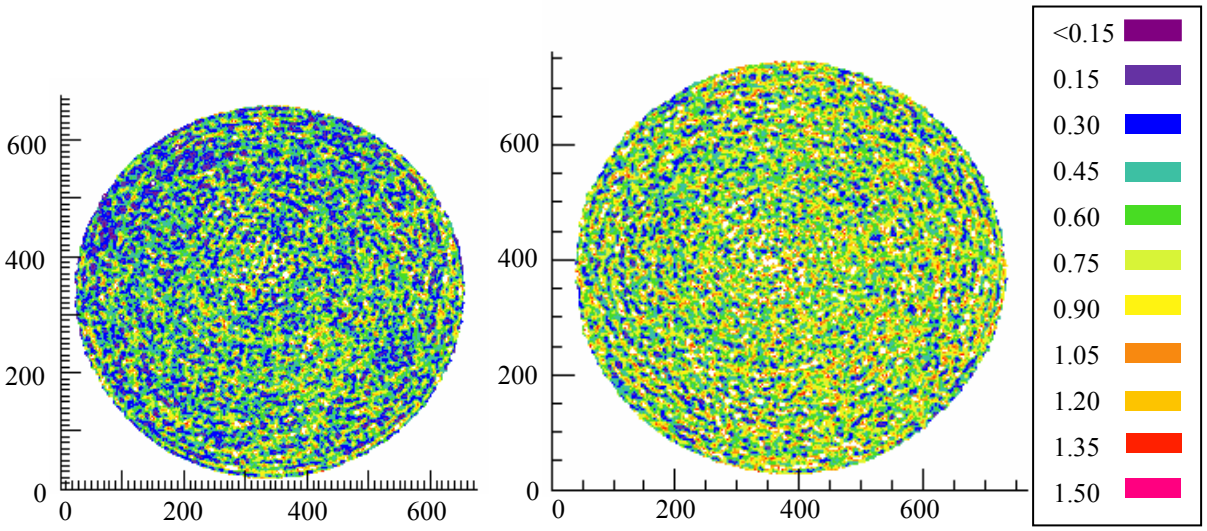

(a) Before compression (b) At 20 % axial strain

Figure 5.26 Void ratio contour plots at Section E of the medium beads

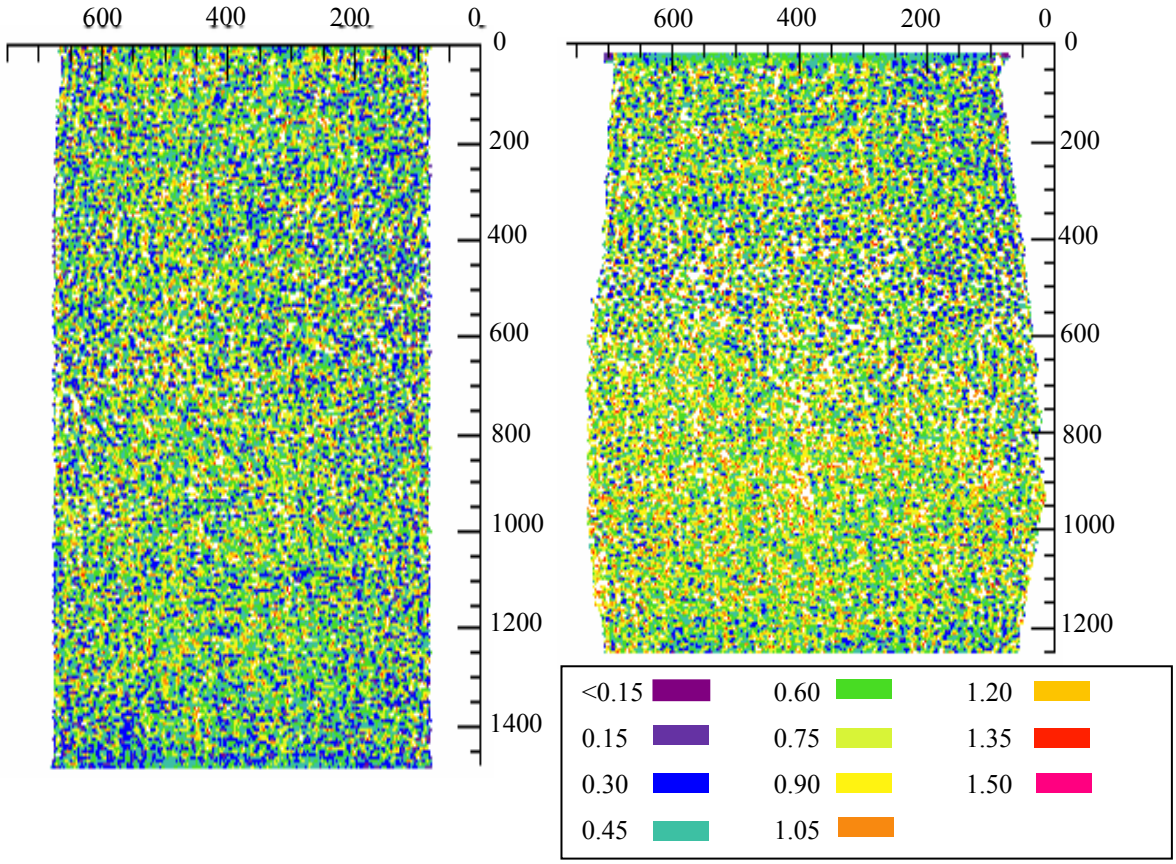

(a) Before compression (b) At 20 % axial strain

Figure 5.27 Void ratio contour plots at a vertical section of the medium beads

From the CT images of all the specimens, the bulging mode of deformation was clearly noticed. No shear bands were found in the three samples after compression. Since the beads are uniform and spherical, they only allow minimal interlocking between the particles. Therefore, the beads form columns and begin to roll over each other causing the bulging deformation to occur. Figure 5.28 is a close-up of the void ratio contour map shown in Figure 5.27 (b), which shows the columns of beads that are formed during compression. The oval highlights a column formation in the medium glass bead specimen. This column formation shown here reaffirms the stick-slip behavior mentioned in Chapter 4.

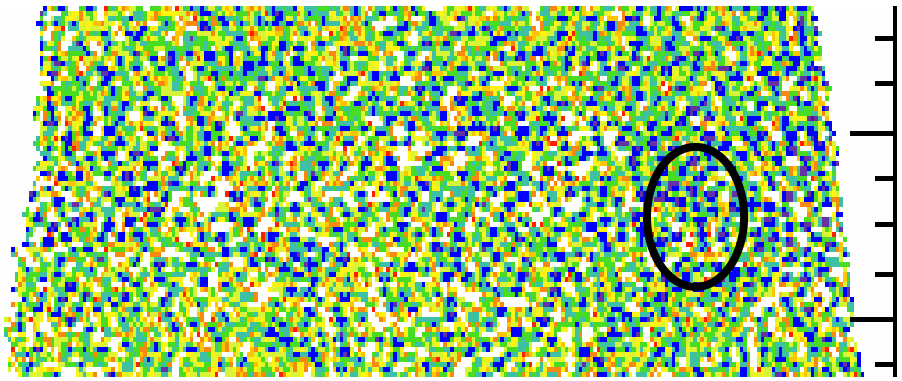

Figure 5.28 Close-up of void ratio contour map of medium glass bead specimen

CHAPTER 6

CONCLUSIONS AND RECOMMENDATIONS

6.1 Conclusions

1. In general, a slight post peak principal stress softening was observed as well as a continuous volume increase (dilation) was recorded even at relatively high strains. This appears to be caused by the uniform shape of the spherical particles. During compression the beads continuously roll over one another because the particles do not interlock with each another.
2. The load oscillations that appeared in the very small, small, and well-graded beads are due to the stick-slip phenomenon. The beads form columns or chains, and as the load is applied to the specimens the columns support the load; however, when it becomes unstable the column collapses, and a drop occurs in the load. These drops appear in the stress-strain analysis too. The larger the particle size, the more stable the columns become. This is why the load oscillations do not appear in the large beads and at high confining pressure for the medium beads. The load oscillations are influenced by the contact points between the particles not the size.
3. From the computed tomography analysis, the specimens showed a bulging deformation mode. This is because the particles roll each other continuously during compression; they do not interlock. If the particles interlock with each other, then deformation will localize into well-defined shear bands. For the glass beads, shear band formation was not observed in all scanned specimens. They only had a bulging deformation. In the medium beads after compression, columns of beads were found in the specimen to support the theory of the stick-slip behavior.

6.2 Recommendations

Based on the findings of the experimental work performed for this thesis, the following recommendations are suggested:

1. Change the surface texture of the beads to a uniform roughness to investigate if roughness has an influence on the stick-slip behavior.
2. Scan a larger diameter glass bead specimen with the CT system to study the formation of the columns that form during compression. The specimen can be scanned at different nominal axial strains, and the formation and collapse of the columns can be tracked.

REFERENCES

Adjemian, F., and Evesque, P. (2004). "Experimental study of stick-slip behavior". *International Journal for Numerical and Analytical Methods in Geomechanics*, Vol 28. pp 501-530.

Albert, I., Tegzes, P., Kahng, B., Albert, R., Sample, J. G., Pfeifer, M., Barabasi, A., Vicsek, T., and Schiffer, P. (2000). "Jamming and Fluctuations in Granular Drag". *Physical Review Letters*, 84, No. 22, pp 5122-5125.

Alshibli, K.A., Sture, S., Costes, N.C., Frank, M.L., Lankton, M.R., Batiste, S.N., and Swanson, R.A. (2000). "Assessment of Localized Deformations in Sand Using X-Ray Computed Tomography". *Journal of Geotechnical Testing*, Vol. 23, No. 3. pp 274-299.

Anandarajah, A. (2004). "Sliding and Rolling Constitutive Theory for Granular Materials". *Journal of Engineering Mechanics*, Vol 130, No. 6. pp 1-16.

Angulo, R. and Intevep, N.O. (1992). "X-Ray Tomography Application in Porous Media Evaluation". *Society of Petroleum Engineers: Second Latin American Petroleum Engineering Conference.* Pp 187-197.

Bardet, J. P. (1997). *Experimental Soil Mechanics*. Prentice-Hall, Inc., Upper Saddle River, New Jersey. 584 pages.

Behringer, R. P. et al. (1999). "Predictability and granular materials". *Physica D*, 133. pp 1-17.

Behringer, R. P., Howell, D., and Veje, C. (1999). "Stress Fluctuations in a 2D Granular Couette Experiment: A Continuous Transition". *Physical Review Letters*, Vol 82, No. 26. pp 5241-5244

Cain, R., Page, N., and Biggs, S. (2001). "Microscopic and macroscopic aspects of stick-slip motion in granular shear". *Physical Review E*, Vol 64, No 016413. pp 1-8.

Coduto, D. P. (1999). *Geotechnical Engineering Principles*. Prentice-Hall, Inc., Upper Saddle River, New Jersey. 759 pages.

Desrues, J., Chambon, R., Mokni, M., Mazerolle, F. (1996). "Void Ratio evolution inside shear bands in triaxial sand specimens studied by computed tomography". *Geotechnique*, Vol 46, No. 3. pp 529-546.

KTH Royal Institute of technology web site. (2001). Computed Tomography. http://kurslab.physics.kth.se/klab/ Labpek/CTlabpek.pdf.

Lambe, T. W. and Whitman, R. V. (1969). *Soil Mechanics*. John Wiley & Sons, New York, New York. 553 pages.

Michael, G. (2001). "X-ray Computed Tomography". *Physics Education*. pp 442-451.

Nasuno, S., Kudrolli, A., Bak, A., and Gollub, J. P. (1998). "Time-resolved studies of stick-slip friction in sheared granular layers". *Physical Review E*, Vol 58, No. 2. pp 2161-2171.

Overney, R., Takano, H., Fujihira, M., Paulus, W., and Ringsdorf, H. (1994)."Anisotropy in Friction and Molecular Stick-slip Motion". *Physical Review Letters*, Vol 72, No. 22. pp. 3546-3549.

Phillips, D.H., and Lannutti, J.J. (1997). "Measuring physical density with X-ray computed tomography". *NDT&E International*. Vol 30, No. 6. pp 339-350.

Powrie, William (1997). *Soil Mechanics: Concepts and Applications*. Chapman & Hall, London, UK. 420 pages.

Radjai, F., Evesque, P., Bideau, D., Roux, S. (1995). "Stick-slip dynamics of a one-dimensional array of particles". *Physical Review E*. Vol 52, No. 5. pp 5555-5564.

Santamarina et al. (2001). *Soils and Waves*. John Wiley & Sons, New York, New York. 805 pages.

Volfson, D., Tsimring, L., and Aranson, I. (2004). "Stick-slip dynamics of a granular layer under shear". *Physical Review E*. Vol 69, No. 031302..

VITA

Lynne Elizabeth Roussel was born in Thibodaux, Louisiana, on December 23, 1980. She attended Edward Douglas Catholic High School in Thibodaux, Louisiana, graduating in 1998. From the fall of 1998 to the spring of 2003, she attended Louisiana State University where she obtained her Bachelor of Science in Civil Engineering degree with a minor in structural engineering. In the Fall of 2003, she enrolled in the graduate program at LSU for geotechnical engineering. That fall she was awarded the NASA Graduate Students Researchers Program Fellowship. Currently she is scheduled to receive her Master of Science in Civil Engineering degree in August of 2005, and she has accepted employment at Aquaterra Engineering, LLC, in Port Allen. In June 2005, she will marry Adam Smith.